博士論文

A Study on Motion Response and Wave Energy Absorption Characteristics of a Ship with an Active Control System

（アクティブ制御システムを有する船の運動応答と波エネルギー吸収特性に関する研究）

韓　佳琳

A Study on Motion Response and Wave Energy Absorption Characteristics of a Ship with an Active Control System

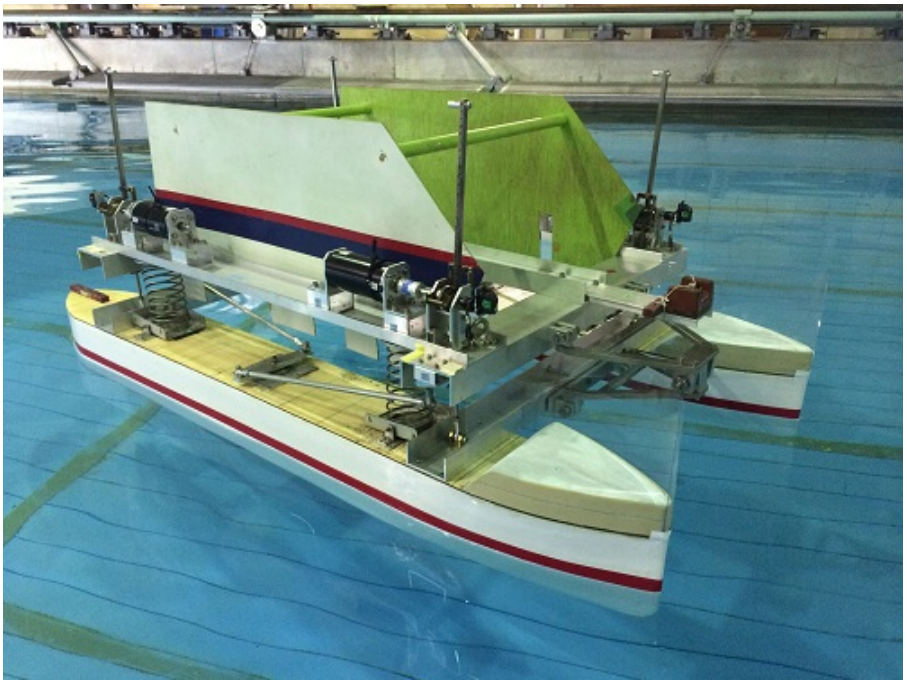

Jialin Han

Kitazawa Laboratory
Systems Innovation
School of Engineering
the University of Tokyo

February 21, 2017

Abstract

A novel catamaran was designed and developed. Its cabin was suspended upon two hulls by four compression springs. Two sets of pantographs and Watt's links were used to guide the vertical relative motion between the cabin and the hulls while restraining the horizontal one. Four motor/generators (M/Gs) were set on the deck and four racks were vertically settled on the hulls. Each of them was linked by a pinion gear in such a way that a shaft of the M/G was connected to that of the pinion, while the tooth of the pinion and the rack were meshed together. Through this rack-pinion-M/G connection, the relative displacement between the cabin and the hulls can be transformed into rotational motion of the M/Gs, and vice versa.

Control systems were designed to improve the ride comfort of the cabin by reducing its motions, and to harvest wave energy by converting kinetic energy into electrical energy. Skyhook control was employed for the former purpose. It was aimed to maintain the acceleration of the cabin at $0\,\mathrm{m/s^2}$ with an I controller. For the latter purpose, an impedance matching technique was used to obtain the maximum power at a given frequency. A simulation program was built to validate the design concept of the control systems in one degree of freedom.

Several experiments were carried out to investigate the performance of the proposed ship structure and control systems, which included a dry test and a wet test. The dry test consists of a free decay test of the cabin, a motor driven test and a forced oscillation test. The natural frequency, friction and dead zone of the suspensions were investigated during the free decay test and the motor driven test. The motion response of the cabin was observed in the forced oscillation test, during which the hulls were riding on a bench that was oscillated vertically.

The wet test was implemented at a deep water towing tank. The motion response of the cabin and the hulls in terms of heave, pitch and roll, the wave energy capture width ratio and the relative displacement between the cabin and the hulls were observed under several regular wave conditions. Skyhook mode, Maximum Power Point Tracking (MPPT) mode, integrated mode, free mode and rigid mode were tested one by one under the same wave conditions. Comparison of those modes were made. The calculation of the primary and secondary energy conversion efficiency in the MPPT mode was carried out to track the flow and distribution of the energy from the incident waves to the ship.

Promising results concerning the motion reduction of the cabin and the energy harvesting ability were obtained. It suggested that a mature type of this novel ship could extend the workability of a ship and benefit the activities on the sea.

Acknowledgements

First and foremost, I would like to express my greatest appreciation to my supervisor Prof.Daisuke Kitazawa, who has put generous effort into the development of this research project, especially in the model developing and fund raising.

Next, my deep thanks go to Mr.Teruo Maeda, for the brilliant idea of the concept of the cabin-suspended ship (Wave Harmonizer), and for the excellent pieces of advice on the mechanical system development of the structure and for the great effort in fund raising and management, without which the model ship would not have been built.

I am also sincerely grateful to Mr.Yukitsugu Hirota for the suggestions and tutorials about the control system design and the development of the simulation program, for the early and quick replies to my E-mails, and more importantly for being so patient when answering my questions.

I want to express my greatest thanks to Mr.Hiroshi Itakura for the collaboration and suggestions on the structure design, model ship assembly and tests, for the large amount of overtime work at the ocean engineering basin, and for being so kind and supportive with me and the experiments.

I also would like to extend my thanks to Mr.Masatoshi Fujino and to my lab mates, Dr.Junbo Zhang, Dr.Makoto Kanehira, Mr.Kentaro Chimura and Ms.Sayuri Taya for their help with the model ship experiments and the wonderful atmosphere in the lab.

Thanks also to my friends in Delft University of Technology, Mr.Ji Bao, Mr.Shuo Zhang and Dr.Xiangrong Wang, for the support they have provided in study, discussions and group works.

Last but not least, I would like to express the deepest gratitude to my family and my dearest friend Ms.Alexandra Florentina Stancu for being so supportive in my study and life, for being by my side in times of need, and especially for the courage and love they have given me.

I also appreciate the finical support provided by the New Energy and Industrial Technology Development Organization (NEDO) and Japan Society for the Promotion of Science (JSPS). The major part of this paper is based on results obtained from a project commissioned by NEDO. A part of the research was supported by JSPS, Grant-in-Aid for Challenging Exploratory Research, 25630399.

Contents

List of Figures

List of Tables

Glossary

cabin segment Page. 10
CWR wave energy Capture Width Ratio; Page. 58
DOF Degree of Freedom; Page. 3
electrical energy loss Page. 48
FL Front-Left; Page. 10
FR Front-Right; Page. 10
free mode Page. 29, 56
hill climbing method Page. 18
hull segment Page. 10
impact factor Page. 22
impedance analogy Page. 26
impedance matching Page. 18
integrated mode Page. 56
LTspice Page. 25
M/G Motor/Generator; Page. 5
M/G energy Page. 48
measured energy Page. 48
mechanical impedance Page. 18
mobility analogy Page. 27
MPPs Maximum Power Points; Page. 18
MPPT Maximum Power Point Tracking; Page. 18
MPPT mode Page. 56
NSM New Strip Method; Page. 108
PID controller Page. 15
plugging braking Page. 20
primary energy conversion efficiency Page. 92
regenerative braking Page. 20
rigid mode Page. 56
RL Rear-Left; Page. 10
RR Rear-Right; Page. 10
secondary energy conversion efficiency Page. 92
skyhook mode Page. 29, 56
suspension segment Page. 10
terminal energy Page. 48
WHzer Wave Harmonizer; Page. 5

Chapter 1

Introduction

1.1 Ocean Waves, Energy and Humans

The history of human society has a tight relation with the ocean. Vessels were designed and built with respect to various purposes, for instance, maritime trades, coastal fishing, travel or wars. Along with the development of the modern technologies and the extension of human activity area, several fields have raised researcher's attention, such as, deep sea exploration and wave energy extraction.

The ocean covers about 79% of the earth surface. Surface waves are continuously generated by the winds, which grow by receiving energy transformed from the winds. During storms, the wave heights increase along with the wave lengths decrease and the wave frequencies broaden. This kind of waves carry significant amount of energy, but it might be dangerous for vessels out on the sea at this condition and it is of hard to convert the energy into other forms. Known that in deep waters, long waves travel faster than short waves. The storm produced irregular waves travel radically from the storm center with different propagation speed. The far the waves away from the storm center, the less irregularity the waves carries. At a certain distance, the sea condition can be regarded as 'safe', which means it does not exceed the allowance of vessels or platforms could bear. The characteristics of a sea site can be described by a power spectrum, from which the significant wave height and the mean period can be estimated. Those are important parameters concerning to offshore platform design, offshore wind farm design or other offshore activities.

Japan has an extensive coastline and close to the Kuroshio current, which makes the Japanese sea at pacific ocean side a high wave energy holding area. A research about the marine renewable energy assessments around Japan has been conducted by the University of Tokyo collaborating with Japan Agency for Marine-Earth Science and Technology (JAMSTEC). The simulation covered a 21-years period, from 1994 to 2014[1]. It indicated that during autumn and winter season, the wave power density at northwest of Japan can reach up to $25 \sim 40\,\mathrm{kW/m}$. The significant wave height of the sea at pacific ocean side is about $1.5 \sim 3.0\,\mathrm{m}$, during the autumn and winter season it is averagely above $2.0\,\mathrm{m}$.

Large wave height carries vast amount of energy, however restrains the workability of vessels, reduces the accessibility of offshore structures and deteriorates the ride quality. To solve this problem, a novel catamaran equipped with suspension systems and control systems was proposed and tested. The adoption of the suspensions was inspired by vehicles, which have achieved great motion reduction by using suspension and advanced control algorithms. Moreover, the catamaran can also act as a wave energy converter converting the kinetic energy into electrical energy. By employing different algorithms, on the one hand the motion of the cabin

can be reduced, hereby improves its ride comfort and extends its workability; on the other hand wave energy can be harvested and reused.

1.2 Ride Comfort Enhancement Devices

Improving ride comfort has been a long term issue in the transportation industry. A lot of approaches and devices have been developed for land vehicles and vessels.

1.2.1 Land Vehicles

Since the first internal combustion engine was invented, vast research has been conducted and many inventions have been made in building shock isolation systems. One of the most promising and widely used techniques is known as suspension. It normally consists of springs, dampers, tires and some linkages. The whole system allows a certain reduction of the vibration disturbance caused by road roughness, hereby providing better road-holding ability and ride quality. An improvement of the ride comfort can be achieved by applying proper control strategies[2], or by mounting advanced shock absorbers[3][4]. The energy harvesting ability from the vibration motion has also drawn attention to some researchers[5][6].

1.2.2 Vessels

Vessels are traditionally a rigid body structure. It has 6 degrees of freedom motion. Several approaches have been proposed and tested to reduce the roll motion of the ship. The methods adopted in those researches covered passive control, active control, simulation, numerical study and validation experiments.

- **bilge keels**
  Bilge keels are the most commonly used technique, which fit to most of the vessels. They are plates that longitudinally fixed to the boundary layer outside a hull near the bottom on both starboard and port side. The bilge keels can cause an amount of water to move with the ship while rolling, produce turbulence hereby damp the roll motion.

- **fins**
  The active fin stabilizers have high efficiency to reduce the ship motion. They work in such a way that gyro sensors send the roll motion of a ship back to a control system, then a command for adjusting the direction of the fins is calculated by the control system, consequently the move of the fins cause forces opposing the roll motion. In this process, the control algorithms play a key role in the efficiency of the roll reduction. The control technique includes first-second-order sliding mode control[7], fuzzy control[8] and cascade control[9] and so on.

- **anti-roll tank**
  The fluid in a tank can be regarded as a resonant fluid system, which justifies itself as a counter-moment generator compensating the moment produced by sea waves, hereby reduce the roll motion of a vessel. The types of tank includes free surface tank, U-tube tanks and free-flooding tanks. Passive free surface tank is normally effective at low encounter frequency with an expense of reducing the metacentric height of the vesse. In contrast, U-tube tanks, free-flooding tanks are more sophisticated and have active control system[10]. Besides experimental investigation, a simulation program was developed by

using smoothed particle hydrodynamics[11]. A U-tube tank may have a potentical to be used as a wave energery converter transforming kinetic energy into electricity[12].

- **roll rudder stabilizer**
  It was known that turning a vessel will also cause a heel angle of the vessel. The greater the turning speed, the larger the heel angle. It was observed that before a vessel enters into any yaw motion or turning, an initially heels inwards was generated. The characteristics of the rudder-induced roll was studied. Rudder cooprated with fins enhanced roll stabilisation[13]. An autopilot has been developed in [14], with only one input of the rudder angle, the controller outputs two outputs as the heading of the ship and the roll angle. Therefore the rudder can not only for controlling the course direction but also reduce the roll motion. This approach was proved to be promising in roll reduction and has been used by Royal Netherlands Navy. Besides the roll motion, yaw motion of a vessel can also be regulated by using a neural network controller.[15]

- **cabin-suspended ships**
  Velodyne Marine® located in California has developed a catamaran equipped with full active suspensions, which consists of state-of-art actuators and air suspensions. By using four G-sensor or gyro sensor detecting the motion of the cabin, the control system calculates the needed force for the air suspension to counteract the motion of the cabin. A high level of motion reduction can be observed in a sea trial video[16]. Another cabin-suspended ship was developed by Nauti-craft Pty Ltd located in Australia. A passive reactive interlinked hydraulic system was employed to reduce the motion of the cabin. The ship was tested on a catamaran and a four-hull type. Both sustained a high stability of the cabin in their sea trial videos[17].

1.2.3 Evaluation Methods for Ride Comfort

A conventional and widely accepted approach for ride comfort evaluation is known as Frequency Weighting, denoted as W_f. It gives a specific weighting factor to an acceleration of a motion at a given frequency, which was summarized from vast of lab experiments and sea trials, the details of which was demonstrated by ISO2631-1[18]. With usage of W_f, several concepts were developed, such as Motion Sickness Dose Value (MSDV)[19], Ride Comfort Index (RCI)[20]. MSDV is used to evaluate ride comfort concerning to one degree of freedom (**DOF**) motion, such as vertical acceleration, while RCI could evaluate that with two degrees of freedom motion, such as a combination of vertical acceleration and lateral acceleration.

1.3 Wave Energy Converters

Ocean wave energy is one of the well-known renewable energy types. A number of devices have been developed by researchers and engineers in aiming of extracting energy from ocean waves. Those devices are named as wave energy converter (WEC). The most efficient WEC was Salter' Duck, which was first designed and tested in 1970s by Stephen Salter. It can absorb about 90% energy from the incoming waves and leave a calm sea behind[21]. Other WECs in developing are attenuator, point absorber, oscillating wave surge converter, oscillating water column and so on. Each of them has its own converting principle.

- **Attenuator**
  An attenuator is a floating device that absorbs energy under head seas condition. It has two arms connecting in line with hinged joints. It is parallel to the wave propagating direction, therefore the incoming waves drive the arms flapping up and down. This movement pressurizes oil into a hydraulic motor which drives a generator producing electricity[22]. Pelamis Wave Power is a successful application of attenuator, which is the first offshore WEC powered a national grid[23].

- **Point Absorber**
  A point absorber is a floating device that can absorb energy from all the direction of wave propagating. It mainly consists of a buoy and a base. The base is beneath the sea level having less motions by either fixed on the sea floor or floats deep enough. While the buoy is floating at water surface oscillating along with the elevation of the waves. It converts the relative motion between the buoy and the base into electrical energy. To optimized the extract efficiency, the characteristics of the parameters such as added mass and damping was investigated by means of phase control[24], parametric resonance invesitgation[25].

- **Oscillating Wave Surge Converter**
  An oscillating wave surge converter utilizes the surge motion of the waves. The water particles in motion push or pull a pendulum moving with them to and fro. The pendulum connects to a relatively stable base with a pivoted joint. The kinetic energy of the pendulum is converted into electricity. Nearshore devices were developed with active control surfaces so as to fit different geometry conditions[26]. Some researches investigated the interactions between a surge converter and the waves, for instance viscous effects[27] and slamming[28].

- **Oscillating Water Column**
  An oscillating water column normally has a water column connecting with an air chamber. The incoming waves cause the water level inside the water column varies up and down, lead to the air pressure in the air chamber fluctuates, thus drive a turbine on top of the air chamber rotates and simultaneously generates electricity. Theoretical studies and simulation programs were conducted to validate the reliability of the concept by a lot of researchers. An U-Oscillating Water Column was mathematically modeled and experimentally investigated[29]. Large scale experiments were carried out to investigate the wave reflection and loading from the waves which suggested that the device can be integrated with wall breakers to reduce wave reflection[30].

1.4 Previous Researches

A novel ship equipped with suspension systems, which were mounted between the cabin and the hulls, was developed. The ship was named as **Wave Harmonizer**(**WHzer**). By applying various control algorithms, the motion of the cabin can be controlled. At a motion reduction mode, the motions of the cabin is reduced hereby improve its ride comfort, while at a wave energy harvesting mode, the WHzers are regarded as a point absorber device producing electricity. By means of a rack-pinion unit, the vertical relative displacement between the cabin and the hulls can be transferred into rotational motion of a **Motor/Generator**(**M/G**), which generates electricity. To test the feasibility of the above-mentioned ideas, four types of WHzer have been developed and evaluated since 2008.

1.4.1 Wave Harmonizer Type 1

The first wave harmonizer was developed in 2008 and named as WHzer Type 1. It was a trimaran which had three small hulls and one big submerged float. One suspension unit consisted of a spring and an oil damper, was mounted between the cabin and each small hull. A rack and pinion unit was used to convert the relative displacement between the cabin and the hulls into rotational motion of a flywheel. The structure and components is shown in Fig.1.1(a). It was found that strong dampers had a relatively high efficiency in reducing the motion of the small hulls other than that of the cabin [31].

1.4.2 Wave Harmonizer Type 2

The WHzer Type 2 was a planning hull catamaran. There were two suspension units on each hull. They were symmetrically located in the front and rear part of the hull with respect to the center of buoyancy of the ship. A model ship with length of 1.6 m was developed and teste. The components and structure of this type are given in Fig.1.1(b). A towing tank test was implemented during 2011-2012. The results indicated that the heave and pitch of the cabin were reduced more if the damping coefficient was increased. It also implied that the relative displacement between the cabin and the hulls had large amount of kinetic energy to be reused [32].

1.4.3 Wave Harmonizer Type 3

Instead of oil dampers and flywheels, a so-called electronic damper was formed and applied to the WHzer Type 3 (Fig.1.1(c)). Two stepping motors were employed. Each of them was connected to a load resistor in series, hereby formed an electrical circuit. By tuning the magnitude of the resistor, the current in the circuit varied, hereby the torque produced. In this way the rotational rate of the motor's shafts were adjusted. It had an effect on the angular velocity of a pinion that meshed with a rack, which leading to a change in the relative velocity between the cabin and hulls. It can be seen as an equivalent result that obtained by a viscous damper. A towing test was implemented in 2012. The results showed that the heave and pitch reduction of the cabin increased along with the reduce of the load resistance, which means an increase of the damping coefficient. It also implied a compromise between the motion reduction and energy harvesting was necessary and should be made according to the use of the ship [33].

1.4.4 Wave Harmonizer Type 4

A semi-active motion control system was developed for the WHzer Type 4. The ship structure was similar to the Type 3, except the number of the stepping motors in one control system was increased from one to two as shown in Fig.1.1(d). The control system analyzed the feedback signals of the acceleration of the cabin as well as the relative velocity between the cabin and the hulls, then determined the time of executing the motion-control system. Through which the heave and the pitch of the cabin were reduced, meanwhile the ratio of the harvested energy to the wave energy carried by the crest over the width of the hulls was achieved at a certain level [33].

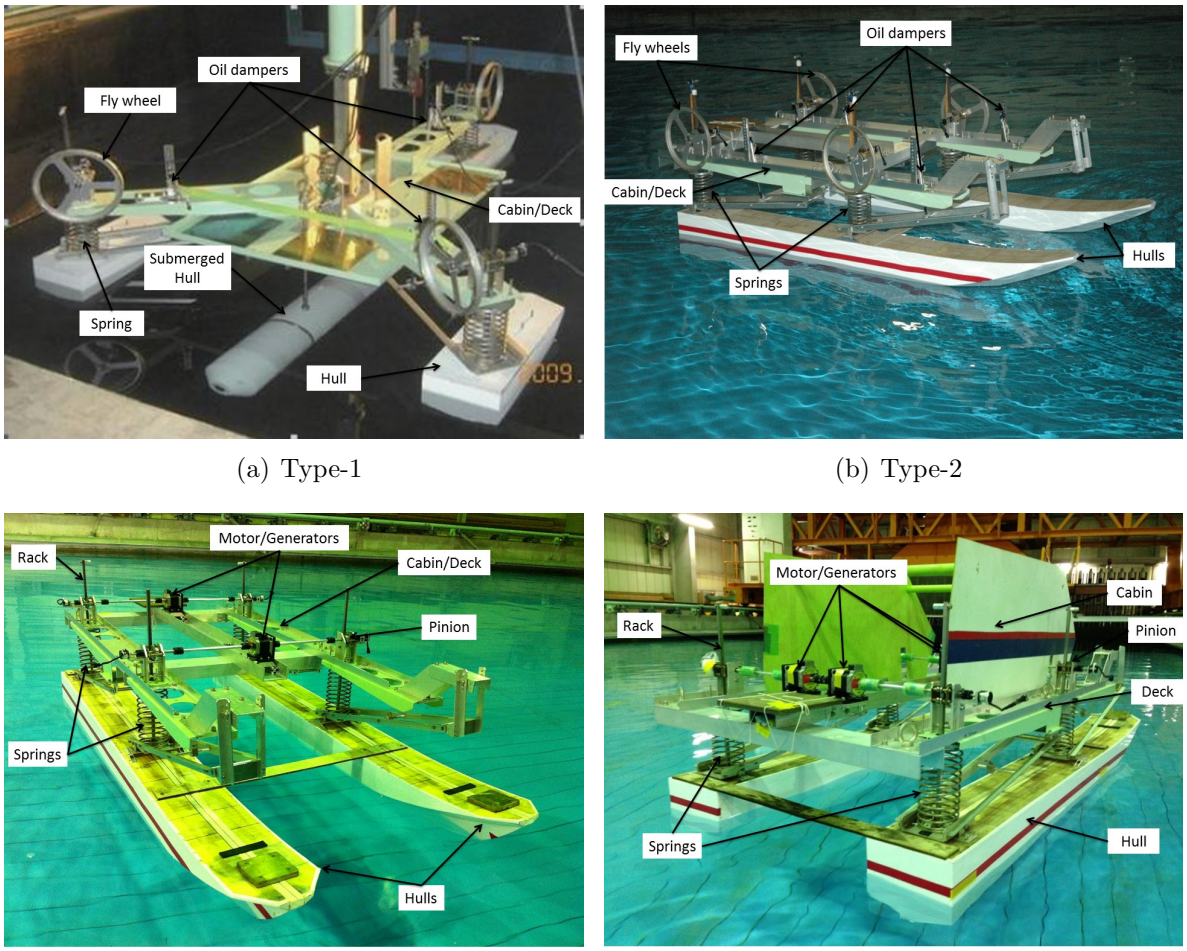

(a) Type-1

(b) Type-2

(c) Type-3

(d) Type-4

Figure 1.1: Components and structure of WHzer Type 1-4

1.4.5 Summary

From Type 1 to Type 4, the motion reduction of each type was investigated by towing tank tests. The wave energy capture ability was numerically estimated in Type 1 and Type 2, and experimentally measured in Type 3 and Type 4. The main conclusions of those studies can be summarized as:

1. suspensions as a part of a ship were proved to be acceptable;
2. catamaran is a suitable ship type;
3. oil dampers mounted between the cabin and the hulls could reduce the heave and pitch motion of the cabin;
4. a rack-pinion unit could effectively convert the relative displacement between the cabin and the hulls to rotational motion of a M/G;
5. an electrical circuit, formed by connecting a M/G and a resistor in series, could work as a damper equivalently. Its damping coefficient in units of Ns/m can be numerically calculated;
6. braking torque produced by the above-mentioned electrical circuit reduced the heave and pitch motion of the cabin at a noticeable level, especially around its resonance frequencies. Meanwhile, the wave energy capture width ratio was promising;
7. the heave and pitch of the hulls may get enlarged at some frequencies because of the force produced by the M/Gs.

1.5 Objectives and Structure

In this research, Wave Harmonizer Type 6 was designed and evaluated. The objectives were to build a feasible and reliable suspension which can not only sustain heave and pitch motion of the cabin, but also the roll motion; to establish effective and robust control systems concerning motion reduction of the cabin and wave energy harvesting under various wave conditions; to investigate and validate the performance of the design concepts of the suspension and control system, consequently acquire the knowledge about the characteristics of the cabin-suspended ship.

Chapter 1 introduces the background of this research, which includes the technologies commonly used to improve ride comfort of the land vehicles and ships, widely developed Wave Energy Converters, the involvement of Wave Harmonizers as well as the main achievements.

Chapter 2 introduces the development procedure of WHzer Type 6. A new design of the suspension was proposed and constructed. It has four modified rack-pinion units which support the roll motion of the cabin; two sets of pantographs and Watt's links that prevent the springs from bending meanwhile guarantee the heave and pitch motion of the cabin. The characteristics of a newly adopted brushed DC motors, the control algorithms for motion reduction and wave energy harvesting were demonstrated.

Chapter 3 elaborates the dry test, which consists of a free decay test, a motor driven test and an on-land forced oscillation test. It explains in detail about the mechanical performance of the suspension design, the heave response of the cabin and the corresponding energy products under a skyhook control and a MPPT control.

Chapter 4 demonstrates a towing tank test under regular wave conditions. The heave, pitch and roll motion response of the cabin and that of the hulls were analyzed under various control modes. The wave energy capture width ratio were evaluated, whose relation with the relative displacement between the cabin and the hulls was investigated.

Chapter 5 discusses the energy flow and distribution at the MPPT mode. The primary and secondary energy conversion efficiency were estimated. A concept, namely encounter wave power, was proposed to adjust the energy carried by the wave crest while viewing from a moving ship.

Chapter 6 concludes the study of WHzer Type 6 in terms of the main achievements, the remained tasks and the future plans.

In the end the references and an appendix about the hydrodynamic characteristics of the displacement hulls were given.

Chapter 2

Design of a Model Ship with 1.6m in Length

2.1 Objectives and Challenges

There were two design sections of Wave Harmonizer Type 6 (WHzer-6). One was the ship structure design section, the other was the control system design section. The objective of the structure design was to develop a flexible suspension system which can support multiple motions of the cabin. That of the control system design was to construct a stable and reliable system to achieve the motion reduction of the cabin, and to obtain the maximum wave power capture ability. To achieve those objectives, there were four technical challenges to be overcame.

1. The first challenge was to restrain undesired relative motions between the cabin and the hulls. Traditional vessels can be seen as rigid body structures, which generate motions in 6 degrees of freedom: translation motion - surge, sway, heave; rotational motion - roll, pitch and yaw. However, due to the springs mounted between the cabin and the hulls, the motions of a wave harmonizer are increased up to 12 DOF. Because both the cabin and the hulls have its own motions in 6 DOF. Phase shift of a motion between the cabin and the hulls, for instance surge, sway and yaw, could yield horizontal twist of the compression springs, which in turn deteriorate the ride comfort and may cause damage of the springs and other suspension components. Therefore, those phase shift should be constrained, meanwhile the heave, pitch and roll motion of the cabin and the hulls should be allowed. In this way, a WHzer can be regarded as a 9 DOF model.

2. The second challenge was to transform vertical relative displacement between the cabin and the hulls into rotational motion of the M/Gs under beam sea or quartering sea condition. Known that from WHzer-1 to WHzer-4, the roll motion of the cabin was not taken into consideration because the suspension structure did not support the roll motion. Therefore, the tests were only implemented under head sea condition. For a more realistic application, the roll motion of the cabin and the hulls should be guaranteed and the motion transformation should be achieved effectively.

3. The third challenge was to select a feasible control algorithm to realize a certain level of motion reduction of the cabin, besides an approach to obtain the maximum wave energy capture ability at a given circumstance.

4. The fourth challenge was to develop an approach to investigate and test the proposed

concept. Since such combination of the cabin-suspended ship with advanced control systems is rare.

2.2 Ship Structure and Specifications

2.2.1 Structure

The components of the structure was given in Fig.2.1. The body can be divided into three segments: cabin segment, suspension segment and hull segment. The **cabin segment** consists of a cabin/deck, four motor/generators (M/Gs), four accelerometers, weight blocks if required and other objects riding above the deck. The **suspension segment** includes the components mounted between the cabin/deck and the hulls, which are four compression springs, four sets of rack-pinion, two sets of Watt's link and two sets of pantograph. The **hull segment** is comprised of two planing hulls, two bridge frame connecting the hulls and weight blocks if required.

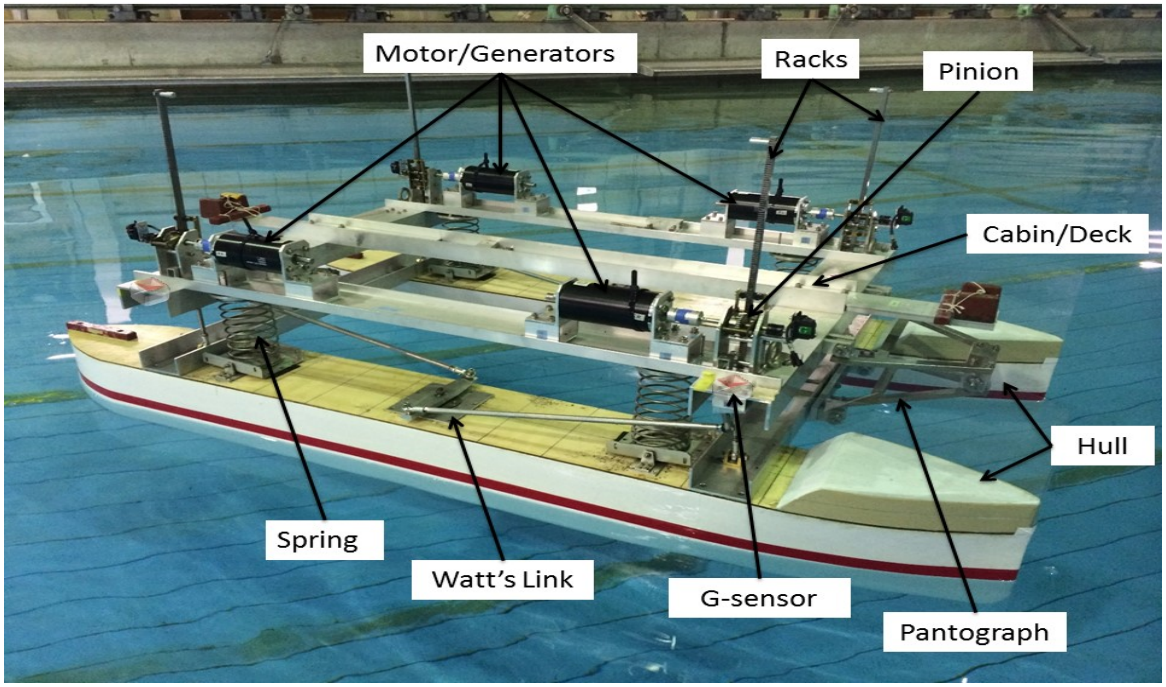

Figure 2.1: Components and structure of WHzer-6

The four springs were mounted between the cabin/deck and the hulls at the four corner of the ship, while the four M/Gs were settled above. For the sake of an easy reference, those corners were named as front-left (**FL**), front-right (**FR**), rear-left (**RL**) and rear-right (**RR**), if the bow was regarded as the front side and the port side was the left side.

At each corner, there was a rack-pinion connecting the hull and the cabin/deck in a way that the rack was vertically fixed on the hull with one end, while its teeth was meshed with that of a pinion. The pinion was fit on the deck and had its shaft connecting to that of a M/G's. Therefore, a vertical motion of the rack can rotate the pinion gear, consequently turn the M/G, and vise versa. This is a mechanism of motion transformation between translation and rotation. A successful application of the mechanism requires the teeth meshing between the pinion and the rack is kept properly.

The aforementioned challenge one and two were solved by modifying the racks, introducing Watt's links and pantographs.

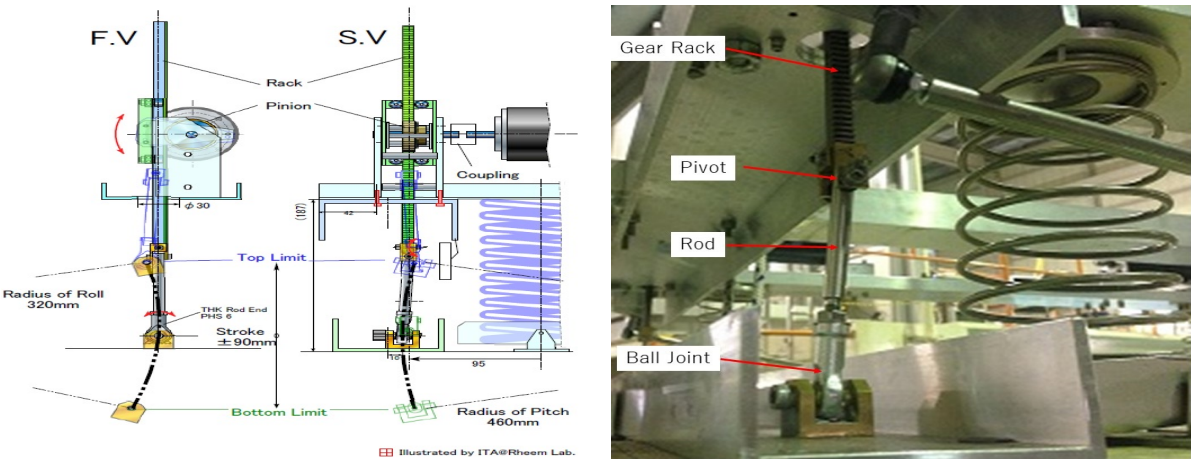

(a) Sketch (b) Photo

Figure 2.2: Sketch and photo of the modified rack

- **Modified Rack**

  A modified rack has four components: a gear rack, a steel rod, a pivot and a ball joint. They were connected in such a way that one end of the rack and the rod were linked together through the pivot, while the other end of the rod was attached with the ball joint that settled on a hull. The detail of the connection was shown in Fig.2.2(b). The pitch motion of the hulls can cause rotational motion of the rod around the pivot, while that of the roll motion causes rotational motion of the rod around the ball joint. Either way of the two could diminish the undesired swing of the gear rack, therefore reduce the risk of the gear teeth dis-meshing.

  Fig.2.2(a) demonstrated the trajectories of the modified rack at the roll motion and the pitch motion, respectively. The limitation of the heave stroke of the cabin is about 0.09 m, therefore with a roll radius of 0.32 m, the limitation of the roll motion of the cabin is about $\pm 16^\circ$ relative to the hulls. That of the pitch motion is about $\pm 11^\circ$ relative to the hulls.

- **Watt's Link**

  Watt's link is a type of the linkages whose central moving point can be approximately regarded as a straight line. It is widely used in rotatory beam engines to increase its power supplement, and in automobile suspensions to prevent relative sideways motion between its axle and car body. In this application, the central point of a Watt's link was fixed on a hull, while the ends of its two longer rods were attached to the bottom of the deck. In this way, the heave motion of the cabin can be guided by a rotational motion of the short rod of the Watt's link around the center point, while the pitch motion of the cabin can be guided by the longer rods. Meanwhile the Watt's links can also restrain the relative motion in terms of surge and sway between the cabin and the hulls.

- **Pantograph with Roll Pivot**

  Pantograph is a linkage originally used to produce identical movements at a given ratio by its arms, which can also be used as extension arms. There are two pantograghs employed in WHzer-6. Each pantogragh has two arms, one was attached to the deck, and the other to the hull bridge. The arm attached at the deck was fixed directly at its two ends, while the one attached to the hull bridge was not. Its two ends were linked by a rod whose

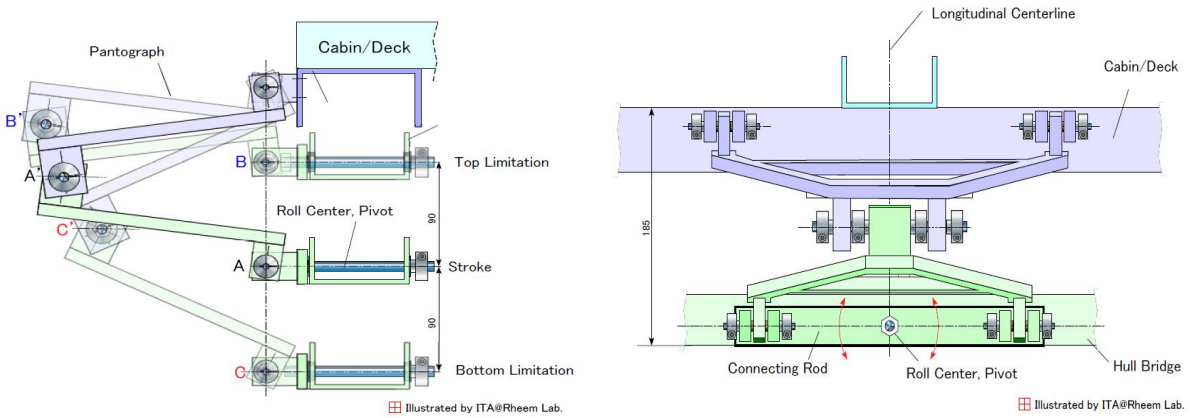

(a) Side View (b) Front View

Figure 2.3: Sketch of the Pantograph

center was connected to the hull bridge through a pivot. In this way, the rolling center of the cabin was located at the position of the pivot. A sketch was depicted in Fig.2.3. Meanwhile, the pantograph can also restrain the relative sideways motion in terms of the yaw between the cabin and the hulls.

2.2.2 Specifications

The specifications of the ship components were shown in Table 2.1. The mass of the suspension segment was assumed to be equally distributed into the cabin segment and the hull segment, which were called the sprung mass and the unsprung mass, respectively. A load shaft was only set on the deck to acquire motion data of the cabin in towing tank test, therefore it was not included in the total weight of the ship unless a towing tank test was considered.

Table 2.1: Specifications of the Structure of WHzer-6

Symbol	**Value**	**Unit**	**Description**
M_T	45.0	kg	Total mass of the ship
M	31.9	kg	Mass of the upper part of the ship (sprung mass)
m	13.1	kg	Mass of the lower part of the ship (unsprung mass)
M_{LS}	2.78	kg	Mass of the load shaft used in towing tank test
L	1.600	m	Length of the ship
B	0.825	m	Width of the ship
b	0.185	m	Width per hull
D	0.105	m	Draft of the ship
k	615.0	N/m	Compression spring constant
k_{33}	5239	N/m	Restoring force constant of two hulls
η_c	$\pm$0.09	m	Stroke limitation of the cabin from the rest position
θ_c	$\pm$11.2	deg	Pitch limitation of the cabin relative to the hulls
ψ_c	$\pm$16.1	deg	Roll limitation of the cabin relative to the hulls

A top view and a side view of the structure were given in Fig.2.4. The dimension of the ship and distances between main components were depicted in details.

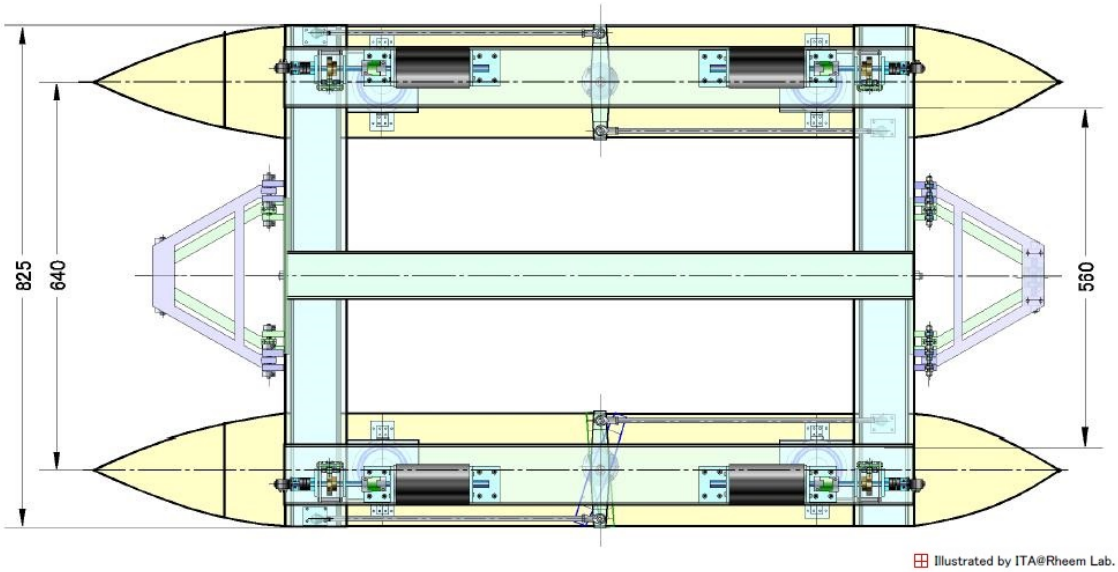

(a) Top View

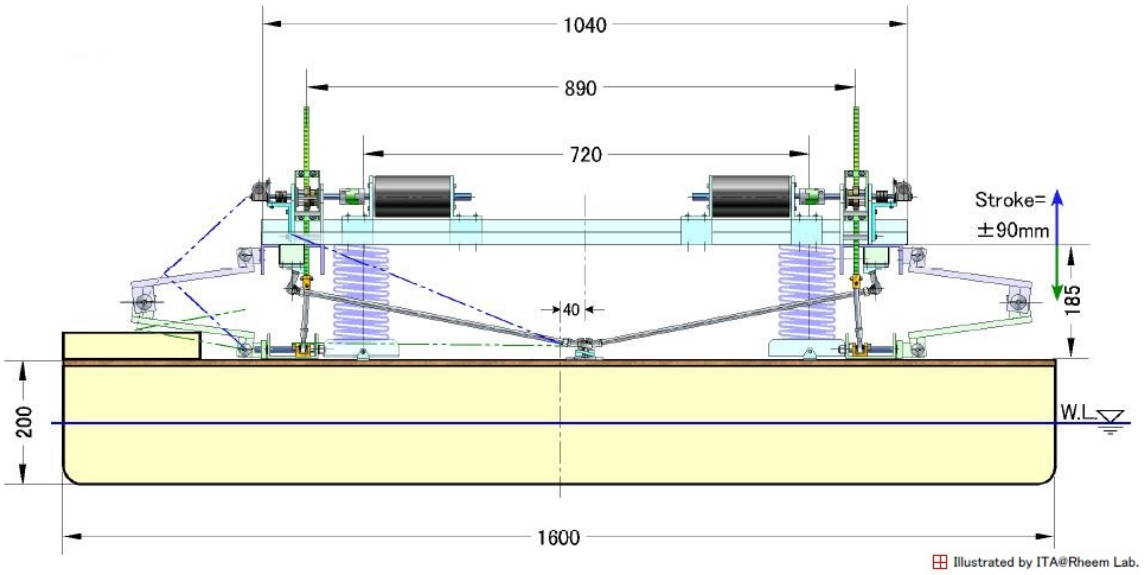

(b) Side View

Figure 2.4: Sketch of the ship structure

2.3 Control System

2.3.1 Brushed DC Motor/Generator

The requirements for a Motor/Generator used in the control system should have high efficiency as a motor to produce torque, and as a generator to convert kinetic energy into electricity. Thus, the ideal M/G should have a low winding resistance which causes less energy loss, and a high torque coefficient which provides large torque if needed.

An electric print motor PMFE-12CBB, made by YASKAWA Japan, and a brushed DC motor Maxon-353300, made by Maxon Japan Co. Ltd, were selected and tested. After a motor effect test and a generator effect test, the Maxon DC motor showed a more reliable and accurate results with respect to the internal resistance and torque constant. Hence, Maxon DC motor was adopted. The specifications of which were given in Table 2.2, and a profile of the motor was shown in Fig.2.5.

Table 2.2: Main specifications and characteristics of the brushed DC motor

Description	**Value**	**Unit**
Nominal voltage	70	V
Nominal current	3.91	A
Nominal torque	0.83	Nm
Stall torque	1.45	Nm
Terminal resistance	1.06	Ω
Terminal inductance	5.1	mH
Torque constant	0.219	Nm/A
Rotor inertia	1.28×10^{-4}	kgm^2
Number of pole pairs	2	–
Weight of motor	2.48	kg

Figure 2.5: Brushed DC motor Maxon-353300

2.3.2 Skyhook Control and PID controller

Given a mass-spring-base structure, an ideal skyhook control describes a situation that any disturbance of the mass transmitted from the base could be counteracted by a damper, whose one end connects to the mass and the other to a fixed point in the sky. The damping coefficient can be automatically and perfectly tuned according to the disturbance so as to prevent the mass from oscillating.

However, in reality such fixed point in the sky does not exist, therefore a skyhook-like control was proposed. Instead of using dampers, motor/generators are commanded to generate force to suppress the disturbance transmitted from the hulls.

It works in such a way that when a spring starts to expand or contract from its neutral length, the M/G produces force to restrain it (motor mode); when the spring expands or contracts towards its normal length, the M/G absorbs the kinetic energy and converts it into electricity (generator mode). As a result, the external force acting on the cabin can be transferred to the rotational motion of the M/G, hereby cause no oscillation of the cabin.

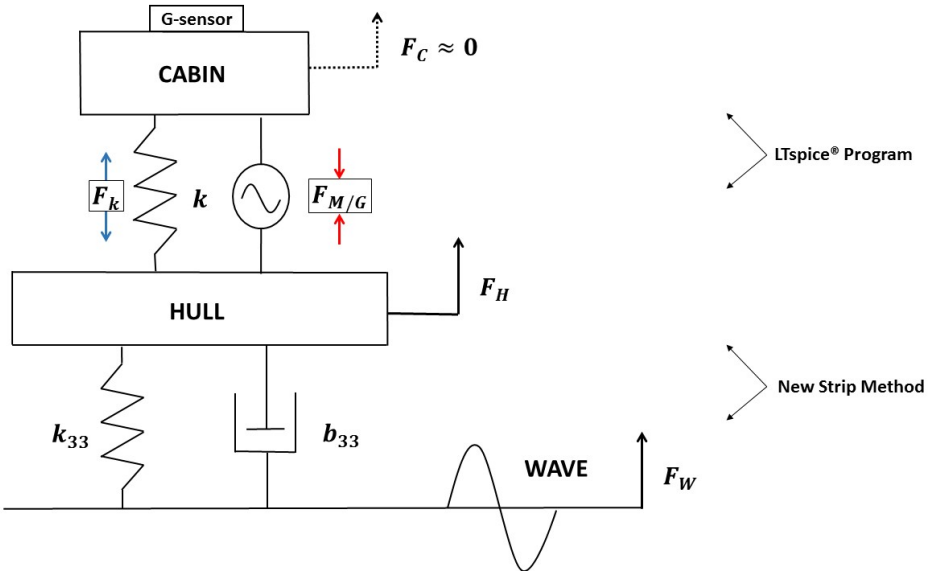

Figure 2.6: Skyhook-like dynamic sketch

A dynamic configuration of the skyhook-like concept was showed in Fig.2.6. The hydrodynamic coefficient and wave exciting force were estimated by New Strip Method (see Appendix A), while the interaction between the cabin and the hulls was formed and simulated by using the LTspice®, which was introduced in section 2.4.

Assuming the hull receives a force F_H, pointing upward. Part of the force is stored by the spring with a certain distance of compression, denotes F_K. The rest part of the force is acting on the cabin denotes F_C. To remain the cabin being still, the motor should produce a force $F_{M/G}$ which equals to F_C in magnitude but of opposite direction. In the control system, this is realized by a PID controller with an error signal of the difference between an absolute vertical acceleration of the cabin and a reference acceleration.

A **PID controller** consists of a proportional term, a integral term and a derivative term, which is based on a control loop feedback mechanism. PID is an abbreviation of proportional, integral and derivative. An error value is continuously calculated as a difference between a measured variable and a predetermined set point. Then, the error is sent to the proportional

term, the integral term and the derivative term, respectively. As a result a correction of the control variable is done, which consequently induces a new error and another correction. This procedure repeats continuously until the error is negligible.

Denote an error value as $e(t)$, a control variable as $u(t)$, a PID controller can be expressed as

$$u(t) = K_p e(t) + K_i \int_0^t e(\tau)d\tau + K_d \frac{de(t)}{dt} \tag{2.1}$$

in which, K_p, K_i and K_d represent the gain of the proportional term, the integral term and the derivative term, respectively; t is the present time, τ is the variable of integration with a range from the initial time 0 to the present time t. This transfer function can also be written in the Laplace domain

$$K_(s) = K_p + \frac{K_i}{s} + K_d s \tag{2.2}$$

in which s is the complex frequency.

Depending on the design of a controller, a combination of the proportional term, integral term and derivative term can be used. Eliminating a control term can be done by setting its gain as 0. The characteristics of each control term can be summarized as:

- **Proportional Term**

  A proportional term accounts for the errors at present. Its output is a product of the P gain K_p and the current error values. A high proportional gain causes a large change of the output comparing to a given change in the error. However, if the gain is too high, a hunting of the control variable about the control set point can be generated, which leads to an unstable situation of the system. In contrast, if the gain is too small, the controller is less sensitive to the error values, hence results in less efficiency of the control system. A proportional controller may result in a steady-state error, which is the difference between the input error and the output response of a system if time goes to infinity. This problem can be solved by adding an integral term to the controller.

- **Integral Term**

  An integral term accounts for the errors at past. It calculates a sum of the errors from the initial time 0 to an instantaneous time t, which results in an accumulated value that should have been corrected. This value multiplies an integral gain K_i yields an output of the integral term. Since an integral term takes all the past errors into consideration, it accelerates the procedure of the output towards to the set point, but with an expense of causing overshoot.

- **Derivative Term**

  A derivative term accounts for the predicted errors in the future, which is based on the current error variance trend. The output of a derivative term is a product of a derivative gain and the gradient of the error over time, which can be a negative or positive value. It is used to predict the behavior of a control system, which could save settling time and improve the stability of the system. However, high frequency noise in the errors turn to cause a high frequency fluctuation of the output of a derivative controller, which can be eased by using a low-pass filter.

Figure 2.7 showed a simple sketch of a plant with a PID controller, in which $y(t)$ represents the plant response or system response. The overall transfer function of this system can be written as

$$H(s) = \frac{K(s) \cdot G(s)}{1 + K(s) \cdot G(s)} \tag{2.3}$$

in which $G(s)$ and $K(s)$ is the transfer function of the plant and the controller, respectively. It is known that unstable situation of the system can be observed if the $H(s)$ is diverged at a complex frequency, specifically if $K(s)G(s) = -1$.

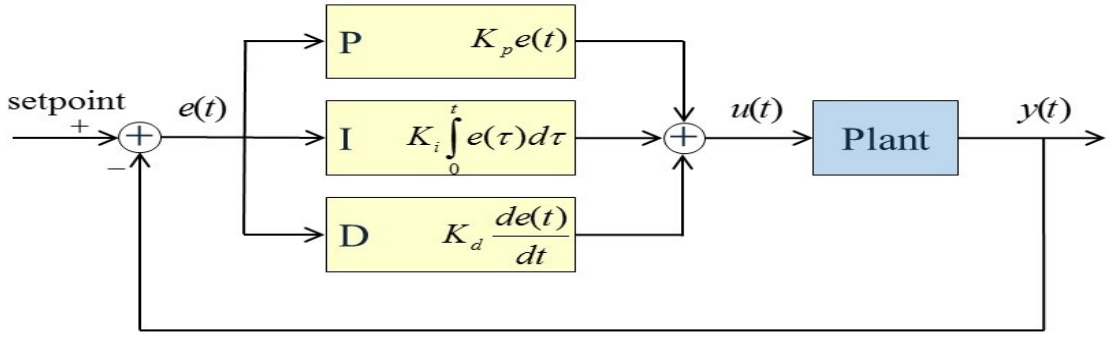

Figure 2.7: Sketch of a PID controller

In WHzer-6, only an integral term was employed. Its control variable is the acceleration of the cabin. The setpoint is $0\,\mathrm{m/s^2}$, thus the error of the I controller is the difference of the cabin acceleration from $0\,\mathrm{m/s^2}$. A control flow chart was given in Fig.2.8. The output of the I controller is an applied voltage to a M/G. If it is larger than the electromotive force, a certain amount of torque can be produced, which then acts on the cabin and the hulls through a rack-pinion unit, consequently modifies the motion of the cabin and the hulls, therefore results in a new acceleration of the cabin. This acceleration is detected by a G-sensor then sent back to the I controller. Such procedure is repeated until the acceleration reaches the set point.

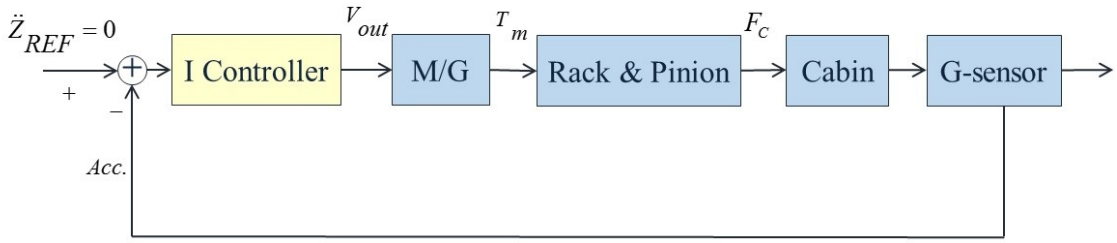

Figure 2.8: Control flow chart of WHzer-6 with an I controller

Known that there are four suspension systems distributed at FL, FR, RL and RR of the model ship. Each of the suspension system has an identical I controller. The control mechanism was the same as described in Fig.2.8. The acceleration was detected at the deck above each suspension system. The four I controllers can be regarded as independent with each other, because it only accounts for its local acceleration of the cabin. In other words, each controller

produces its own applied voltage to the M/G. It was assumed that if the four I controllers reached their stable state, so did the cabin.

Loop tuning of the I controller was done manually associated with a bench test. Although for a towing tank test, the controllers at the front and the rear under a head sea condition, or that at the starboard side and the port side under a beam sea condition, may require different gain setting, in this fundamental investigation the gains of the four controllers were set identically at a time so as to get a basic insight of the characteristics of the motion response and the requirements of parameter settings. In this way, a simulation program can be simplified to a quarter-model program, which deals with only one suspension system with a quarter mass of the cabin segment as well as the hull segment.

2.3.3 Maximum Power Point Tracking and Impedance Matching

Maximum power point tracking (**MPPT**) is a technique commonly used for wind turbines and solar panels. It describes a process of finding an electronic load setting for a controller to obtain its maximum power extraction ability at a given environmental condition. The electronic load settings to obtain maximum power are called maximum power points (**MPPs**). In the energy harvesting mode of the WHzer-6, the MPPs were obtained by an approach named impedance matching.

The maximum power transfer theorem states that to reach the maximum amount of power transfers from a source to a load, the impedance of the two must be a pair of complex conjugates. Specifically, if the source only has resistance components, then the load should also have only resistance components with the magnitude equals to that of the source. If the source has both resistance components and reactive components, such as capacitor and inductor, then the load impedance should be a complex conjugate with that of the source.

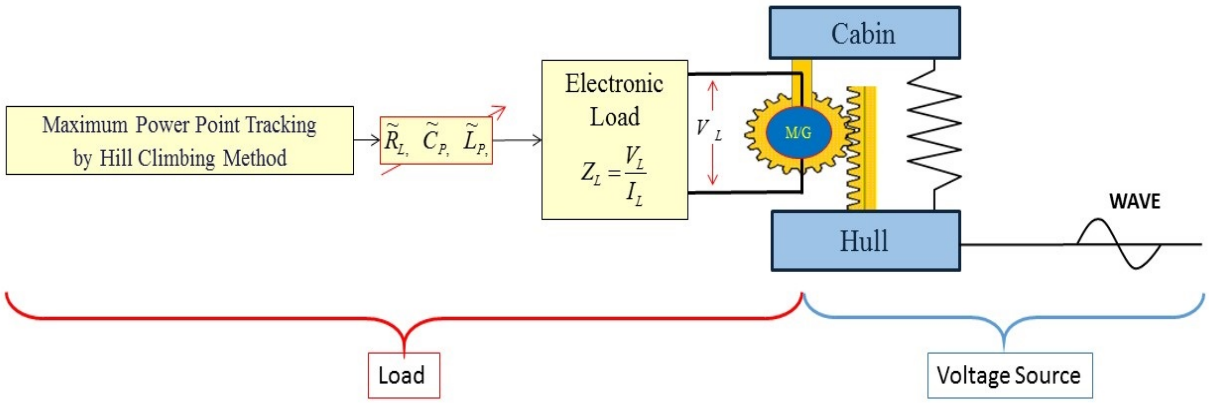

Figure 2.9: Sketch of a source and a load

As depicted in Fig.2.9, the wave induced relative motion between the cabin and the hulls can be regarded as a voltage source, while a resistor, a capacitor and an inductor compose of an electronic load. Known that the relative motion can be converted into the rotational motion of the M/G through a rack-pinion unit, the **mechanical impedance** can be seen as the impedance of the voltage source as view from the terminals of the M/G. According to the maximum power transfer theorem, a MPP is obtained if the impedance of the electronic load is a complex conjugate of the mechanical impedance. It is called **impedance matching**.

One of the approaches to seek the MPPs is **hill climbing method**. It works in such a way that tuning a parameter of the electronic load at a certain direction, if the obtained power is increased then continually tuning in that direction; otherwise reverse the direction until the power turns to be decreased on both of the direction. A limitation of this method is that the seeking might stop at a local peak but not the overall maximum point. To avoid this, the range of tuning should be set as large as possible.

The power delivered from the source to the load can be expressed as

$$P_L = \frac{1}{2} Re\left\{V_L \cdot I_L^*\right\} \tag{2.4}$$

$$= \frac{1}{2} Re\left\{\left(V_S \cdot \frac{Z_L}{Z_S + Z_L}\right)\left(\frac{V_S}{Z_S + Z_L}\right)\right\} \tag{2.5}$$

$$= \frac{1}{2}|V_S|^2 \frac{Re\left\{Z_L\right\}}{|Z_S + Z_L|^2} \tag{2.6}$$

in which V_S is the source voltage, Z_S and Z_L are the source impedance and load impedance, respectively. The impedance can also be written in forms of a combination of resistance and reactance, which are

$$Z_S = R_S + jX_S \tag{2.7}$$

$$Z_L = R_L + jX_L \tag{2.8}$$

The maximum P_L, therefore, is obtained if

$$Z_S = Z_L^* \tag{2.9}$$

It implies that the maximum power transfer efficiency from a source to a load is 50%. In other words, half of the source power is transferred to a load, half of the power is dissipated in the source. Known that the impedance is frequency-dependent variable, to achieve impedance matching, the magnitude of the electronic load components are frequency-dependent as well. A simulation program, built by using LTspice®, was implemented to seek the MPP at a given frequency. More details were introduced in section 2.4.2.

2.3.4 Integrated Control

An integrated control is a combination of the skyhook control and the energy harvesting control. It is regarded as a pre-investigation of the relation between the energy production of the M/Gs and the motion response of the cabin, which serves for the optimization of the control system.

The command voltage from the skyhook control and that from the energy harvesting control were multiplied by an impact factor, respectively, before they were summed up as a new command voltage applied to a M/G. The contribution of a control mode is adjusted by tuning the magnitude of the impact factor.

Defined by the direction of a M/G rotates and the current flows, the operations of a M/G can be depicted in a quadrant diagram as shown in Fig.2.10. A cell symbol, named as source term, represents the command voltage from a control system; an adjustable cell symbol with a outer circle, named as M/G term, represents the electromotive force produced by rotational motion of the M/G; R_w represents the winding resistance of the M/G, x axis of the diagram represents the current through the electrical circuit, clockwise as positive; y axis represents the angular velocity of the M/G, clockwise as positive.

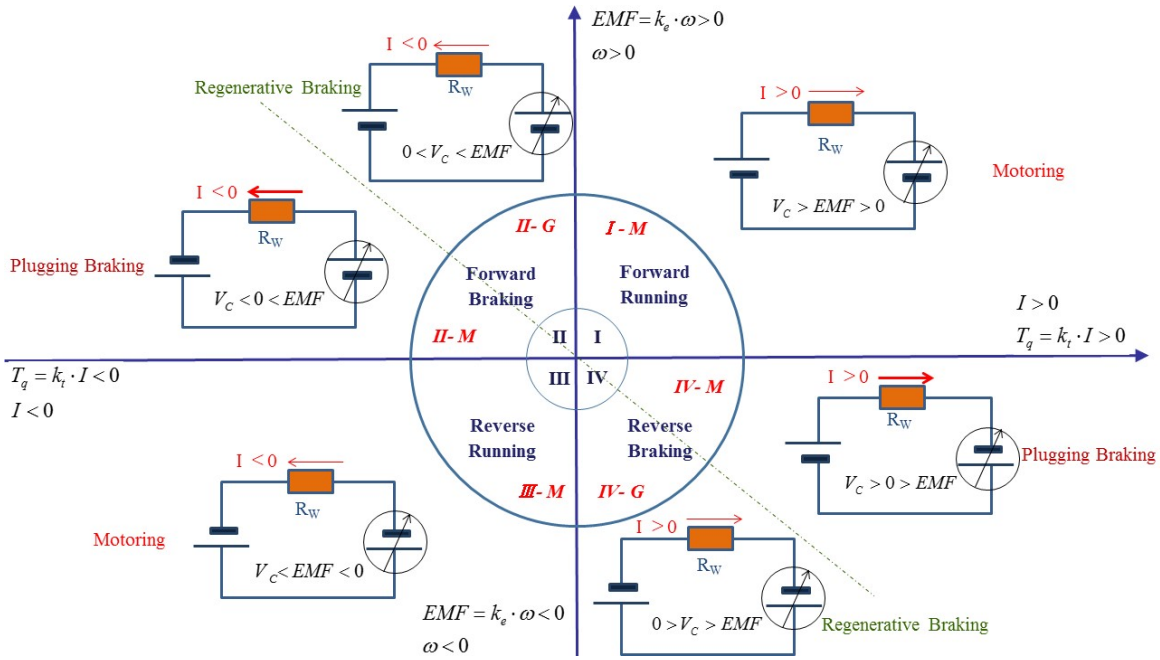

Figure 2.10: Operation quadrant diagram of the M/G

- **Electromotive Force** (EMF)
  The electromotive force, denotes as EMF, is the amount of voltage induced by rotational motion of a M/G. It is proportional to the angular velocity of the rotation, known as

$$EMF = K_e \cdot \omega \tag{2.10}$$

  in which, k_e represents the EMF constant, in units of Vs/rad.

- **Motor Command Voltage** (V_c)
  The motor command voltage is the output signal from the controller. At the skyhook mode, it is aiming to minimize the motion of the cabin; at the energy harvesting mode, it is used to achieve impedance matching hereby obtain the maximum energy capture ratio; at the integrated control mode, it is a combination of the above-mentioned modes.

- **Torque** (T_q)
  Torque produced by a M/G exerts a force acting on the cabin and the hulls as an action and reaction force pair, which regulates the motion of the cabin and the hulls. It is proportional to the current flow through a M/G, which can be written as

$$T_q = K_t \cdot I \tag{2.11}$$

  in which, K_t represents the torque constant, measured in Nm/A. It is numerically equals to K_e according to the law of energy conversation.

- **First Quadrant** ($I - M$)
  In the first quadrant, the M/G is under forward running condition. Both the V_c and EMF are positive values, and V_c is larger than EMF. The current flows in the direction from the source term to the M/G term, driving the M/G rotates clockwise, thus with motor effect in domination. The rotation is accelerated at beginning, then reaches a constant rate and obtains its equilibrium state.

- **Second Quadrant ($II-G$, $II-M$)**
  The second quadrant is under forward braking condition aiming to slow down the rotation of the M/G. At high rotation rate, reducing the voltage from the source term until it below that of the EMF but above 0 V, the current changes its direction, simultaneously the action of the torque varies from driving the M/G rotates to braking, meanwhile, kinetic energy is converted into electricity charging the source term. As it continues the rotation rate reduces, until it reaches an equilibrium state. This braking method is called **regenerative braking** with generator effect in domination. It is normally used on a system which has large inertia, such as the electric trains. A quick braking can be achieved by reverse the poles of the source term, by doing so, the source term and the M/G term act at the same direction, result in a large current hereby a significant torque. It is called the **plugging braking** with motor effect in domination, which is normally used in the field of elevator control or machine tools control. In general, the regenerative braking produces electricity but takes a relative long time to slow down a system, in contrast, the plugging braking diminishes motion quickly with an expense of dissipating more energy by the winding resistance of a M/G.

- **Third Quadrant ($III-M$)**
  The third quadrant is analogous to the first quadrant, the M/G is under reverse running state. Both the V_c and EMF are negative values, while V_c is larger than EMF. The current flows in the direction from the M/G term to the source term, driving the M/G rotates anticlockwise, thus with motor effect in domination. The rotation is accelerated at beginning, then reaches a constant rate and obtains its equilibrium state.

- **Forth Quadrant ($IV-G$, $IV-M$)** The forth quadrant is analogous to the second quadrant, but with the motor rotates in the direction of anticlockwise. It is called the reverse braking. At high rotation rate, reducing the voltage of the source term until it below the EMF, the current flows from the source term towards the M/G term. The kinetic energy is converted into electricity, meanwhile the rotation slows down. To achieve a fast braking, reversing the poles of the source term could produce a large current in the circuit and simultaneously a big torque to eliminate the rotation.

At the skyhook mode, the M/Gs are mainly acting at the plugging braking and running conditions: $I-M$, $II-M$, $III-M$ and $IV-M$, however, in the plugging braking conditions the winding resistances dissipate large amount of energy due to large current, known as $P_w = I^2 R_w$. At the MPPT mode, resonance of the cabin is supposed to be produced which results in a relative high rotation rate. The M/G is under regenerative braking condition: $II-G$ and $IV-G$. It captures energy but sacrifices the ride comfort. Therefore, an integrated controller is used to investigate the relation between energy harvesting and ride comfort, which can provide a perspective on system optimization.

2.4 Electrical Circuit of the Control System

The electrical circuit of the skyhook control and the energy harvesting control was depicted in Fig.2.11, which demonstrated the principle of parameter tuning. Those circuit represented only one control system which works with one M/G and one suspension unit. In other words, four control systems were used in the model ship. The design of the circuit was based on the function of wave energy harvesting, later on that of the skyhook was considered. Since the energy harvesting mode only counts of the rotational rate of the M/G that connected, therefore it was regarded as a local concentrated mode. This characteristics was hold by the skyhook mode as well, which means the four control systems worked independently. The advantage of this redundant design is that the risk of the system break down can be greatly reduced. Failure on one of the four control system would not bring significant effect on the whole ship. Moreover, it shortened the development time of the control system.

At a skyhook mode, the input signal is the acceleration of the cabin, the output of the integrator as shown in Fig.2.11, which can be expressed as

$$G_{int}(j\omega) = -\frac{R_2}{R_1} \cdot \frac{1}{1 + j\omega R_2 C_3} \tag{2.12}$$

in which, the product of R_2 and C_3 represents time constant of the incomplete integrator. The Laplace transform gives

$$G_{int}(s) = -\frac{100}{s + 0.5} \tag{2.13}$$

At an energy harvesting mode, the input signal is the current of the M/G. A feedback resistor R_f and feedback capacitor C_f were tuned to achieve impedance matching between the mechanical system and the electrical system. The impedance can be written as

$$Z_e = C_f \shortparallel R_f \tag{2.14}$$

An **impact factor** of the skyhook control and energy harvesting control is defined as

$$G_{sky} = \frac{R_4}{R_{sky}} \tag{2.15}$$

$$G_{MPPT} = \frac{R_4}{R_{har}} \tag{2.16}$$

Tuning G_{sky} varies the overall gain of the I controller; while for G_{MPPT} the value of 1 represents a MPP condition. Other values draw the control deviates from its MPP condition. It was used as a tool to validate the maximum power harvesting settings.

The motor control circuit was given in Fig.2.12, which demonstrated the mechanism of action among a G-sensor, a control system and a M/G.

For the skyhook control circuit, the acceleration of the cabin was detected by a G-sensor ($SCA1020$), whose sensitivity is about $0.122\,\mathrm{V/(m/s^2)}$. It was filtered by a low pass filter before sending to the skyhook controller.

For the energy harvesting circuit, the current through the M/G was estimated in such a way that a resistor R_{18} was connected to the M/G in series meanwhile its other end was grounded, so the current through the resistor can be regarded as that through the M/G. Known that $R_{18} = 0.1\,\Omega$, therefore the voltage magnitude of R_{18} is always one tenth of the current mathematically. With this solid relation, the voltage was used as a representation of the M/G current, which was sent to energy harvesting circuit.

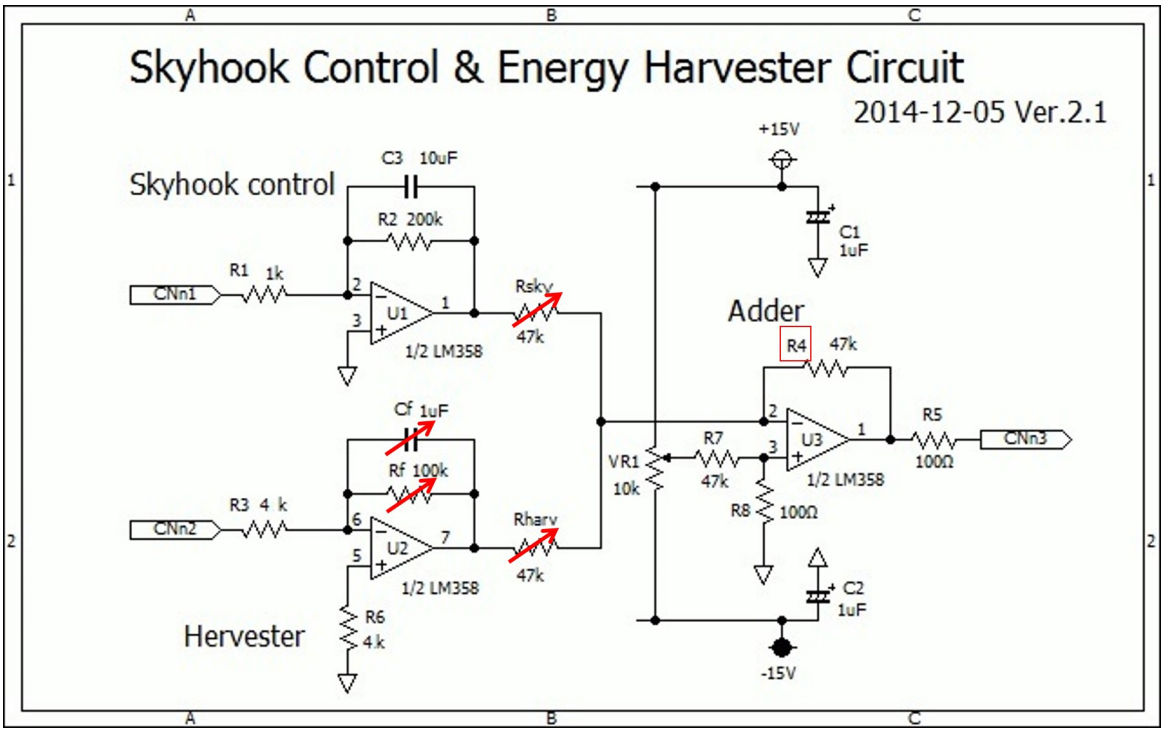

Figure 2.11: Parameter tuning circuit

The gain of the voltage applied to the M/G comparing to the correcting voltage generated by the skyhook and that by the energy harvester circuit was 4. Denote CTRLIN as V_{in}, the gain was obtained by

$$G_{op} = \frac{V_{in} + \frac{R_{15}}{R_{16}} \cdot V_{in}}{V_{in}} = 4 \tag{2.17}$$

Known that the gain of the adder stage as shown in Fig.2.11 is -1, therefore, the overall gain of the skyhook circuit can be written as

$$\boxed{G_i = -0.122 \cdot 100 \cdot 4 \cdot \frac{47}{R_{sky}} \cdot (-1) = \frac{2294}{R_{sky}}} \tag{2.18}$$

The impedance obtained by the circuit can be written as

$$Z_{elc} = \frac{1}{10} \cdot 4 \cdot \frac{C_f \,\|\, R_f}{R_3} \cdot \frac{R_4}{R_{har}} \tag{2.19}$$

The Laplace transform of which gives

$$\boxed{Z_{elc}(s) = \frac{10^{-4} R_f}{1 + sR_f C_f} \cdot \frac{47}{R_{har}}} \tag{2.20}$$

in which the units of the R_{sky} and R_{har} are $\mathrm{k}\Omega$, that of the feedback resistor and the capacitor are Ω and F, respectively.

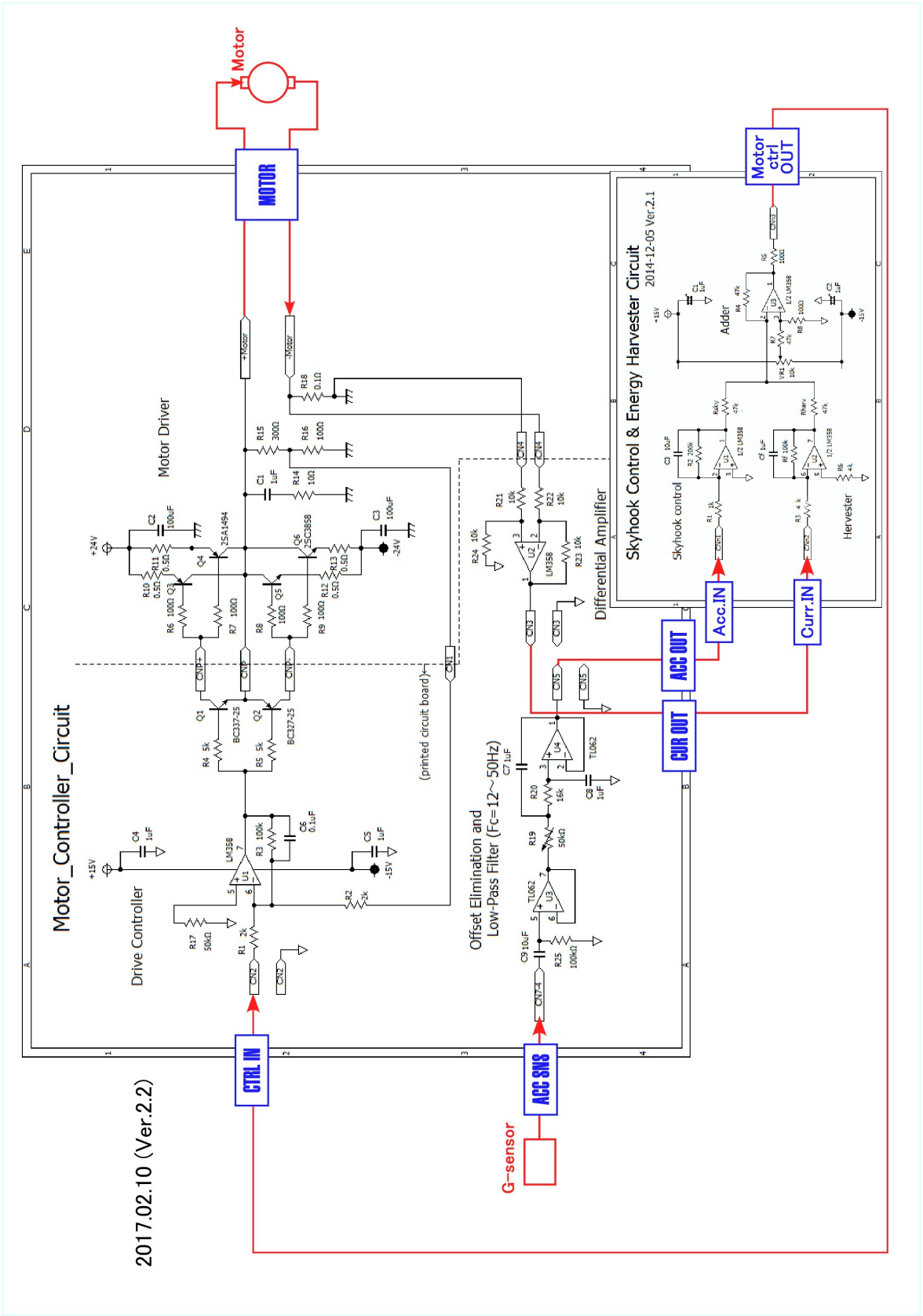

Figure 2.12: Control circuit of one M/G

2.5 Quarter Ship Simulation Program Based on LTspice®

A simulation model with one degree of freedom was built by using **LTspice®**, which is an open source analogue electronic circuit simulator produced by the semiconductor manufacturer Linear Technology (LTC).

2.5.1 Analogy Rules

There are two common methods to achieve an analogy between a mechanical system and an electrical system. One is impedance analogy, the other is mobility analogy. Those definitions are quite straightforward. It can be viewed in such a way that if a mechanical impedance is analogous to that of an electrical system, it is called impedance analogy; otherwise if it is analogous to the admittance of an electrical system, it is called mobility analogy.

Mechanism sketches of a mechanical system and RLC circuits of an electrical system, which have its components either in series or in parallel, were shown in Fig.2.13. A mechanical system consists of a spring k, a damper b and a mass m. Define that exerting a given force $F_1(t)$ with a velocity of $v_1(t)$ at one end of the mechanical system, would yield a certain displacement of each components with velocity of $v_c(t)$, $v_b(t)$ and $v_m(t)$, respectively. A RLC circuit consists of an inductor L, a resistor R and a capacitor C. Define that applying a given current I to the circuit would produce a certain voltage at each electrical component with magnitude of $V_L(t)$, $V_R(t)$ and $V_C(t)$, respectively.

In a mechanical system, which has a spring, a damper and a mass connected in series, the flow variable is the external force $F_1(t)$ and the effort variable is the velocity $v_1(t)$. The mobility, also known as admittance, of the mechanical system can be expressed as

$$\frac{1}{Z_{mec}} = \frac{v_1(t)}{F_1(t)} \tag{2.21}$$

$$= \frac{v_c(t) + v_b(t) + v_m(t)}{F_1(t)} \tag{2.22}$$

$$= \frac{v_c(t)}{k \cdot s^{-1} v_c(t)} + \frac{v_b(t)}{b \cdot v_b(t)} + \frac{v_m(t)}{m \cdot s v_m(t)} \tag{2.23}$$

$$= sk^{-1} + b^{-1} + s^{-1}m^{-1} \tag{2.24}$$

in which, s is the Laplace operator, $Z_{mec}(t)$ is the mechanical impedance of the system, which is the reciprocal of its mobility.

In the case that a mechanical system has a spring, a damper and a mass connected in parallel, the flow variable and the effort variable turn to be the velocity $v_1(t)$ and the external force $F_1(t)$, respectively. The impedance of which can be written as

$$Z_{mec} = \frac{F_1(t)}{v_1(t)} \tag{2.25}$$

$$= \frac{F_c(t)}{v_c(t)} + \frac{F_b(t)}{v_b(t)} + \frac{F_m(t)}{v_m(t)} \tag{2.26}$$

$$= \frac{k \cdot s^{-1} v_c(t)}{v_c(t)} + \frac{b \cdot v_b(t)}{v_b(t)} + \frac{m \cdot s v_m(t)}{v_m(t)} \tag{2.27}$$

$$= sm + b + s^{-1}k \tag{2.28}$$

For a RLC circuit having a resistor, an inductor and a capacitor connected in parallel, the flow variable is the current and the effort variable is the voltage. Its admittance can be written

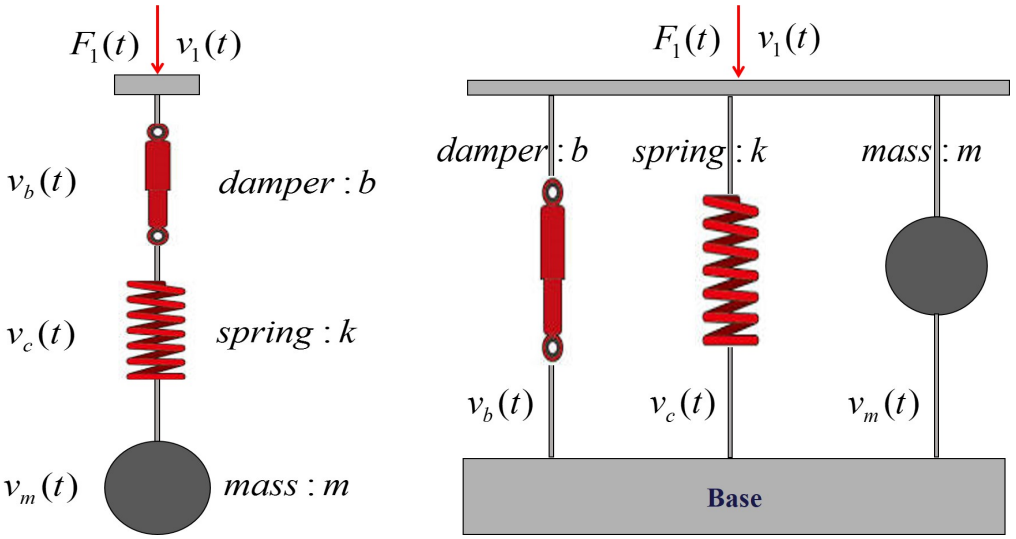

(a) Mechanical system in series

(b) Mechanical system in parallel

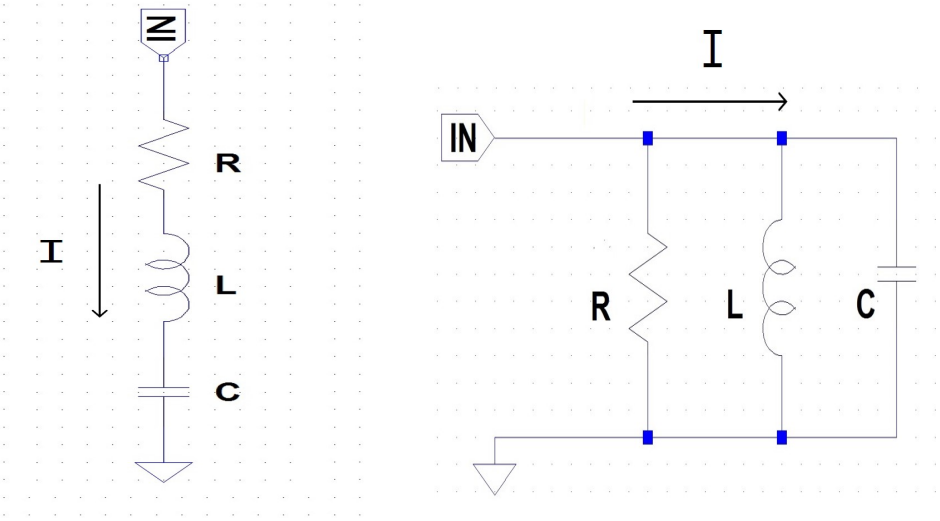

(c) Electrical system in series

(d) Electrical system in parallel

Figure 2.13: Analogy between a mechanical system and an electrical system

as

$$\frac{1}{Z_{elc}} = sC + R^{-1} + s^{-1}L^{-1} \tag{2.29}$$

In the case that a RLC circuit having a resistance, an inductor and a capacitor connected in series. The flow variable and the effort variable are the voltage and the current, respectively. Its impedance can be written as

$$Z_{elc} = sL + R + s^{-1}C^{-1} \tag{2.30}$$

An **impedance analogy** is realized by letting the mechanical impedance analogous to that of the electrical, or the mechanical mobility analogous to the electrical admittance. A mobility analogy is obtained by letting the mechanical impedance analogous to the electrical admittance, or the mechanical mobility analogous to the electrical impedance. Those relations can be summarized in Table 2.3.

Table 2.3: Analogue parameters in a mechanical system and an electrical system

Analogy Rule	**Damper** b	**Spring** k	**Mass** m	**Parallel**	**Series**	**Force**	**Velocity**
Impedance	R	C^{-1}	L	Series	Parallel	Voltage	Current
Mobility	R^{-1}	L^{-1}	C	Parallel	Series	Current	Voltage

Specifically, comparing Eq.(2.29) to Eq.(2.24), and Eq.(2.30) to Eq.(2.28), one may find that an impedance analogy allows a capacitor to represent a spring whose magnitude are reciprocal, a resistor to represent a damper and an inductor to represent a mass. In this way, a mechanical system in parallel is analogous to an electrical system in series, while a mechanical system in series is analogous to an electrical system in parallel. The advantages of this analogy is that the mathematical relations in the electrical domain is identical to that in the mechanical domain.

Comparing Eq.(2.24) to (2.30), and Eq.(2.28) to Eq.(2.29), one can find that a spring, a damper and a mass in a mechanical system can be represented by an inductor with reciprocal value, a resistor with reciprocal value and a capacitor with the same value, respectively. In this way a mechanical system in parallel can be represented by an electrical system in parallel, while that in series is represented by an electrical system in series. This is called **mobility analogy**, the characteristics of which is that the mechanical network can be arranged similarly to its analogous electrical network. Mobility in a mechanical domain is analogous to the impedance in an electrical domain. Therefore, in the energy domain the flow variables in the mechanical and electrical domain are velocity and voltage, respectively, while that of the effort variables are force and current, respectively. Those relations can be summarized in Table 2.4.

Table 2.4: Variables in mechanical domain and electrical domain under mobility analogy

Electrical Variable	**Mechanical Variable in Transnational motion**	**Mechanical Variable in Rotational Motion**
Current [A]	Force [N]	Torque [Nm]
Voltage [V]	Velocity [$\frac{\mathrm{m}}{\mathrm{s}}$]	Angular Velocity [$\frac{\mathrm{rad}}{\mathrm{s}}$]
Resistance [Ω]	Responsiveness [$\frac{\mathrm{m}}{\mathrm{Ns}}$]	Rotational Responsiveness [$\frac{\mathrm{rad}}{\mathrm{Nms}}$]
Capacitance [F]	Mass [kg]	Moment of Inertia [$\mathrm{kg} \cdot \mathrm{m}^2$]
Inductance [H]	Compliance [$\frac{\mathrm{m}}{\mathrm{N}}$]	Rotational Compliance [$\frac{\mathrm{rad}}{\mathrm{Nm}}$]
Electrical Impedance [Ω]	Mobility [$\frac{\mathrm{m}}{\mathrm{Ns}}$]	Rotational Mobility [$\frac{\mathrm{rad}}{\mathrm{Nms}}$]

2.5.2 Simulation Programs Based on Mobility Analogy

Figure 2.14 showed an example of the quarter-ship simulation programs. This program simulates the heave response of the ship controlled by the electrical system. The topography of the mechanical system followed the rule of mobility analogy. It told that the inductor $L21$ represents the compression spring, whose magnitude are inverse of each other; a resistor represents a damper, whose magnitude are inverse of each other as well; a capacitor $M21$ represents a quarter mass of the cabin. The description of the components was given in Table 2.5.

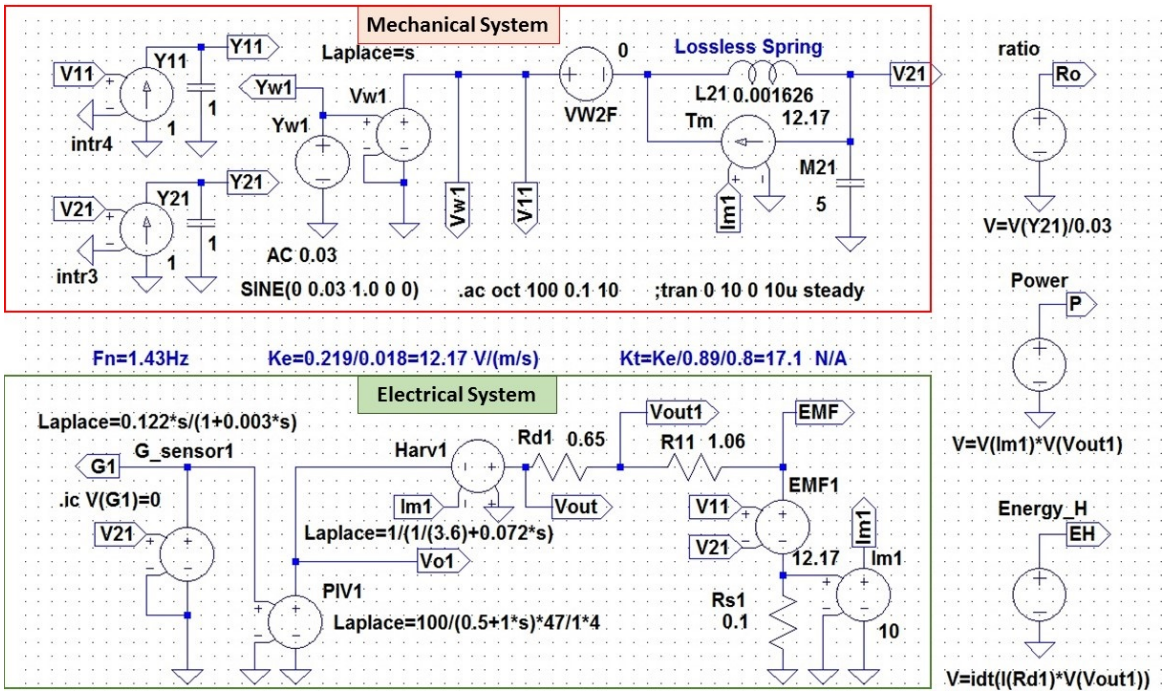

Figure 2.14: One DOF quarter model simulation for a bench test in LTspice®

Table 2.5: Parameters descriptions of the simulation program

Symbol	Units	Description
$V11$	m/s	Velocity of the hulls
$V21$	m/s	Velocity of the cabin
$Y11$	m	Heave of the hulls
$Y21$	m	Heave of the cabin
$L21$	m/N	Inverse value of spring constant
$M21$	kg	a quarter mass of the cabin
$G1$	m/s^2	acceleration of the cabin
$R11$	Ω	Terminal resistance of the M/G
$Rd1$	Ω	Resistance of the wire connecting the control system and the M/G
$Rs1$	Ω	Resistance of the current sensor
Tm	Nm	Mechanical torque
Ke	V/(m/s)	Electromotive force constant
EMF	V	Electromotive force
$Im1$	A	Motor current
Ro	–	Heave ratio of the cabin to the hulls
P	W	Power production of the M/G
EH	J	Energy product of the M/G, positive means harvesting, negative means consumption

- **Skyhook Control Program**
  In the mechanical system, the hulls were given an sinusoidal vertical oscillation at an amplitude of 0.03 m with a range of frequency from 0.1 Hz to 10 Hz as shown in the

program in terms of *.ac oct 100 0.1 10*. The heave response of the cabin was regulated by the torque provided by a M/G, while the current flow through the M/G was controlled by the electrical system. It worked in such a way that the acceleration of the cabin was fed back to the control system, then the I controller corrected the error and outputted a voltage command and applied to the M/G, which consequently modified the current. Known that torque was proportional to the current, therefore the torque acting on the cabin was controlled. To sum up, in this program the mechanical system sent a signal of the velocity of the cabin into the electrical system, the corresponding acceleration and the error were calculated, based on which the electrical system sent back a voltage command to the mechanical system. It repeats until the acceleration of the cabin reaches the set point of the I controller. The transfer function of which is expressed as

$$K_i(s) = 100 \cdot \frac{1}{0.5 + s} \cdot \frac{47}{R_{sky}} \cdot 4 \tag{2.31}$$

in which 100 is the integration gain defined by $C2$ $R2$ and $R1$, as shown in Fig.2.15; the ratio of 47 to a resistor R_{sky} is the impact factor of the I controller; 4 is the gain of a power amplifier. Known that the gain of the G-sensor is 0.122, the total gain of the I controller can be obtained by

$$\boxed{G_i = 0.122 \cdot 100 \cdot 4 \cdot \frac{47}{R_{sky}} = \frac{2294}{R_{sky}}} \tag{2.32}$$

in which the units of the R_{sky} is $\text{k}\Omega$.

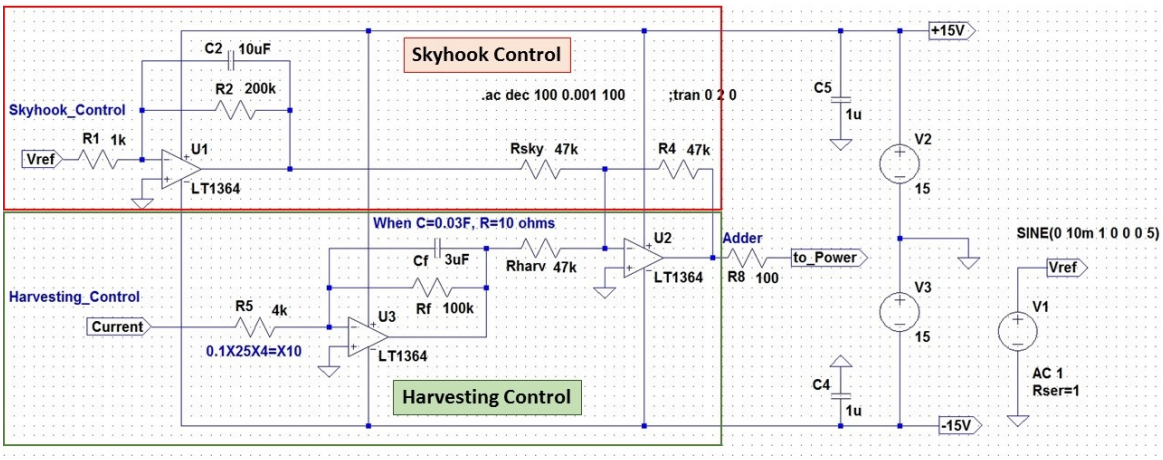

Figure 2.15: Electrical circuit of skyhook control and energy harvesting control in LTspice®

The heave response of the cabin with several I gains were shown in Fig.2.16. In which the oscillation amplitude of the hulls was 0.03 m, the frequency ranked from 0.1 Hz to 10 Hz. An I gain of 0 means the controller was turned off, hence the ship can be seen as a simple mass-spring-mass system, it was named as **free mode**. Others with I controller correcting the motion of the cabin were named as **skyhook mode**. The I gains from the smallest to the largest value were calculated from a group of the tuning resistor R_{sky}: $10^6\,\text{k}\Omega$, $60\,\text{k}\Omega$, $20\,\text{k}\Omega$, $10\,\text{k}\Omega$, $4\,\text{k}\Omega$, $1\,\text{k}\Omega$, respectively.

The y axis of Fig.2.16 represented the heave ratio of the cabin to the hulls. A resonance was observed around 1.44 Hz at free mode, while that under skyhook mode was not significant. In the low frequency domain, the cabin turned to move along with the hulls

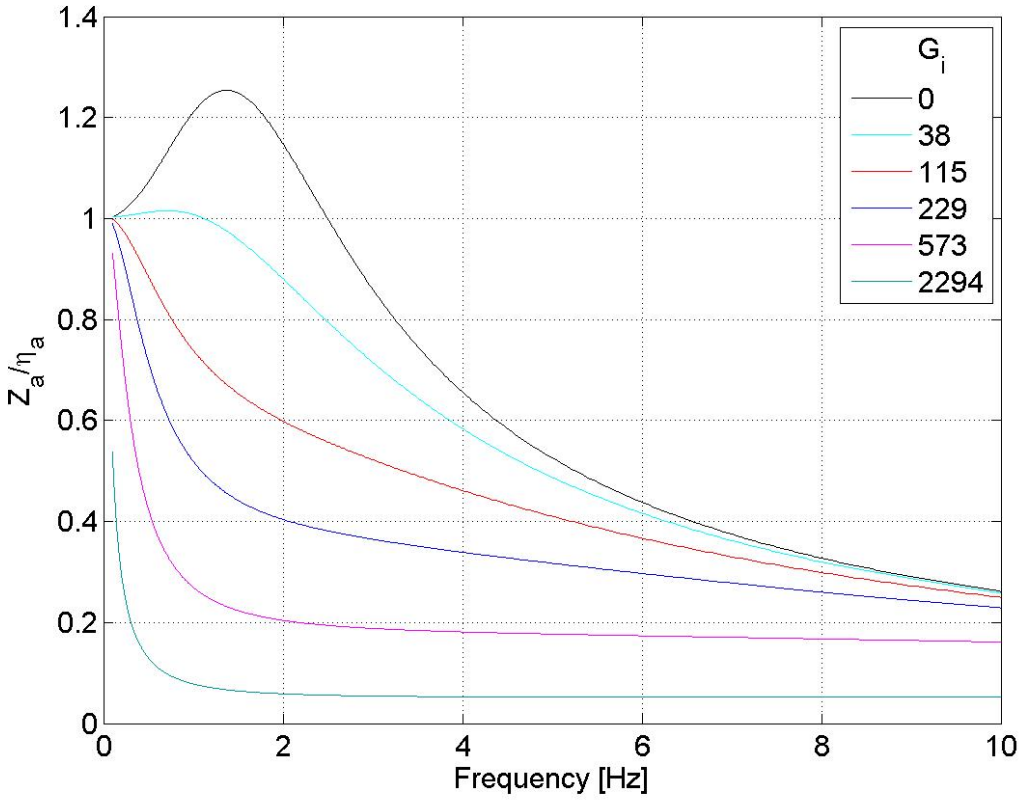

Figure 2.16: Heave response of the cabin obtained under free mode and skyhook mode

since the ratio was pointing to 1. With an increment of the frequency, the heave of the cabin was reduced significantly if the I gain was larger. In a relative higher frequency domain, such gradient was mitigated. It also showed that the resonance can be eliminated greatly if the I gain was larger than 38. In general, higher I gain contributed more in the heave reduction of the cabin at a given frequency.

- **Energy Harvesting Program**
  The transfer function of the energy harvesting mode was given as

$$\boxed{H_{har} = \frac{47}{R_{har}} \cdot \frac{I_{m1}}{\frac{1}{R_L} + sC_p}} \tag{2.33}$$

in which, $\frac{1}{\frac{1}{R_L}+sC_p}$ is the impedance of a RLC parallel circuit. Comparing to Eq.(2.20), it is known that to reach an agreement of the impedance between a simulation program and the electrical circuit, the components of the electrical loads should meet a relation that

$$R_f = 10^4 R_L \tag{2.34}$$
$$C_f = 10^{-4} C_p \tag{2.35}$$

The R_L and C_p represent a pair of load resistor and padding capacitor obtained by a simulation program named MPPs tracking program. $\frac{47}{R_{har}}$ is the impact factor.

- **MPPs Tracking Program**
  An example of the MPPs tracking program was shown in Fig.2.17. In which, the C_p and

Table 2.6: Parameter settings to achieve impedance matching

Frequency (Hz)	C_p(F)	$R_L(\Omega)$	L_p(H)
0.8	0.1100	2.4	10^6
0.9	0.0900	2.9	10^6
1.0	0.0720	3.6	10^6
1.1	0.0560	4.7	10^6
1.2	0.0420	6.8	10^6
1.3	0.0300	10.6	10^6
1.4	0.0205	18.6	10^6

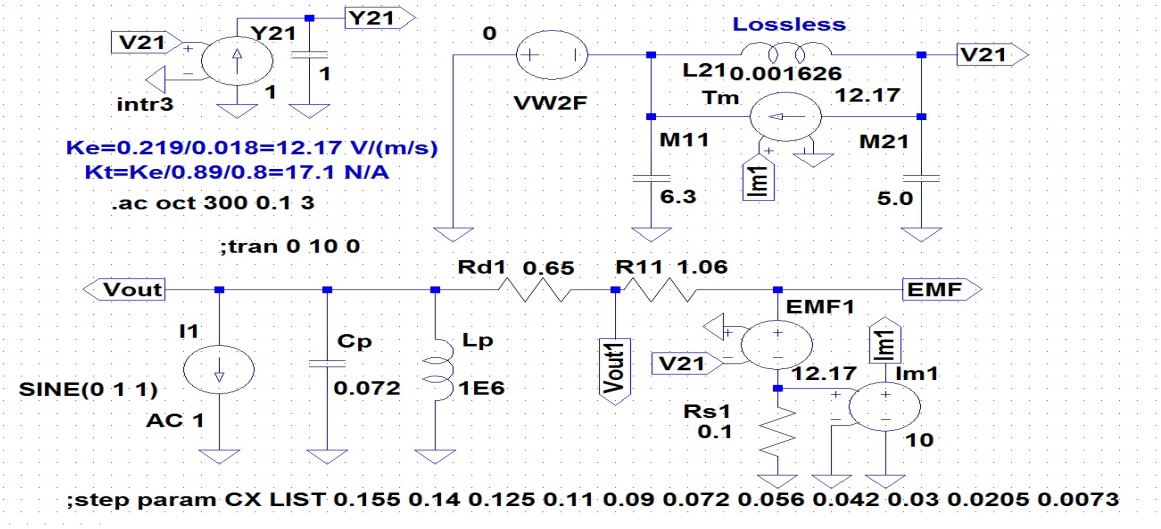

Figure 2.17: Simulation program for tracking maximum power point

L_p were a padding capacitor and padding inductor. Sinusoidal current with amplitude of 1 A and frequency varies from 0.1 Hz to 3.0 Hz was fed into the motor. The purpose of tuning the C_p and L_p is to seek the magnitude of a load resistor R_L, with which the impedance matching of the source term and the load term can be obtained, as a results heave resonance of the cabin can be observed.

A group of the typical results was given in Fig.2.18. The x axis represented the oscillation frequency, while y axis meaned the heave of the cabin, input power of the M/G and the corresponding magnitude of the load resistor, respectively. Each curve was labeled with a frequency value, which means that a peak of the curve was supposed to be observed at that frequency. Hereby, the magnitude of the C_p, L_p and R_L were regarded as the MPP at that frequency. Details of the MPPs were given in Table 2.6. Note that the inductance was extremely large, the amount of current crossed through it can be ignored, therefore the inductor was omitted in the transfer function as expressed in Eq.(2.33) and was not adopted in the model test.

What need to be pointed out is that the programs shown in Fig.2.14 and Fig.2.18 were built in ideal condition, in which the non-linear friction of the suspension components was not taken into consideration. It implied that the programs can only provide a quantitative evaluation of the control system. To make an application of those programs for a model test, the friction should be modeled precisely.

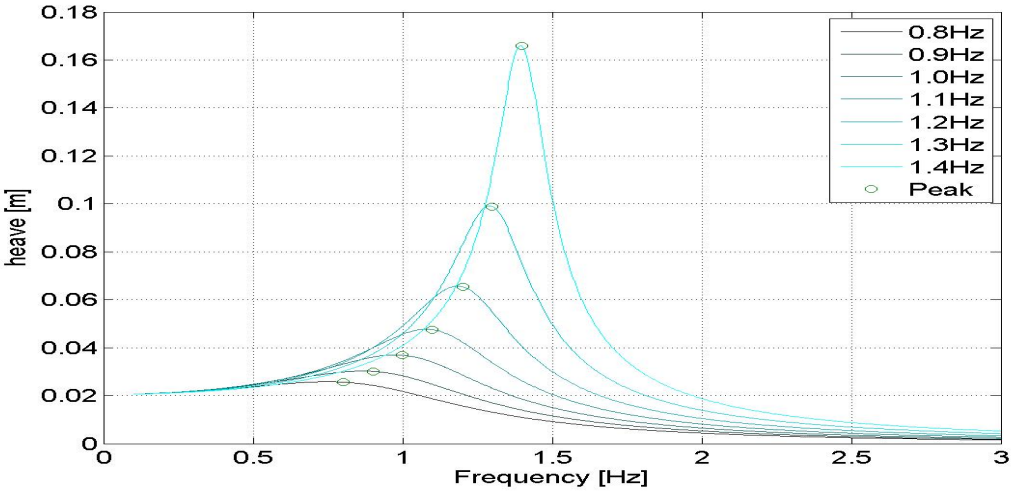

(a) Heave of the cabin

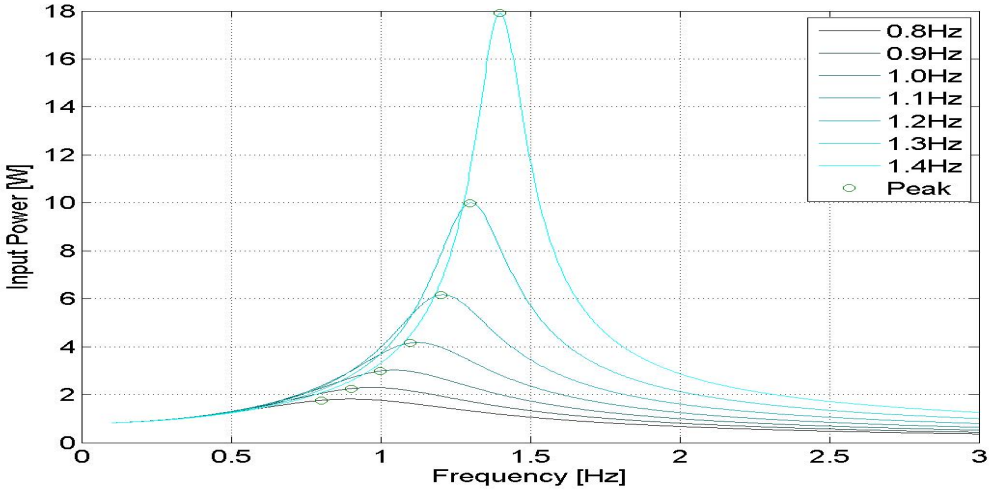

(b) Input Power

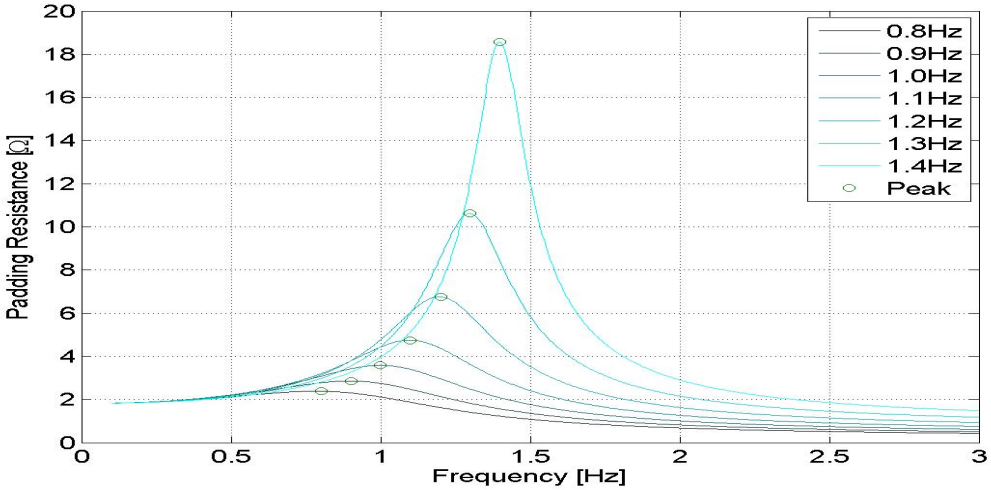

(c) Padding resistance

Figure 2.18: Heave of the cabin, power production and magnitude of padding resistance under MPP tracking

2.6 Equations of Motion

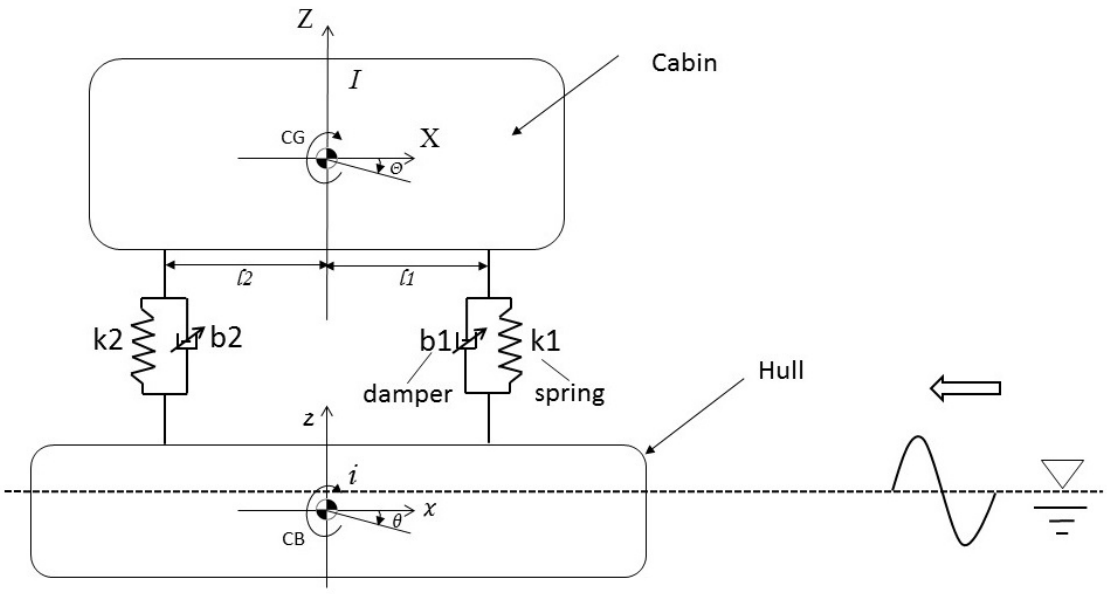

Figure 2.19: Dynamic Model

The dynamic model of WHzer-6 was depicted in Fig.2.19. The coordinate system followed the right-hand rule. The pitch motion of the cabin was around its center of gravity, while that of the hulls was around its center of buoyancy. A positive pitch motion was regarded as bow down, that of heave was upward. The descriptions of the physical characteristics were given in Table.2.7.

The motion of the cabin and the hulls interacted with each other through the compression springs mounted in between, as well as the M/G effect produced by the controllers. Assuming the M/G effect, either motor effect or generator effect, can be represented by a damper with time-depending damping efficient of b_1 and b_2 for the front part and the rear part, respectively. The equations of motion can be expressed as
Heave of the Cabin:

$$M \cdot \ddot{Z} + b_1 \cdot \dot{Z}_{r1} + k_1 \cdot Z_{r1} + b_2 \cdot \dot{Z}_{r2} + k_2 \cdot Z_{r2} = 0 \tag{2.36}$$

Pitch of the Cabin:

$$I \cdot \ddot{\Theta} + l_1 b_1 \cdot \dot{Z}_{r1} + l_1 k_1 \cdot Z_{r1} - l_2 b_2 \cdot \dot{Z}_{r2} - l_2 k_2 \cdot Z_{r2} = 0 \tag{2.37}$$

Heave of the Hulls:

$$\begin{aligned} &m \cdot \ddot{z} - (b_1 \cdot \dot{Z}_{r1} + k_1 \cdot Z_{r1} + b_2 \cdot \dot{Z}_{r2} + k_2 \cdot Z_{r2}) \\ &= E_3 - a_{33}\ddot{z} - b_{33}\dot{z} - k_{33}z - a_{35}\ddot{\theta} - b_{35}\dot{\theta} - k_{35}\theta \end{aligned} \tag{2.38}$$

Pitch of the Hulls:

$$\begin{aligned} &i \cdot \ddot{\theta} - (l_1 b_1 \cdot \dot{Z}_{r1} + l_1 k_1 \cdot Z_{r1} - l_2 b_2 \cdot \dot{Z}_{r2} - l_2 k_2 \cdot Z_{r2}) \\ &= E_5 - a_{55}\ddot{\theta} - b_{55}\dot{\theta} - k_{55}\theta - a_{53}\ddot{z} - b_{53}\dot{z} - k_{53}z \end{aligned} \tag{2.39}$$

in which, Z_{r1} and Z_{r2} represent the relative displacement of the front and rear compression springs, respectively, which are expressed as

$$Z_{r1} = Z - l_1\Theta - z + l_1\theta \tag{2.40}$$

$$Z_{r2} = Z + l_2\Theta - z - l_2\theta \tag{2.41}$$

Assuming the time component is expressed as $e^{j\omega t}$, then the motions and their derivatives can be written as:

$$\begin{bmatrix}\dot{Z} & \dot{\Theta} & \dot{z} & \dot{\theta}\end{bmatrix}^T = j\omega \cdot \begin{bmatrix}Z & \Theta & z & \theta\end{bmatrix}^T \tag{2.42}$$

$$\begin{bmatrix}\ddot{Z} & \ddot{\Theta} & \ddot{z} & \ddot{\theta}\end{bmatrix}^T = -\omega^2 \cdot \begin{bmatrix}Z & \Theta & z & \theta\end{bmatrix}^T \tag{2.43}$$

$$Z_{r1} = \begin{bmatrix}1 & -l_1 & -1 & l_1\end{bmatrix} \cdot \begin{bmatrix}Z & \Theta & z & \theta\end{bmatrix}^T \tag{2.44}$$

$$Z_{r2} = \begin{bmatrix}1 & l_2 & -1 & -l_2\end{bmatrix} \cdot \begin{bmatrix}Z & \Theta & z & \theta\end{bmatrix}^T \tag{2.45}$$

$$\dot{Z}_{r1} = j\omega \cdot \begin{bmatrix}1 & -l_1 & -1 & l_1\end{bmatrix} \cdot \begin{bmatrix}Z & \Theta & z & \theta\end{bmatrix}^T \tag{2.46}$$

$$\dot{Z}_{r2} = j\omega \cdot \begin{bmatrix}1 & l_2 & -1 & -l_2\end{bmatrix} \cdot \begin{bmatrix}Z & \Theta & z & \theta\end{bmatrix}^T \tag{2.47}$$

Substitute Eq.(2.42)-(2.47) into Eq.(2.36)-(2.39), and after several algebra, it gives:
Heave of Cabin:

$$\begin{bmatrix} -\omega^2 \cdot M + (k_1 + j\omega b_1) + (k_2 + j\omega b_2) \\ -l_1(k_1 + j\omega b_1) + l_2(k_2 + j\omega b_2) \\ -(k_1 + j\omega b_1) - (k_2 + j\omega b_2) \\ l_1(k_1 + j\omega b_1) - l_2(k_2 + j\omega b_2) \end{bmatrix}^T \cdot \begin{bmatrix} Z \\ \Theta \\ z \\ \theta \end{bmatrix} = 0 \tag{2.48}$$

Pitch of Cabin:

$$\begin{bmatrix} l_1(k_1 + j\omega b_1) - l_2(k_2 + j\omega b_2) \\ -\omega^2 \cdot I - l_1^2(k_1 + j\omega b_1) - l_2^2(k_2 + j\omega b_2) \\ -l_1(k_1 + j\omega b_1) + l_2(k_2 + j\omega b_2) \\ l_1^2(k_1 + j\omega b_1) + l_2^2(k_2 + j\omega b_2) \end{bmatrix}^T \cdot \begin{bmatrix} Z \\ \Theta \\ z \\ \theta \end{bmatrix} = 0 \tag{2.49}$$

Heave of Hulls:

$$\begin{bmatrix} -(k_1 + j\omega b_1) - (k_2 + j\omega b_2) \\ l_1(k_1 + j\omega b_1) - l_2(k_2 + j\omega b_2) \\ -\omega^2(m + a_{33}) + j\omega b_{33} + k_{33} + (k_1 + j\omega b_1) + (k_2 + j\omega b_2) \\ -\omega^2 a_{35} + j\omega b_{35} + k_{35} - l_1(k_1 + j\omega b_1) + l_2(k_2 + j\omega b_2) \end{bmatrix}^T \cdot \begin{bmatrix} Z \\ \Theta \\ z \\ \theta \end{bmatrix} = E_3 \tag{2.50}$$

Pitch of Hulls:

$$\begin{bmatrix} -l_1(k_1 + j\omega b_1) + l_2(k_2 + j\omega b_2) \\ l_1^2(k_1 + j\omega b_1) + l_2^2(k_2 + j\omega b_2) \\ -\omega^2 a_{53} + j\omega b_{53} + k_{53} + l_1(k_1 + j\omega b_1) - l_2(k_2 + j\omega b_2) \\ -\omega^2(i + a_{55}) + j\omega b_{55} + k_{55} - l_1^2(k_1 + j\omega b_1) - l_2^2(k_2 + j\omega b_2) \end{bmatrix}^T \cdot \begin{bmatrix} Z \\ \Theta \\ z \\ \theta \end{bmatrix} = E_5 \tag{2.51}$$

The equation matrix of the motions, therefore, can be written as

$$A \cdot \begin{bmatrix} Z \\ \Theta \\ z \\ \theta \end{bmatrix} = \begin{bmatrix} 0 \\ 0 \\ E_3 \\ E_5 \end{bmatrix} \tag{2.52}$$

in which A is a 4×4 matrix, the row of which is comprised of the first component of the left-hand equation from Eq.(2.48) to Eq.(2.51), respectively. Once the b_1 and b_2 are known, the motion of the cabin and the hulls can be estimated by

$$\begin{bmatrix} Z \\ \Theta \\ z \\ \theta \end{bmatrix} = A^{-1} \cdot \begin{bmatrix} 0 \\ 0 \\ E_3 \\ E_5 \end{bmatrix} \tag{2.53}$$

where A^{-1} is the inverse of A.

The results of the equations of motion at the free mode and the rigid mode were given in Appendix A.

Table 2.7: Specifications of the parameters in the equations of motion

Symbol	Value	Unit	Description
M	34.68	kg	Modified mass of the upper part of the ship (includes the mass of a load shaft)
m	13.1	kg	Modified mass of the lower part of the ship
I	3.216	kgm^2	Moment of inertia of the cabin
i	2.305	kgm^2	Moment of inertia of the hulls
l_1	0.36	m	Horizontal distance from the front suspension to CG
l_2	0.36	m	Horizontal distance from the rear suspension to CG
k_1	1230	N/m	Spring constant of two compression springs at the front
k_2	1230	N/m	Spring constant of two compression springs at the rear
k_{33}	5239	N/m	Restoring force constant of heave for two hulls
k_{53}	-97.51	N	Restoring moment on pitch due to heave for two hulls
k_{35}	-97.51	N	Restoring force on heave due to pitch for two hulls
k_{55}	894.04	Nm	Restoring moment constant of pitch for two hulls
b_1	$b1(t)$	$\mathrm{Nm/s}^2$	Time-dependent damping coefficient at the front
b_2	$b2(t)$	$\mathrm{Nm/s}^2$	Time-dependent damping coefficient at the rear
Z	$Z(t)$	m	Heave of the cabin
Θ	$\Theta(t)$	rad	Pitch of the cabin
z	$z(t)$	m	Heave of the hulls
θ	$\theta(t)$	rad	Pitch of the hulls
a_{ij}	$a_{ij}(\omega)$	kg	Frequency-dependent added mass for the force on the hulls in the i direction due to the acceleration of the hulls in the j-motion
b_{ij}	$b_{ij}(\omega)$	Ns/m	Frequency-dependent damping coefficient for the force on the hulls in the i direction due to the velocity of the hulls in the j-motion
E_3	$E_3(\omega)$	N	Frequency-dependent wave exciting force
E_5	$E_5(\omega)$	N	Frequency-dependent wave exciting moment
j	–	–	Imaginary unit
ω	–	rad/s	Angular frequency

Chapter 3

Bench Tests and Evaluation

This chapter introduces three bench tests of WHzer-6. A free decay test of the cabin was carried out to identify the natural frequency of the cabin, and to estimate the friction of the suspensions; a motor driven test was implemented to investigate the movability of the cabin at a certain applied voltage to the M/Gs, and to estimate the dead zone of the suspensions; a forced oscillation test of the hulls was used to validate the performance of the control system.

3.1 Free Decay Test of the Cabin

3.1.1 General Description

A free decay test of a ship is normally implemented in still water. However, in this section, the test was operated on the suspended cabin while the hulls were settled on a fixed platform. The objectives of this test are to identify the natural frequency of the suspended cabin, and to estimate the friction of the suspension components.

Known that the force of friction commonly consists of a static component and a viscous component. The static friction occurs before a relative motion between two objects happens, while that of the viscous friction occurs after and it is proportional to the velocity. For an oscillation motion, the friction is known as non-linear.

In free decay test, the friction causes the oscillation motion eventually die out, during which the kinetic energy is converted into thermal energy or heat. Here, it is assumed that this procedure can be analogously regarded as a viscous damper dissipating energy in an ideal system, whose damping coefficient varies along with the oscillation velocity so as to keep the damping force equals to the force of friction. This relation can be expressed as

$$F_{df} = b(\dot{Z}) \cdot \dot{Z} = F_{cf} \tag{3.1}$$

in which F_{df} and F_{cf} represents the damping force and the friction, respectively; $b(t)$ represents the equivalent damping coefficient which is a function of the velocity $\dot{Z}$.

The governing equation of the heave motion of the cabin in a free decay test can be written as:

$$M \cdot \ddot{Z} + b \cdot \dot{Z} + k \cdot Z = 0 \tag{3.2}$$

in which M and k represent the mass of the cabin and the spring constant of the compression springs, respectively.

It can also be written as

$$\ddot{Z} + \frac{b}{M} \cdot \dot{Z} + \frac{k}{M} \cdot Z = 0 \tag{3.3}$$

A non-dimensional damping coefficient K is defined as a fraction between the actual damping coefficient and the critical damping coefficient [34], which is given as

$$K = \frac{b}{2 \cdot \sqrt{M \cdot k}} \tag{3.4}$$

Known that the natural frequency of the cabin can be expressed as

$$\omega_0 = \sqrt{\frac{k}{M}} \tag{3.5}$$

After some algebra of Eq.(3.4) and Eq.(3.5), the actual damping coefficient b can be written as

$$\boxed{b = \frac{2 \cdot K \cdot k}{\omega_0}} \tag{3.6}$$

in which, the compression spring constant k is known; the natural frequency ω_0 and K can be estimated from a free decay test.

Substituting Eq.(3.6) into Eq.(3.3), after some algebra one can obtain that:

$$\ddot{Z} + 2K\omega_0 \cdot \dot{Z} + \omega_0^2 \cdot Z = 0 \tag{3.7}$$

With an initial vertical displacement of Z_a of the cabin in the test, the solution of the above equation can be given as

$$Z = Z_a \cdot e^{-K\omega_0 t} \left(cos\omega_z t + \frac{K\omega_0}{\omega_z} sin\omega_z t \right) \tag{3.8}$$

in which, ω_z represents the decay frequency of two successive peaks, $e^{-K\omega_0 t}$ represents the corresponding decrease of two successive peaks, which is expressed as

$$ln \left[\frac{Z(t + T_z)}{Z(t)} \right] = -K\omega_0 T_z \tag{3.9}$$

By using the decay frequency ω_z to approximately represent the natural frequency ω_0, the K factor estimated by a free decay history of the cabin can be rewritten as:

$$\boxed{K = \frac{1}{2\pi} \cdot ln \left[\frac{Z(t)}{Z(t + T_z)} \right]} \tag{3.10}$$

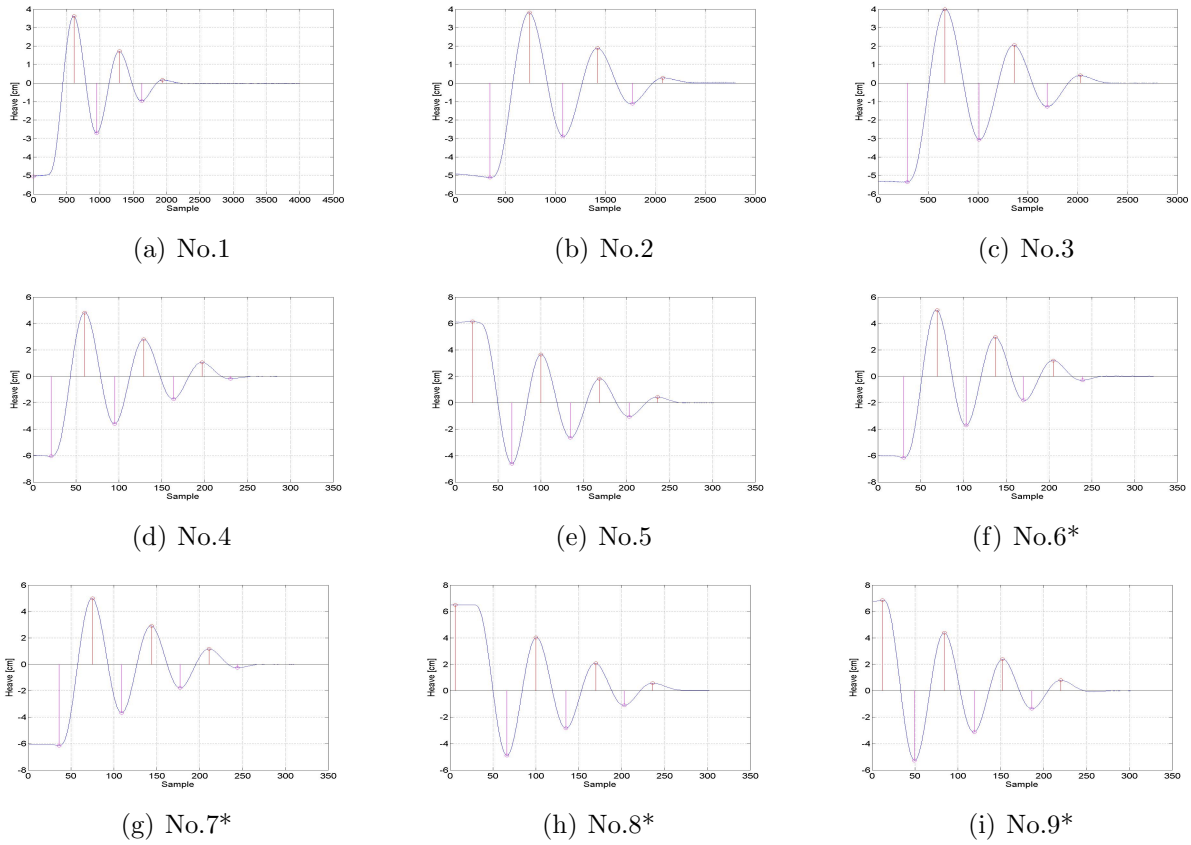

(a) No.1 (b) No.2 (c) No.3

(d) No.4 (e) No.5 (f) No.6*

(g) No.7* (h) No.8* (i) No.9*

Figure 3.1: Free decay test of the cabin with the motors connecting the pinion gears

3.1.2 Free Decay Tests and Natural Frequency

In the free decay test, the control system was turned off and disconnected from the terminals of the M/Gs, so as to avoid current flow through the M/Gs while they were rotated.

The cabin was initially lifted up or pushed down to a certain level and then released. A vertical oscillation of the cabin was observed, which continued several periods before died out. To reduce the measurement error, this test was repeated 9 times with the M/Gs connected to the shaft of a pinion and 4 times with the two disconnected. The decay histories of each oscillation of the cabin were given in Fig.3.1 and Fig.3.2. A negative initial value of the curve in a sub-figure means the cabin was pushed down, that of positive means lifted up before releasing.

Fig.3.1(a) to Fig.3.1(e) represented the cases in which lubrication oil was not instantly added to the pinion gears, while that from Fig.3.1(f) to 3.1(i) was added (with a $*$ mark). The sampling frequency for the first row of Fig.3.1 was 1000 Hz with an initial stoke of 0.04 m, which for the second and third rows were 100 Hz and $0.05 \sim 0.06$ m, respectively.

In the decay history from Fig.3.1(a) to Fig.3.1(c), 3 peaks and 2 troughs were observed, that in Fig.3.1(d), Fig.3.1(f) and Fig.3.1(g) were 3 peaks and 3 troughs. By comparing Fig.3.1(f) to Fig.3.1(d) one can find that the effect of the lubrication oil was negligible. Because under the same initial stroke condition of 0.05 m, the decay history of the oscillation and the number of peaks and toughs were extremely alike. After disconnecting the M/Gs from the pinion's shafts, about 10 peaks and 10 troughs were observed in each sub-figure of Fig.3.2, whose initial stroke equaled to that of the cases shown from Fig.3.1(d) to 3.1(i).

The natural period was estimated by calculating a time interval between two successive peaks. If the oscillation decays slow, several estimations can be obtained from a single test.

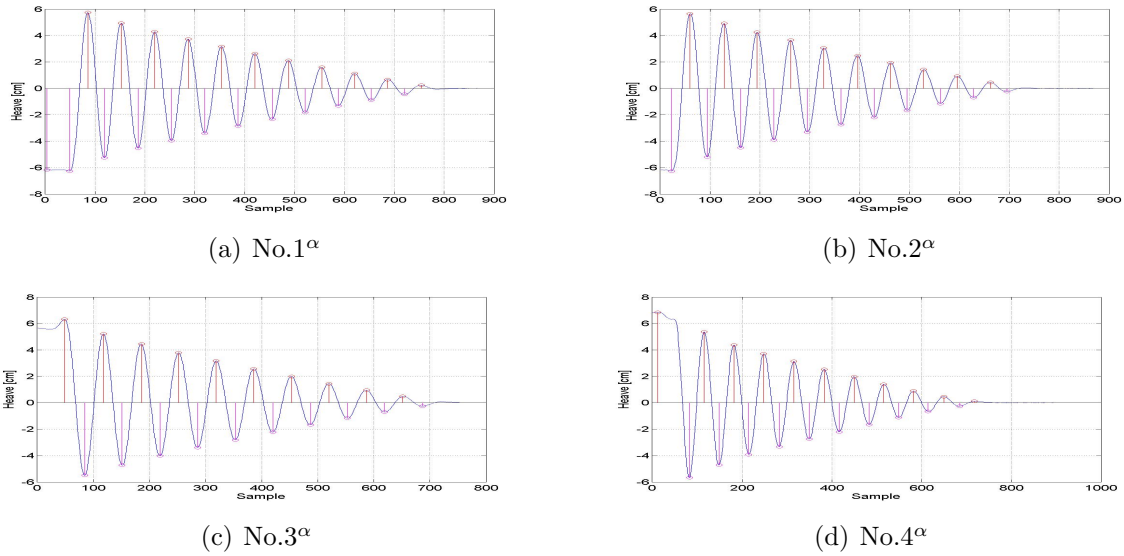

(a) No.1$^{\alpha}$ (b) No.2$^{\alpha}$

(c) No.3$^{\alpha}$ (d) No.4$^{\alpha}$

Figure 3.2: Free decay test of the cabin with the motors disconnected from the pinion gears

Table 3.1: Natural periods estimated from free decay test

Case	**1**	**2**	**3**	**4**	**5**	6*	7*	8*	9*	1^{α}	2^{α}	3^{α}	4^{α}
T_0	0.68	0.69	0.69	0.70	0.72	0.70	0.69	0.70	0.69	0.67	0.67	0.67	0.67
ω_0	9.20	9.10	9.10	9.02	8.73	9.02	9.06	9.02	9.06	9.36	9.35	9.36	9.40

Therefore, in a single test, the natural period was obtained by taking the mean value of the estimated natural periods from the peaks, it is given as

$$\overline{T_0} = \frac{1}{n-1}\sum_{i=2}^{n}(t_i - t_{i-1}) \tag{3.11}$$

in which n represents the number of peaks, t_i represent the time when the i-th peak was observed. The natural periods estimated in each run of the test were listed in Table 3.1. The case number with a superscript of α represented the one had the M/Gs disconnected from the pinion gears.

It was seen that the estimated natural frequency varied slightly among the tests, the mean value of the 9 cases with the M/Gs connected to the shafts of the pinion gears gives:

$$T_0 \approx 0.70 \tag{3.12}$$
$$f_0 \approx 1.44 \tag{3.13}$$
$$\omega_0 \approx 9.03 \tag{3.14}$$

While that had the M/Gs disconnected to the pinion gears gives:

$${T_0}^{\alpha} \approx 0.67 \tag{3.15}$$
$${f_0}^{\alpha} \approx 1.49 \tag{3.16}$$
$${\omega_0}^{\alpha} \approx 9.38 \tag{3.17}$$

It showed that equipping with the M/Gs extended the natural frequency of the suspended cabin with a ratio of 4.5%, which also had relatively larger damping coefficient.

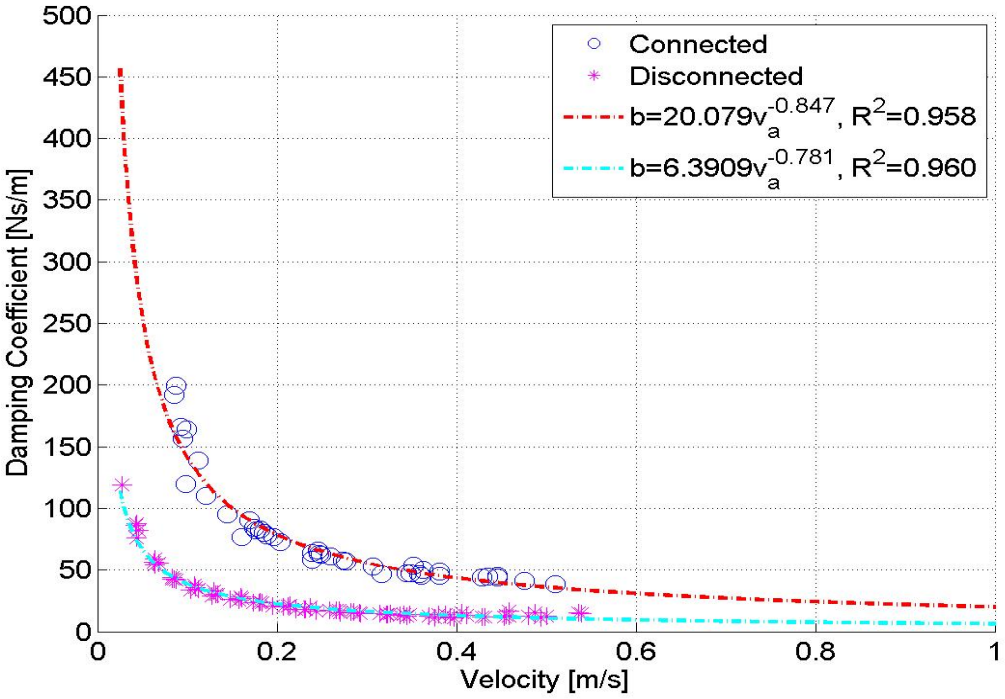

Figure 3.3: Estimated damping coefficient of the suspensions versus heave velocity of the cabin

3.1.3 Equivalent Viscous Damping for Coulomb Friction

A method of modeling the friction was proposed by using the actual damping estimated in the free decay test. Known that the value of K can be calculated from a pair of successive peaks in a free decay history through Eq.(3.10). Its corresponding mean oscillation amplitude of the cabin, also known as heave, can be represented by

$$Z_a = \frac{Z(t) + Z(t + T_z)}{2} \tag{3.18}$$

Then the oscillation velocity can be written as

$$v_a = \omega_a \cdot Z_a \tag{3.19}$$

Substituting K into Eq.(3.6) the actual damping coefficient for a given v_a was obtained. A figure of the actual damping coefficients b versus the mean oscillation velocity v_a was showed in Fig.3.3. A non-linear relation between the oscillation velocity of the cabin and the damping coefficient was observed. A power curve fit was carried out, which gives

$$\boxed{b = 20.079 \cdot v_a^{-0.847}}, \qquad for v_a \in (0.085, 0.510) \tag{3.20}$$

$$b^{\alpha} = 6.3909 \cdot v_a^{-0.781}, \qquad for v_a \in (0.027, 0.539) \tag{3.21}$$

The coefficient of determination, denoted as R^2, for both fittings are about 0.96. It implied that a reasonable prediction of the damping coefficient can be made for a given velocity that in the range given in the above equations. An extension of the prediction was also shown in Fig.3.3. It showed that at low velocity, the damping coefficient is relatively large, while at high velocity it turns to maintain at a small constant value.

3.2 Motor Driven Test

3.2.1 General Description and Evaluation

Two types of voltage signal were applied to the M/Gs which drive the M/Gs rotating accordingly. The objectives were to investigate the movability of the cabin at a given applied voltage of the M/Gs, and to estimate the dead zone of the suspensions.

One of the tests was implemented by applying a periodic voltage to the terminals of the four M/Gs simultaneously, which generated a periodic rotation of the M/Gs, consequently yielded a vertical oscillation of the cabin through the rack-pinion units. The oscillation amplitude of the cabin was observed and recorded.

The other test applied a constant voltage at a time to the M/Gs, which was held for a while before the next adjustment of the input voltage. The corresponding heave response of the cabin was observed. The voltage adjustment was done in two ways, whose initial applied voltage were both 0 V. One was done by increasing the voltage from 0 V to 4 V then decreasing back to 0 V; the other was decreased to -4 V at first, and then increased to 0 V. The step at a time was 1 V. As a result, the cabin was lifted up or pushed down at a certain distance according to the voltage applied to the M/Gs.

Results of the test under the periodic voltage input condition and the stepped voltage input were given in Fig.3.4 and Fig.3.5, respectively. Simple linear regression were carried out on the results. By doing which, the relation between the applied voltage of the M/Gs and the output of the cabin's heave motion was estimated.

Figure 3.4 suggested that the heave amplitude of the cabin was positively related to the input voltage of the M/Gs. According to a linear regression, the relation can be expressed as:

$$Z_a = -1.2583 + 1.2247 \cdot V_{peri-in}, \qquad r^2 = 0.9994 \tag{3.22}$$

in which $V_{peri-in}$ represents the periodic input voltage, r^2 is the ratio of the explained variation to the total variation. The closer it to 1, the better it fits the data. This equation implied that an unit variance of the periodic voltage could cause a displacement of the cabin about 1.2247 cm, which can be written as

$$\boxed{1V_{peri-in} = 1.22\,\text{cm}} \tag{3.23}$$

Known that the initial value of $V_{peri-in}$ and Z were both 0, the value of -1.2583, therefore, can be regarded as a thrust value of the dead zone. It means until the input voltage exceeds a certain value of V_{sv}, would not the cabin oscillate. It can be obtained by letting $Z = 0$ in Eq.(3.22), which yields

$$V_{sv} = 1.03 \tag{3.24}$$

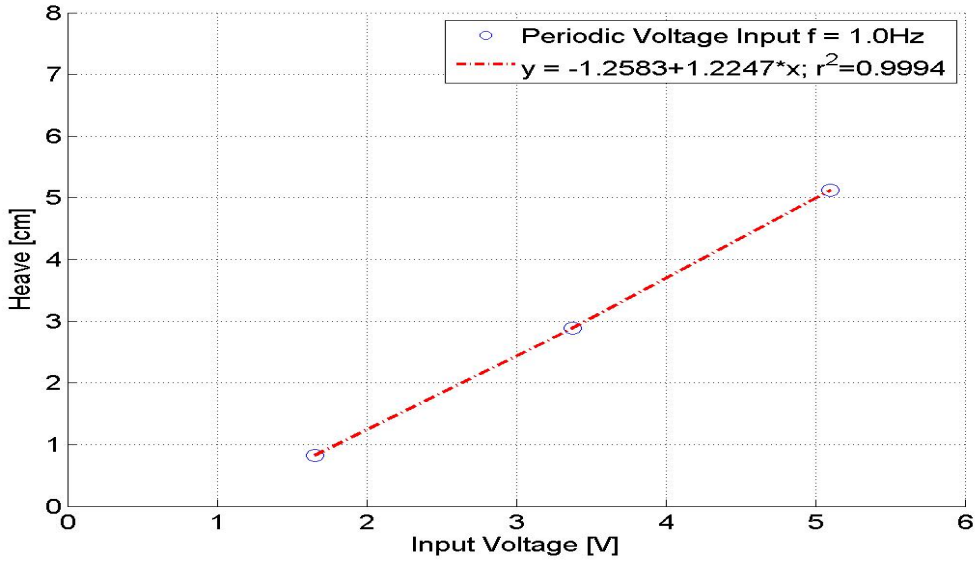

Figure 3.4: Estimated relation between heave of the cabin and the periodic voltage input of the M/Gs, $f = 1.0\,\mathrm{Hz}$

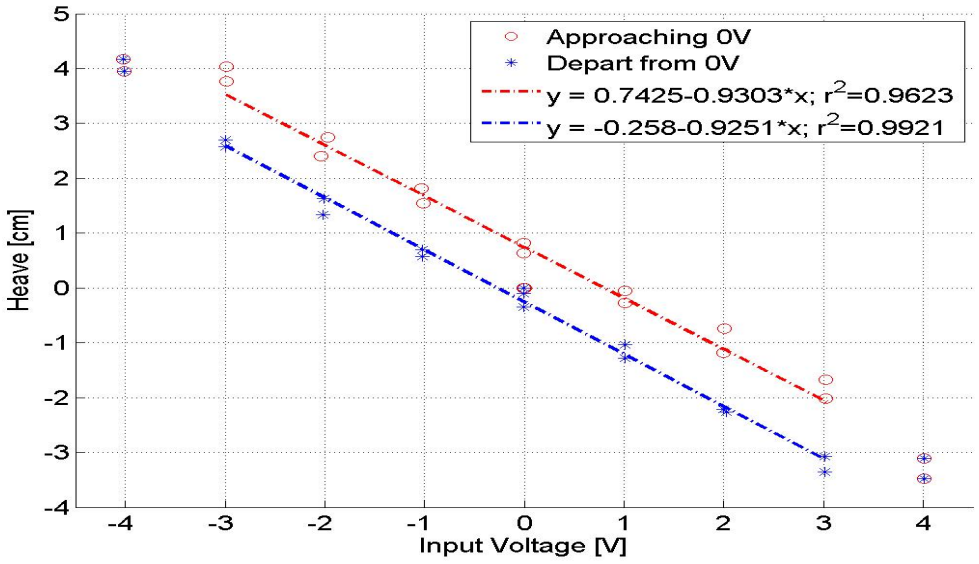

Figure 3.5: Estimated relation between heave of the cabin and the stepped voltage input of the M/Gs

Figure 3.5 showed the results obtained by varying the input voltage with 1 V at a time. The test was repeated four times, in which two times were started from decreasing and the other two from increasing of the input voltage. Those results were classified by the movement direction of the cabin as shown in the figure. The blue color represents the cabin was departing from its natural position, while that of the red represents approaching. It was readily seen that the cabin did not back to its natural position when the input voltage was tuned back to 0 V. A simple linear regression was carried out to identify the relation between the input voltage and the output motion, which showed

$$Z_a = -0.258 - 0.9251 \cdot V_{step-in}, \qquad r^2 = 0.9921 \tag{3.25}$$

$$Z_a = 0.7425 - 0.9303 \cdot V_{step-in}, \qquad r^2 = 0.9623 \tag{3.26}$$

Those equations implied that an unit variance of the input voltage could produce heave motion of the cabin of 0.93 cm approximately, which was expressed as

$$\boxed{1V_{step-in} = 0.93\,\text{cm}} \tag{3.27}$$

Also note that the difference between the constant values of Eq.(3.25) and Eq.(3.26)can be regarded as a representation of the dead zone of the suspension components, which gave

$$\boxed{Z_{dz} = 1.0\,\text{cm}} \tag{3.28}$$

There is another way to estimate the dead zone by using Eq.(3.24), which implied that to start a motion of the cabin the applied voltage should reach at least 1.03 V, by substituting it into Eq.(3.27), one can obtain a result of 0.96 cm. It is extremely close to the one in Eq.(3.28). By using which, the energy consumed to break the dead zone may be estimated by

$$E_{dz} = M \cdot g \cdot Z_{dz} \tag{3.29}$$

in which g is the acceleration of gravity. Substituting Eq.(3.28) into Eq.(3.29) gave

$$\boxed{E_{dz} = 3.4\,\text{Nm}} \tag{3.30}$$

3.2.2 Energy Balance

In a periodic voltage input test, the input energy per period can be obtained in such a way that, firstly take an integration of the product of the applied voltage of the M/Gs and the current over n periods, then take the mean value of it over period. It can be expressed as

$$E_{in} = \frac{1}{n}\int_0^{nT} V_{in}(t) \cdot I(t)dt \tag{3.31}$$

in which, V_{in} represents the applied voltage to the M/Gs, $I(t)$ represents the motor current.

Assuming the input energy was distributed into four sections, part of which was converted into kinetic energy, dissipated by the coulomb friction, consumed by the winding resistance of the M/Gs, and a residual component.

The kinetic energy can be obtained by

$$E_{kn} = \frac{1}{2} \cdot M \cdot (\omega \cdot Z_a)^2 \tag{3.32}$$

The energy dissipated by the friction was seen as the amount consumed by an equivalent viscous damper, whose damping coefficient was given in Eq.(3.20). Known that the worked done per period by a damper can be estimated by

$$E_{df} = \frac{1}{n}\int_0^{nT} b \cdot \dot{Z}(t)dZ(t) \tag{3.33}$$

in which $Z(t)$ is a harmonic motion with a frequency of ω and amplitude of Z_a. After some algebra, one can get

$$E_{df} = \pi \cdot b \cdot \omega \cdot {Z_a}^2 \tag{3.34}$$

The energy lost per period due to the resistance of the leading cable R_{cr}, can be obtained by

$$E_{cr} = \frac{1}{n}\int_0^{nT} R_{cr} \cdot I^2(t)dt \tag{3.35}$$

The residual energy was defined as the amount of energy that was lost in the ways that were not mentioned above. The energy balance of the motor driven test, hereby, can be described as

$$\boxed{E_{in} = E_{kn} + E_{df} + E_{cr} + E_{rs}} \tag{3.36}$$

The energy distribution at each section was listed in Table 3.2, the corresponding pie chart was depicted in Fig.3.6. It showed that about 30% of the input energy was dissipated by friction, that of $6 \sim 25\%$ was consumed by the leading cable resistance, whereas the useful energy was below $4 \sim 18\%$ of the total input energy. With an increment of the input voltage, more energy was distributed to the kinetic form.

Table 3.2: Energy distribution of the periodic motor driven test, $f = 1.0\,\mathrm{Hz}$

$Z_a(\,\mathrm{cm})$	$V_{in}(\,\mathrm{V})$	$E_{in}(\,\mathrm{Nm})$	$E_{kn}(\,\mathrm{Nm})$	$E_{df}(\,\mathrm{Nm})$	$E_{rw}(\,\mathrm{Nm})$	$E_{rs}(\,\mathrm{Nm})$
0.83	1.65	1.12	0.05	0.33	0.18	0.57
2.88	3.38	4.59	0.57	1.40	0.90	1.72
5.12	5.10	10.04	1.80	2.71	2.48	3.05

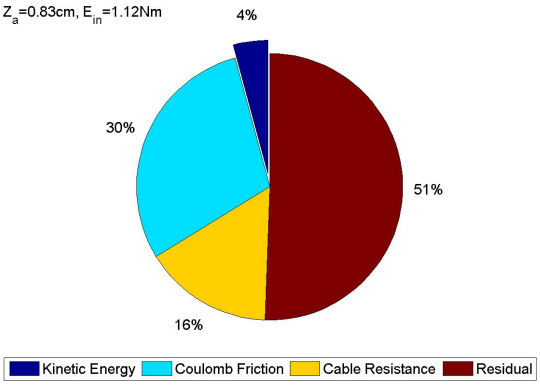

(a) $Z_a = 0.83\,\mathrm{cm}, f = 1.0\,\mathrm{Hz}$

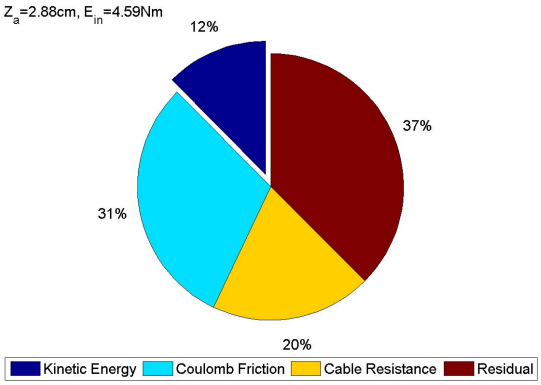

(b) $Z_a = 2.88\,\mathrm{cm}, f = 1.0\,\mathrm{Hz}$

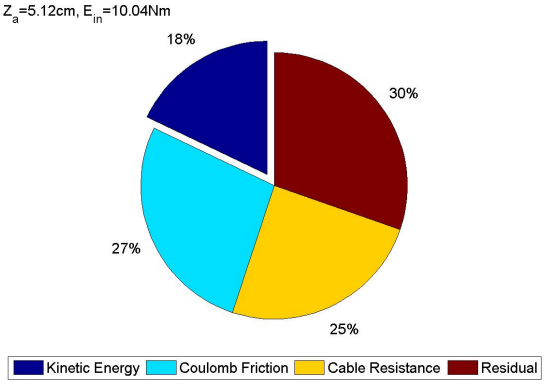

(c) $Z_a = 5.12\,\mathrm{cm}, f = 1.0\,\mathrm{Hz}$

Figure 3.6: Energy distribution in the periodic motor driven test, $f = 1.0\,\mathrm{Hz}$

3.3 Forced Oscillation Test of the Hulls

3.3.1 General Description

The objectives of the on land forced oscillation test of the hulls were to validate the performance of the control design, and to experimentally confirm a feasible region of the parameter settings for the skyhook control scenario.

The test setup was shown in Fig.3.7. An oscillation machine was settled on a heavy steel framework. The oscillation operator was connected to a metal support on which the model ship was ridden. The hulls were tied to the bottom of the metal support, therefore the hulls oscillate simultaneously with the metal support. The heave response of the cabin under various control algorithms was observed.

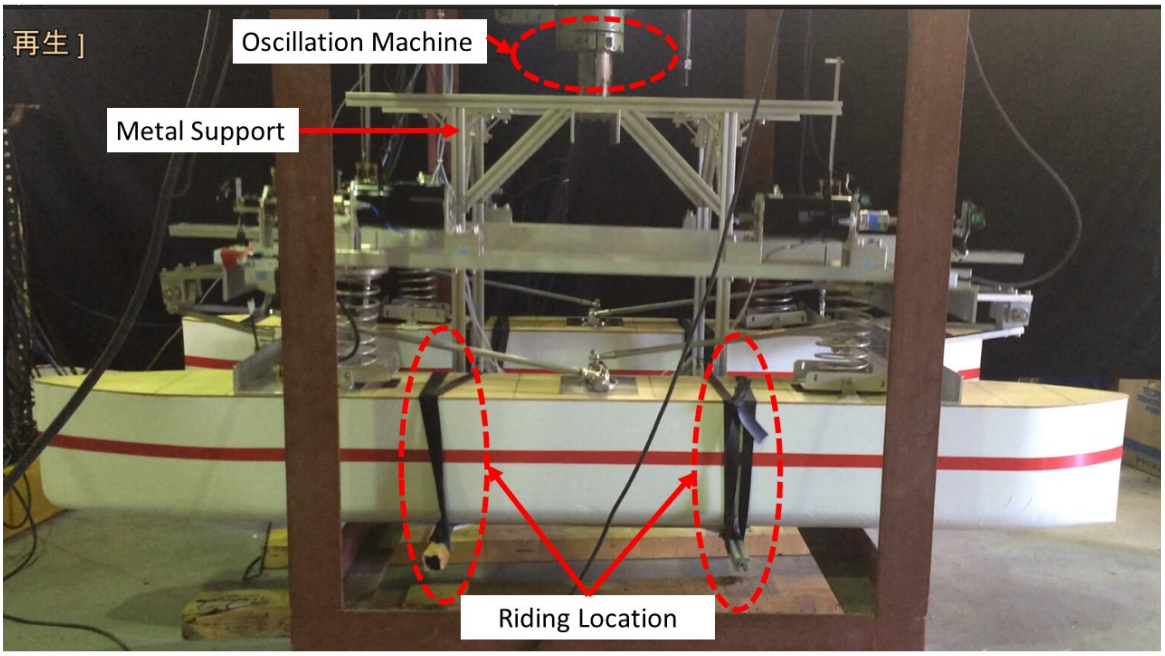

Figure 3.7: Bench test set up

The stroke amplitude of the hulls was set as 0.03 m, while the frequency was 0.8 Hz, 1.0 Hz, 1.2 Hz and 1.4 Hz, respectively. It was found that when the frequency was lower than 0.8 Hz, the relative displacement between the cabin and the hulls was small, the effect of the control system was hardly to be seen; while that above 1.4 Hz would exceed the capacity limitation of the oscillation machine.

20 group of data were recorded with a sampling frequency of 100 Hz. They were the acceleration of the cabin, the relative displacement between the cabin and the hulls, the motor terminal voltage, the motor current of the four suspension units, the input command voltage of the motor of three suspension units and the heave of the cabin.

The heave of the hulls was estimated according to the relation of the heave of the cabin and the relative displacement between the cabin and the hulls, which can be described as

$$z(t) = Z(t) - Z_r(t) \tag{3.37}$$

in which Z_r represents a mean value of the relative displacement of the four suspension units, a positive of which means a spring is extended, while that of negative means compressed. A

dimensionless heave of the cabin is defined by a ratio of the heave of the cabin to that of the hulls, which was written as

$$\eta_{zc} = \frac{Z_a}{z_a} \tag{3.38}$$

in which η_{zc} represents the dimensionless heave of the cabin, Z_a and z_a represents the amplitude of the heave of the cabin and the hulls, respectively.

Measured energy of the M/Gs, denoted as E_{ms}, was estimated by summing up the product of the measured motor terminal voltage and the motor current at four suspension units. It was expressed as

$$E_{ms} = \frac{1}{n}\sum_{i=1}^{4}\int_{t_0}^{t_0+nT} V_{t_i}(t)\cdot I_i(t)dt \tag{3.39}$$

in which T represents the oscillation period, V_t and I represent the measured motor voltage and current, respectively; i represents the location of a suspension units. A positive value of E_t means the energy was harvested, that of negative means consumed.

The energy dissipated by the winding resistor of the M/Gs, and that due to the resistance of the leading cable between the motor terminal and the control panel were regarded as energy loss, denoted as E_{wr} and E_{cr}, respectively. They are called **electrical energy loss**. Those components are always negative and can be obtained by

$$E_{wr} = -\frac{1}{n}\sum_{i=1}^{4}\int_{t_0}^{t_0+nT} R_{wr}\cdot I_i^2(t)dt \tag{3.40}$$

$$E_{cr} = -\frac{1}{n}\sum_{i=1}^{4}\int_{t_0}^{t_0+nT} R_{cr}\cdot I_i^2(t)dt \tag{3.41}$$

The relation of the **terminal energy** and the electrical energy loss were depicted in Fig.3.8. in which, **M/G energy**, denoted as E_{mg}, is defined as the pure energy that flows into or out of

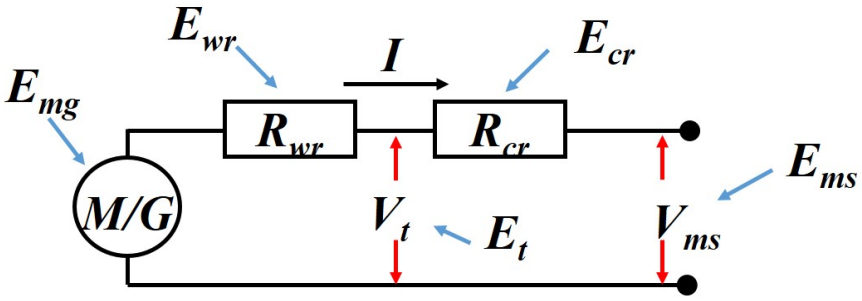

Figure 3.8: Energy product seen from motor terminal and inside of a motor

the M/G without any electrical energy loss. Under energy harvesting mode or integrated mode with energy harvesting mode in domination, a positive E_t can be obtained. Under a skyhook mode or an integrated mode with skyhook mode in domination, a negative E_t can be gained. In the following chapters the energy consumed at a skyhook mode or captured at an energy harvesting mode was represented by the terminal energy shown in Eq.(3.42).

$$\boxed{E_t = E_{mg} + E_{wr} = E_{ms} - E_{cr}} \tag{3.42}$$

3.3.2 Simulation Program for Bench Test

A one degree of freedom simulation program was built, the details of which were shown in Fig.3.9. The oscillation amplitude of the hulls was set as 0.03 m.

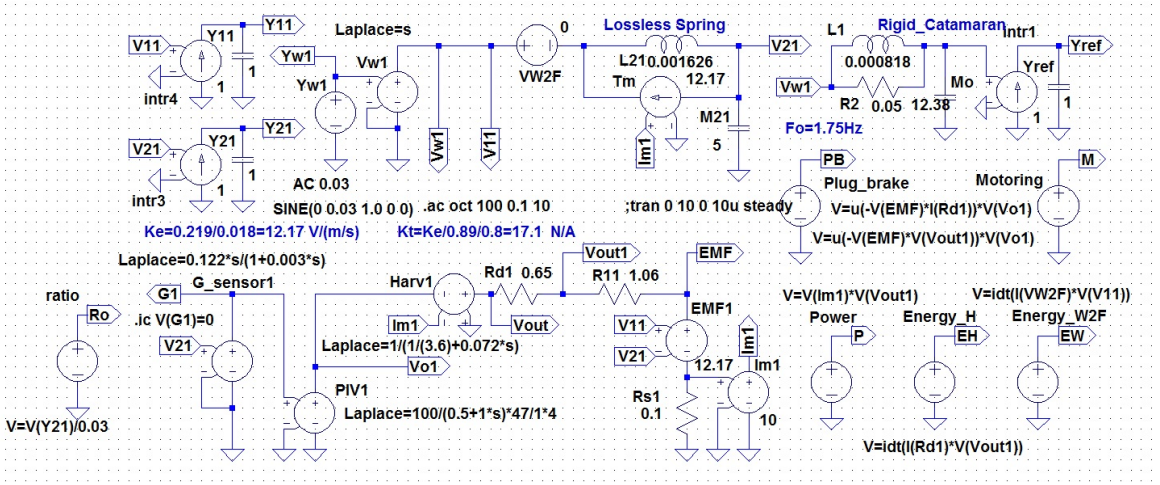

Figure 3.9: Simulation program of the bench test of WHzer-6

The main components and parameters in the program were listed.

- **transfer function**

  At skyhook mode, the transfer function of the I controller was showed as

$$H_{skh}(s) = 0.122 \cdot \frac{100}{0.5+s} \cdot \frac{47}{R_{sky}} \cdot 4 \tag{3.43}$$

  in which, R_{sky} was manually tuned to seek for a feasible range of the I gain.

  At energy harvesting mode, the transfer function was expressed as

$$H_{har}(s) = \frac{I_{m1}}{\frac{1}{R_L} + C_p \cdot s} \tag{3.44}$$

  in which, R_L and C_p are the parameter pairs shown in Table 2.6.

- **mass adjustment of the cabin**

  Known from Table 2.1 the sprung mass of the model ship was about 31.9 kg, which consist of the mass of the deck frame, the M/Gs, adjusting weight block used in tank test, and half of the mass of the suspension components, for instance the springs, Watt's links and Pantographs. The natural frequency was observed at 1.18 Hz in simulation with this sprung mass. However, the free decay test suggested that the natural frequency of the cabin was about 1.44 Hz. By tuning the mass value in the simulation, it was found that a natural frequency of 1.44 Hz can be observed if the mass was set as 20 kg, which is approximately equals to the mass of the deck frame and the M/Gs.

- **R_{sky} tuned for skyhook control mode**

  The R_{sky} was chosen as 4 kΩ, 10 kΩ, 20 kΩ, the corresponding I gain of the skyhook control were 573 ,229 ,115, respectively, according to Eq.(2.32).

- **R_L and C_p tuned for energy harvesting mode**

  Load resistor and padding capacitor were tuned to maximize the energy that can be captured at energy harvesting mode for each frequency.

- **free mode**

  Free mode was defined as a situation at which the control system was disabled, which resulted in a mass-spring-mass system. The I gain of the free mode can be regarded as 0.

- **oscillation frequency**

  The heave response of the cabin was simulated between 0.5 Hz and 2.0 Hz, so as to make a comparison with that of the bench test.

3.3.3 Heave Response of the Cabin in Simulation and Test

The dimensionless heave of the cabin was obtained by comparing the amplitude of the heave of the cabin to that of the hulls. A value of which less than 1 represents the heave of the cabin is smaller than the hulls, that of 1 implies they equal to each other.

Figure 3.10 showed the dimensionless heave of the cabin, the consumed power both in simulation and the test. The x axis represents the stroke frequencies, while y axis is the dimensionless heave of the cabin and the consumed power, respectively. The circles represent the results from the bench test, while the break lines represent that from the simulation in ideal condition, the one taking friction into account was represented by $*$. The estimation of the friction adopted the method of an equivalent viscous damper as described in Eq.(3.20). The calculation of the damping coefficients used the relative velocity between the cabin and the hulls as obtained from the bench test. For an ease comparison, the same color of the marks and curves represented the same test condition.

It was seen that at the free mode, a resonance was observed around 1.4 Hz. With a stronger I gain, heave of the cabin was reduced more at a given frequency. It also showed that the simulation result of the heave was slightly bigger than that of the test at the ideal condition, meanwhile the consumed power is smaller than that of the test, especially under higher I gain condition. The fluctuation of the power consumption in Fig.3.10(b) might be caused by small deviation of the stroke amplitude of the oscillation machine, which might not be 0.03 m as strictly as the one in simulation. It was also showed that the equivalent damping method reduced the gap between the ideal condition and the bench test, especially when the oscillation frequency was approaching the natural frequency of the cabin. It suggested that the aforementioned method of estimating friction might cause low accuracy when it was used at the frequency apart from the natural frequency.

A limitation of the I gain was found by the bench tests. It was observed that when the gain was set above 573, an unstable state of the control system was generated. Therefore, in the following towing tank test, the I gains were set smaller than this value, in other words, the chosen R_{sky} should be larger than 4 kΩ. The threshold value of I gain is expressed as

$$\boxed{G_i \leq 573} \tag{3.45}$$

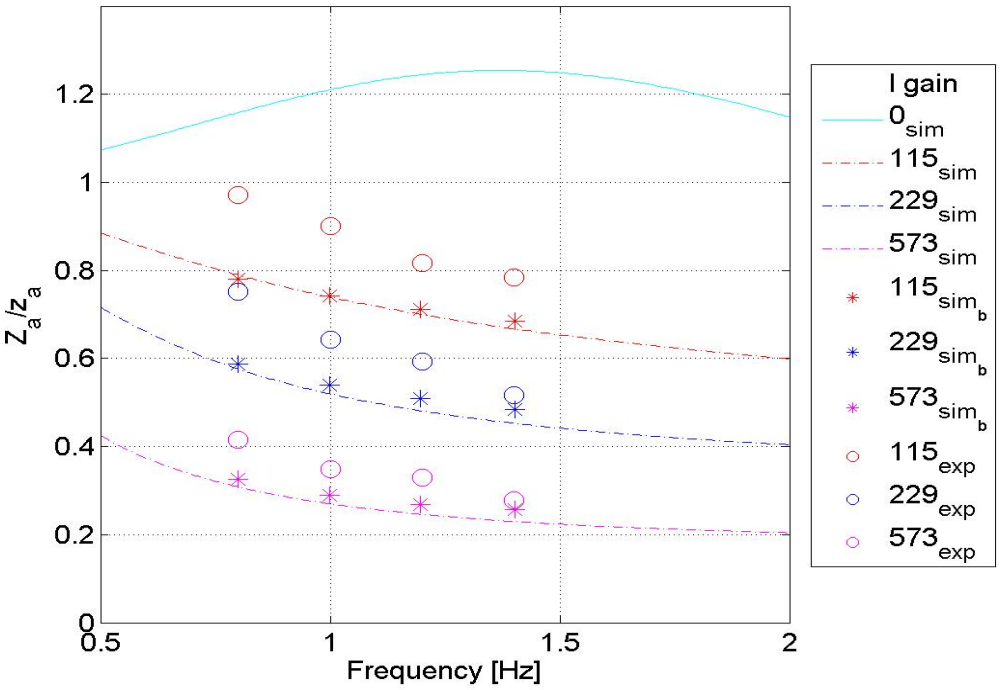

(a) Dimensionless heave

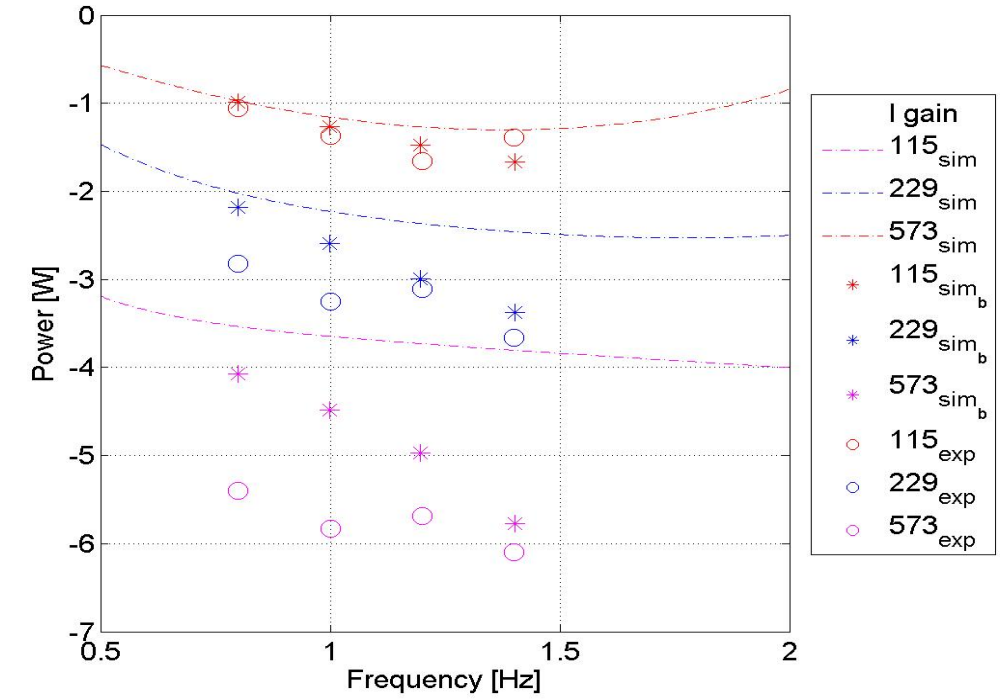

(b) Consumed Power

Figure 3.10: Simulation and experimental results of the dimensionless heave

3.3.4 Results of Wave Energy Harvesting

The energy harvesting mode was carried out with a stroke amplitude of 0.03 m and a frequency of 1.0 Hz. At the MPPT condition, the impact factor was tuned, therefore 5 cases of energy harvesting scenario were tested, as shown in Table 3.3. Case No.1 means the M/Gs were shorted in the electrical circuit, therefore the generated energy should close to zero, the heave of the cabin should be the smallest among all the cases. Case No.7 represents an open circuit, which can be regarded as a free mode, thus the produced energy should be zero and the heave of the cabin should be the largest among all the cases.

Table 3.3: Impact factors of the bench test under energy harvesting mode

Case No.	**1**	**2**	**3**	**4**	**5**	**6**	**7**
Impact Factor	SHORT	1/5	1/2	1	2	5	OPEN

Comparison between the bench test and the simulation with respect to heave and the power generation were showed in Fig.3.11. A gradually increasing of heave motion both in simulation and test was observed. case No.1 and case No.7 gave the smallest and the largest heave response, respectively, which matched the expectation.

Figure 3.11(b) depicted the amount of power that harvested in simulation and test in units of W. The simulation result suggested that the highest harvesting potential was obtained at case No.4, which represents the MPP condition at the frequency of 1.0 Hz. In other cases the amount of power was gradually reduced. The power of case No.1 in the test was supposed to be zero, however a certain amount of power was observed. By checking the current and the voltage of the M/Gs, it was found that the voltage was very small, in contrast, the current was large. It might be caused by an incomplete short circuit. Substituting which into Eq.(3.41), certain amount of power was obtained. Although, the trend of the power was not as clear as the one shown in the simulation, it still suggested that the MPP can be adopted as a reasonable condition in aiming of maximizing energy harvesting.

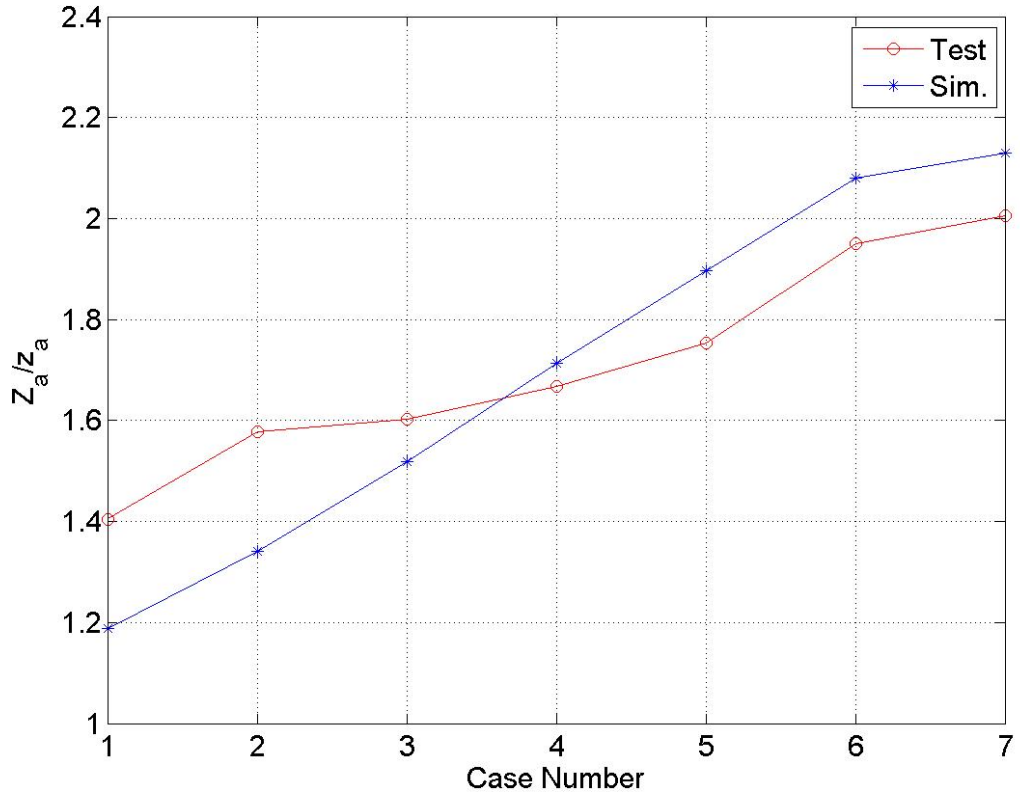

(a) Heave response

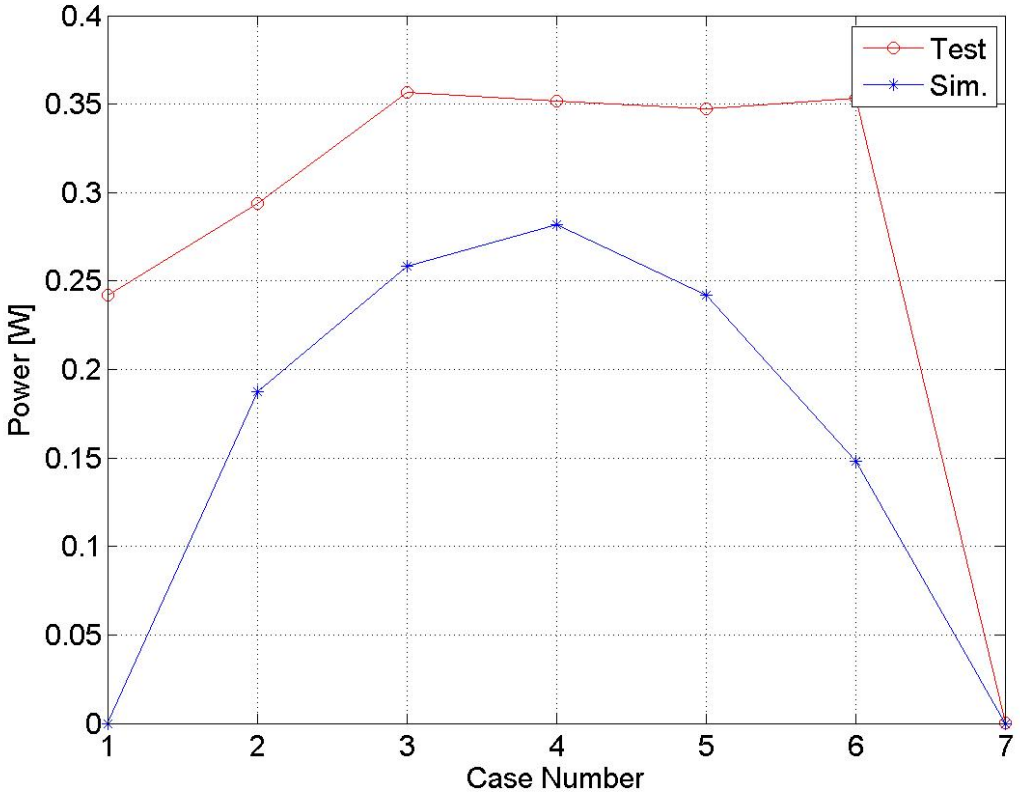

(b) Energy Harvesting

Figure 3.11: Bench test results on energy harvesting, $f = 1.0\,\mathrm{Hz}$

3.4 Summary

Through three types of the dry test, the performance of the suspension structure and the control system were evaluated. The results can be summarized as:

- The suspension structure and the control system were well-designed, the blushed DC motor was performing well in both skyhook mode and the energy harvesting mode.
- The heave response of the cabin in the bench test agreed reasonable with that in the simulation. Higher I gain contributed more in heave motion reduction, however, consumed more energy. $G_i = 573$ was the highest I gain for the skyhook control.
- Although, the magnitude of the energy harvested in the bench test differed with that in the simulation, the MPP obtained by the simulation program was regarded as valuable.
- The friction of the suspension components was numerically analyzed and was suggested to be represented by a viscous damper. The results showed that such analogy method was acceptable at a certain level.
- The dead zone of the suspensions was about 1 cm.

Chapter 4

Towing Tank Test in Regular Wave Conditions

4.1 General Description

A towing tank test was implemented at the Ocean Engineering Basin in the Chiba Campus of the University of Tokyo. Fig.4.1 showed the circumstance of the basin. It is 50 m in length, 10 m in width and 5 m in depth. A depth-adjustable floor can vary the water depth from 5 m to 0.5 m according to the requirements. A carriage is settled upon the tank with a towing speed up to 2.0 m/s. Wave makers are fit at one end of the basin, while wave absorbers are at the other end.

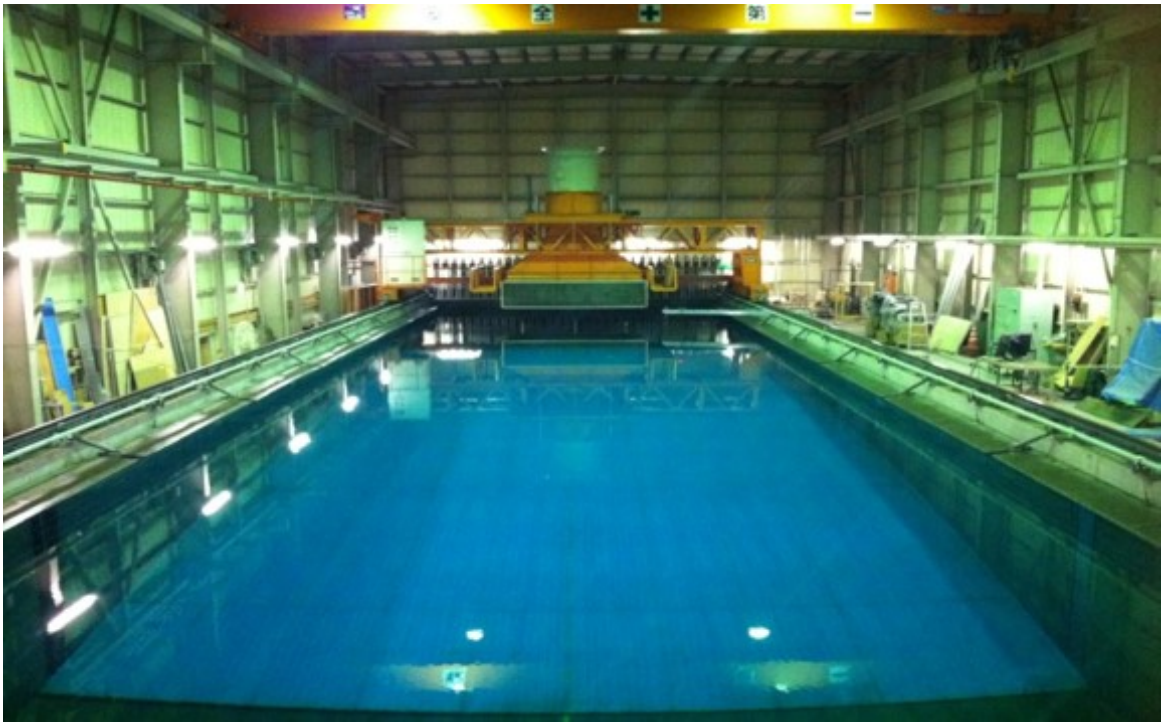

Figure 4.1: Ocean engineering basin of the University of Tokyo

The model ship was tested under five control modes: skyhook mode, MPPT mode, integrated control mode, free mode and rigid mode.

- **Skyhook mode**
  At the skyhook mode, four of the I controllers were exerted to minimize the motion of the cabin at its own location. The I gain of each controller was identical at a test run. The I gain, defined in Eq.(2.18), were 115, 229 and 573, respectively.

- **MPPT mode**
  At the maximum power point tracking mode, the electronic load pairs of the controller were changed at each wave frequency so as to guarantee the MPP was tracked. The MPPs, shown in Table 4.1, were found by 1 DOF quarter simulation program built in LTspice®. Known that the ship is a 9 DOF structure, therefore using the results suggested by the 1 DOF simulation may only give an approximation of the real maximum power point. In other words, the energy captured under those conditions can be increased if the real MPPs were found. To evaluate the characteristics of the wave energy harvesting mode, the impact factor of the MPPs, denoted as G_{MPPT} in Eq.(2.16), were tested with three values: 1/3, 1 and 3.

Table 4.1: MPPs for towing tank test

Frequency (Hz)	$C_p(\mu\text{F})$	$R_L(\text{k}\Omega)$
0.5	12	22
0.7	9	25
0.8	7	30
0.9	4	41
1.0	1.5	54
1.1	0.1	53
1.2	0.1	35
1.3	0.1	17
1.5	0.1	10

- **Integrated mode**
  At the integrated mode, the skyhook control and the MPPT control were combined in three ways as shown in Table 4.2, in which the impact factor of the MPPT and the gain of the I controller were tuned. Thus, the contribution of the skyhook control and the MPPT control in the motion response of the cabin and the wave energy capture ability were adjusted.

- **Free mode**
  Free mode is a test condition when the control system was turned off, the whole ship can be regarded as a mass-spring-mass system.

- **Rigid mode**
  By mounting four mental plates between the cabin and the hulls at the four corners, the suspensions were disabled, resulted in a solid connection between the cabin and the hulls, which was regarded as a rigid body. This mode was used as a reference system to evaluate the motion variance brought by the control systems.

The test was carried out in regular wave conditions which were listed in Table 4.3 for head wave condition and Table 4.4 for beam wave condition. The direction of wave propagation β was 180° and 90°. The towing speed was 0 m/s and 1.5 m/s, respectively.

Table 4.2: Integrated control settings

MPPT Mode	**Skyhook Mode**	**Integrated Control Description**
$G_{MPPT} = 1$	$G_i = 573, G_{Sky} = 1$	The most oscillating condition combined with the strongest motion elimination condition, the impact factors of the two are both 1.
$G_{MPPT} = 1$	$G_i = 229, G_{Sky} = 1$	The most oscillating condition combined with a less strong motion elimination condition, the impact factor of the two are both 1.
$G_{MPPT} = 1/3$	$G_i = 573, G_{Sky} = 1$	The less oscillating condition combined with the strongest motion elimination condition, while the impact factor of the MPPT is 1/3, that of the skyhook is 1.

At each head wave condition, all the five modes were implemented; at beam wave condition, integrated mode was not carried out, skyhook mode was only tested in the highest I gain condition due to the limitation of time. To avoid the disturbance brought by a previous test run, the time interval between two tests was $20 \sim 25$ min. The sampling frequency for the data recording was 1000 Hz.

The acquired data includes: water surface elevation; the heave, pitch and roll motion of the cabin; the relative displacement between the cabin and the hulls as well as the acceleration at four suspension sites; the current of the four M/Gs; the terminal voltage of the four M/Gs; the input control voltage of the four M/Gs.

The motion response of the hulls were not directly measured, but estimated according to the motion response of the cabin and the relative displacement. The relation can be written as

$$z(t) = Z(t) - \frac{1}{4} \cdot (Z_{FL}(t) + Z_{FR}(t) + Z_{RL}(t) + Z_{RR}(t)) \tag{4.1}$$

$$\theta(t) = \Theta(t) - atan\left(\frac{Z_{FL}(t) + Z_{FR}(t) - Z_{RL}(t) - Z_{RR}(t)}{0.72}\right) \cdot \frac{180}{\pi} \tag{4.2}$$

$$\phi(t) = \Phi(t) - atan\left(\frac{Z_{FL}(t) + Z_{RL}(t) - Z_{FR}(t) - Z_{RR}(t)}{0.64}\right) \cdot \frac{180}{\pi} \tag{4.3}$$

in which, Z_{FL}, Z_{FR}, Z_{RL}, Z_{RR} represents the relative displacement at FL, FR, RL and RR of the ship; Z, θ and Φ represents the heave, pitch and roll of the cabin, z, θ and ϕ represents that of the hulls; 0.72 and 0.64 are the distance between the front and rear, the left and right suspension units, respectively, as depicted in Fig.2.4.

According to the linear wave theory, in the wave propagation direction the energy transport per unit time per unit crest length is a product of the wave group velocity and the time averaged wave energy of per unit area of the wave. In regular wave condition, the power carried by per unit length of crest can be described as

$$\overline{P_w} = \frac{g^2 \rho}{32\pi} \cdot H^2 \cdot T \tag{4.4}$$

where, ρ is the water density, g is the acceleration of gravity, H and T are the wave height and period, respectively.

The index used to evaluate the energy production seen at the terminal of a M/G is a ratio of the energy coming in or out at the M/Gs to that carried by the waves with a crest length as same as the width of the hulls. It can be expressed as

$$\mu = \frac{\overline{P_{M/G}}}{2B \cdot \overline{P_w}} \cdot 100\% \tag{4.5}$$

where B represents the width per hull; a positive value of μ means wave energy was captured, it is named as **wave energy capture width ratio** (**CWR**), while a negative value represents that amount of energy was consumed by the control system.

Table 4.3: Head wave conditions

Period (s)	**Frequency** (Hz)	**Amplitude** (cm)	**Wave Slope**
0.67	1.5	1.12	0.10
0.77	1.3	1.47	0.10
0.83	1.2	1.71	0.10
0.91	1.1	2.06	0.10
1.00	1.0	2.48	0.10
1.11	0.9	3.06	0.10
1.25	0.8	1.94	0.05
1.43	0.7	2.51	0.05
2.00	0.5	4.97	0.05

Table 4.4: Beam wave conditions

Period (s)	**Frequency (Hz)**	**Amplitude (cm)**	**Wave Slope**
0.67	1.5	1.12	0.10
0.77	1.3	1.47	0.10
0.83	1.2	1.71	0.10
0.91	1.1	2.06	0.10
1.00	1.0	2.48	0.10
1.11	0.9	3.06	0.10
1.25	0.8	3.88	0.10
1.43	0.7	5.08	0.10
2.00	0.5	4.97	0.05

4.2 Results

4.2.1 Head Wave Condition

The results at the head wave condition with forward speed of 0 m/s and 1.5 m/s were showed from Fig.4.2 to Fig.4.18. The x axis represents the angular frequency of encounter, while the y axis represents the corresponding dimensionless values.

The heave of the cabin and the hulls were given from Fig.4.2 to Fig.4.6. The dimensionless heave was obtained by calculating the ratio of the amplitude of the heave response to that of the incident waves.

The pitch of the cabin and the hulls were given from Fig.4.7 to Fig.4.11. The dimensionless pitch was obtained by calculating the ratio of the amplitude of the pitch response to the wave slope of the incident waves.

The relative displacement between the cabin and the hulls were given from Fig.4.12 to Fig.4.16. The dimensionless relative displacement was obtained by calculating the ratio of the amplitude of the relative displacement to that of the incident waves.

The power production at the skyhook mode, MPPT mode and integrated mode were given from Fig.4.17 to Fig.4.18. The dimensionless power production was obtained by Eq.4.5.

4.2.2 Heave Response at Skyhook Mode

Figure 4.2 depicted the heave response of the cabin and the hulls under head wave conditions without forward speed. The black-circle line represents the rigid mode, which is a reference system for motion response evaluation. It was seen in Fig.4.2(a) that a small peak and a large peak occurred around 5 rad/s and 7.5 rad/s. The small peak can be regarded as a coupled heave response due to the pitch resonance of the cabin that happened at 5 rad/s, which can be seen in Fig.4.7(a). The big peak was caused by the resonance of the heave of the cabin, whose coupling effect on the pitch motion, however, was not seen in Fig.4.7(a). The blue-diamond line in Fig.4.2(a) represents the free mode. It suggested that when the frequency was below 7 rad/s, the heave of the cabin at the free mode was larger than that at the rigid mode. Conversely, above 7 rad/s, the heave of the cabin at the free mode was smaller than that at the rigid mode. It also showed that with higher I gain, the heave of the cabin was reduced more, however, such effect was not clear on the hulls as shown in Fig.4.2(b). In which, the heave of the hulls under control algorithms were approximately at the same level.

Figure 4.3 demonstrated the heave response of the cabin and the hulls under head wave conditions with forward speed of 1.5 m/s. In Fig.4.3(a), at the free mode a significant resonance of the cabin was observed around 7 rad/s, which was smaller at rigid mode. It also showed that below 10 rad/s, higher I gain contributed more in the heave reduction of the cabin, whereas above 10 rad/s the effect of the I gain tuning on heave reduction was not significant. In Fig.4.3(b), the heave response at the free mode differed from the other modes, a deep trough was observed around 9 rad/s and a sharp peak was seen around 14 rad/s. It was seen that below 8 rad/s I gain of 573 eliminated the heave of the hulls more comparing to other I gains, but it was reversed while the encounter frequency increases. Especially from 8 rad/s to 12 rad/s, the heave of the hulls at higher I gain scenario was larger.

Heave Response at Skyhook Mode, $v = 0\,\mathrm{m/s}$, $\beta = 180°$

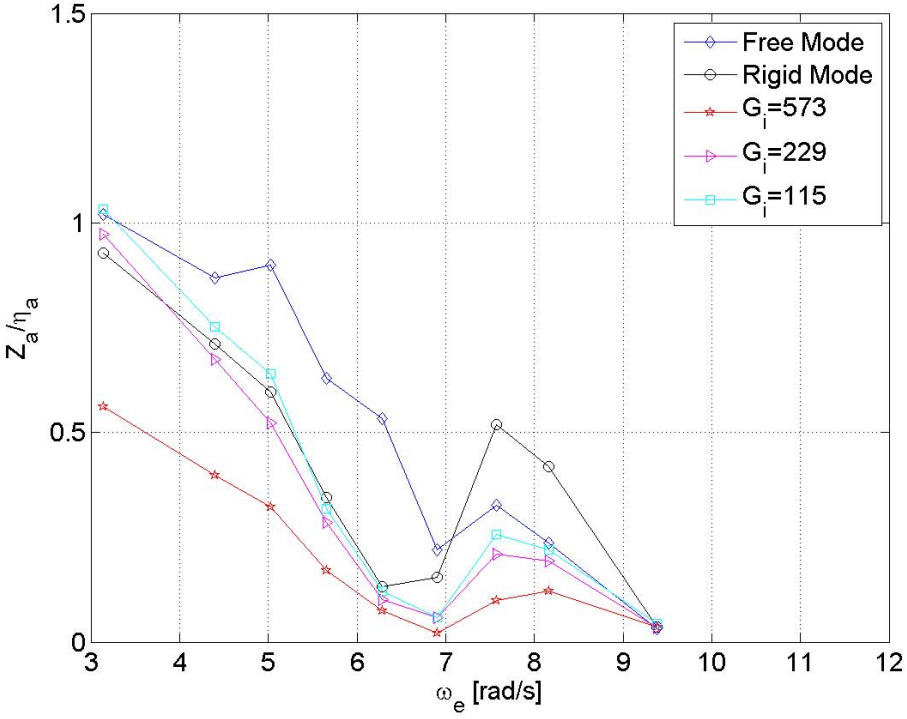

(a) Heave of the cabin

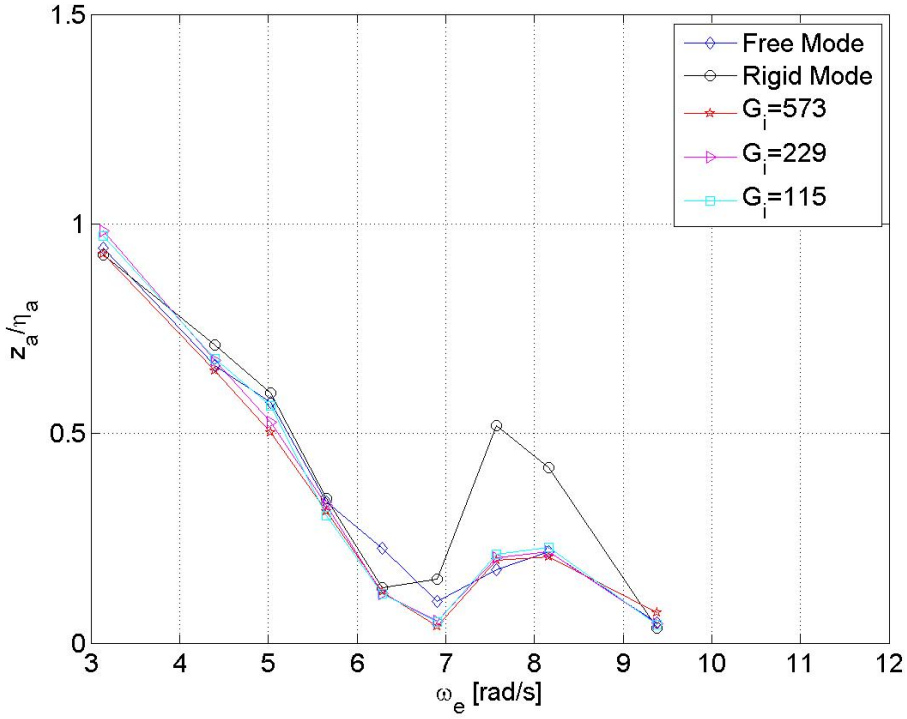

(b) Heave of the hulls

Figure 4.2: Heave of the cabin and the hulls at skyhook mode without forward speed

Heave Response at Skyhook Mode, $v = 1.5\,\mathrm{m/s}$**,** $\beta = 180°$

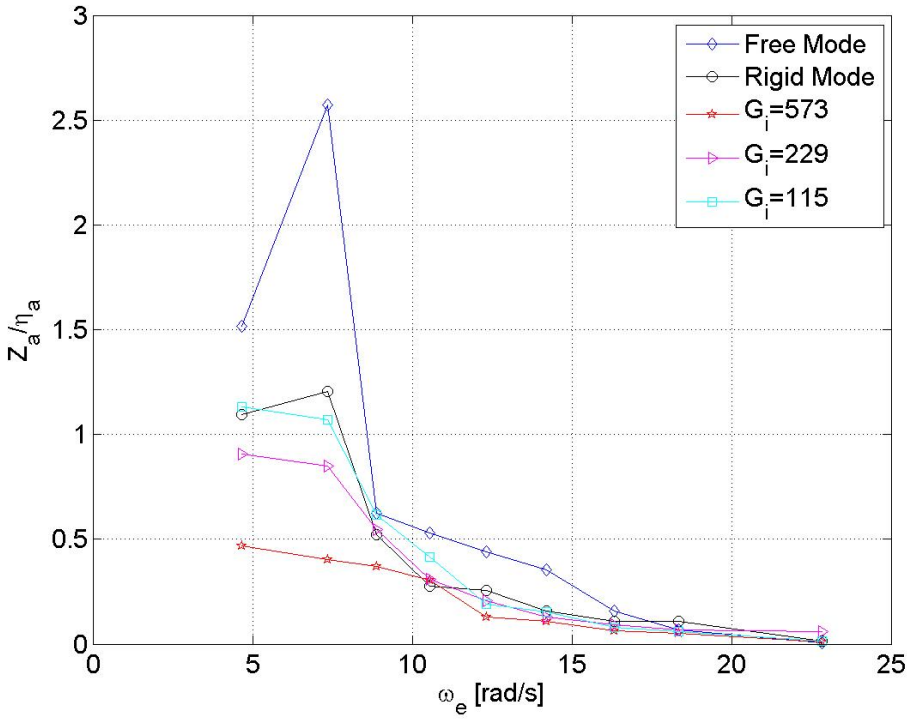

(a) Heave of the cabin

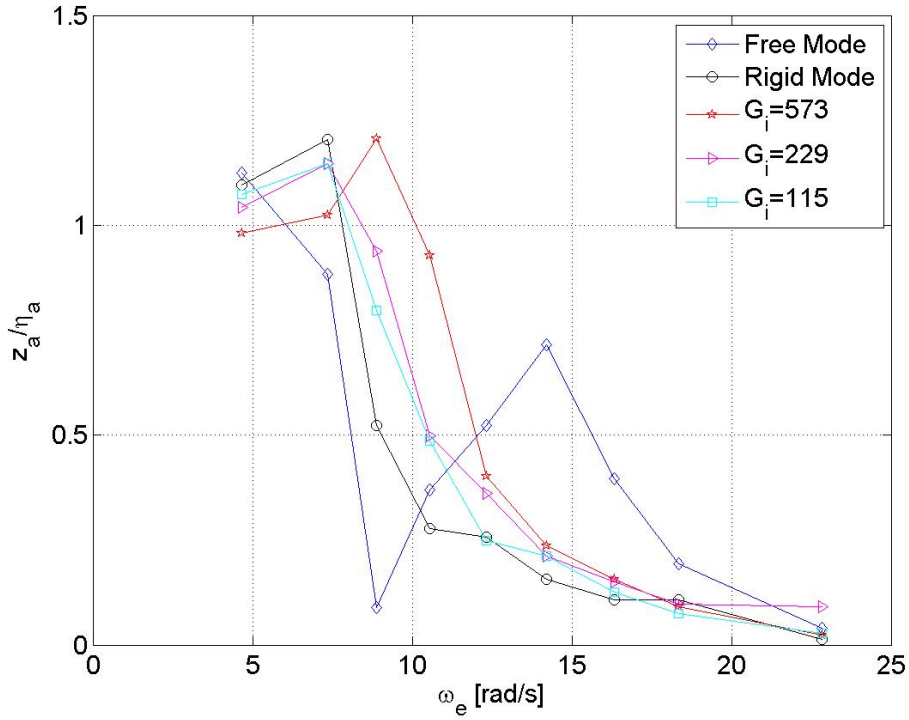

(b) Heave of the hulls

Figure 4.3: Heave of the cabin and the hulls at skyhook mode with forward speed of 1.5 m/s

4.2.3 Heave Response at MPPT Mode

Figure 4.4 showed the heave response of the cabin and the hulls under head wave conditions without forward speed. In Fig.4.4(a), the heave of the cabin at the MPPT mode was analogous to that at the free mode. They were higher than that at the rigid mode below 7 rad/s, while lower than the rigid model when it was above 7 rad/s. It can be regarded as the MPPT controller enlarged the heave of the cabin, nevertheless, its effect on the hulls was not observed in Fig.4.4(b).

Figure 4.5 gave the heave response of the cabin and the hulls under head wave conditions with forward speed of 1.5 m/s. Heave of the cabin shown in Fig.4.5(a) showed similar characteristics as given in Fig.4.4(a) that the heave of the cabin was larger than that at the rigid mode, and was approaching that at the free mode. It was observed in Fig.4.5(b) that at lower frequency domain the heave of the hull at the MPPT mode were lower than that at the rigid mode, however, along with the increase of the encounter frequency, especially above 10 rad/s, the situation was reversed. The heave of the hulls at the rigid mode turned to be the smallest one.

Heave Response at MPPT Mode, $v = 0\,\mathrm{m/s}$**,** $\beta = 180°$

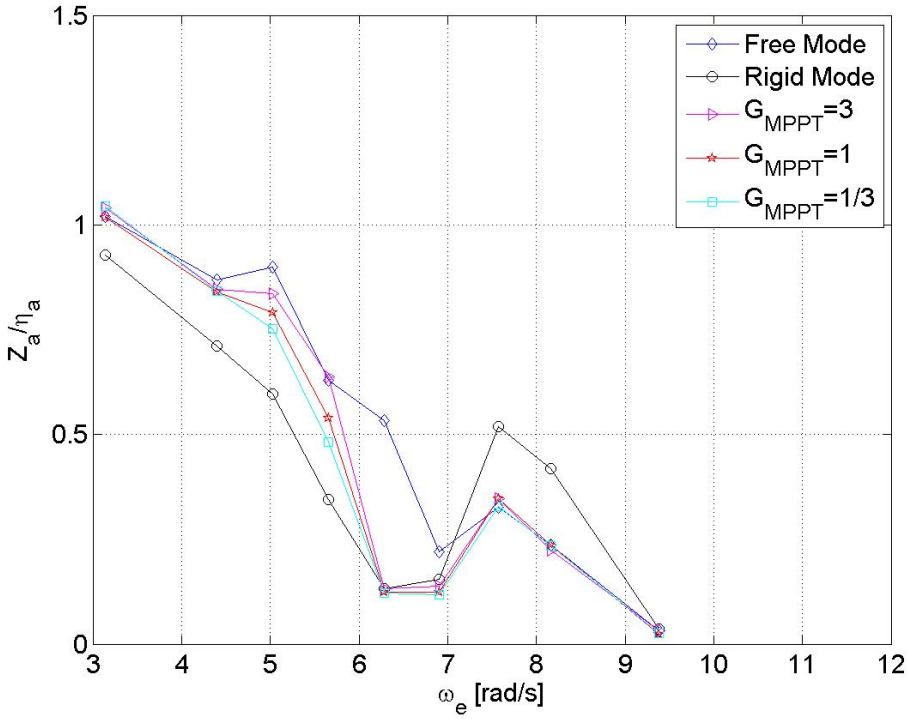

(a) Heave of the cabin

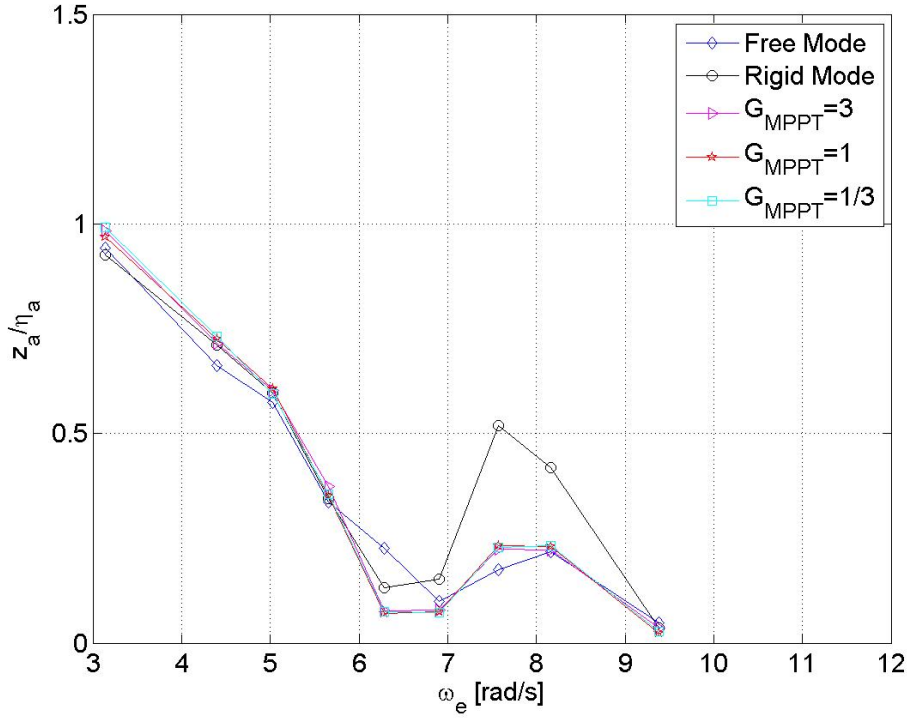

(b) Heave of the hulls

Figure 4.4: Heave of the cabin and the hulls at MPPT mode without forward speed

Heave Response at MPPT Mode, $v = 1.5\,\mathrm{m/s}$**,** $\beta = 180°$

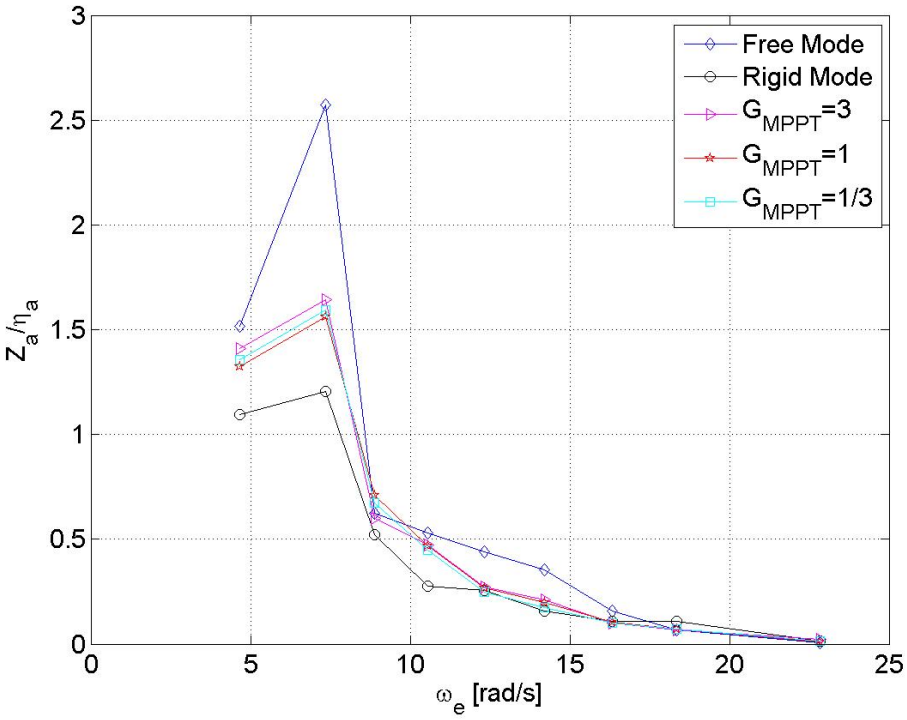

(a) Heave of the cabin

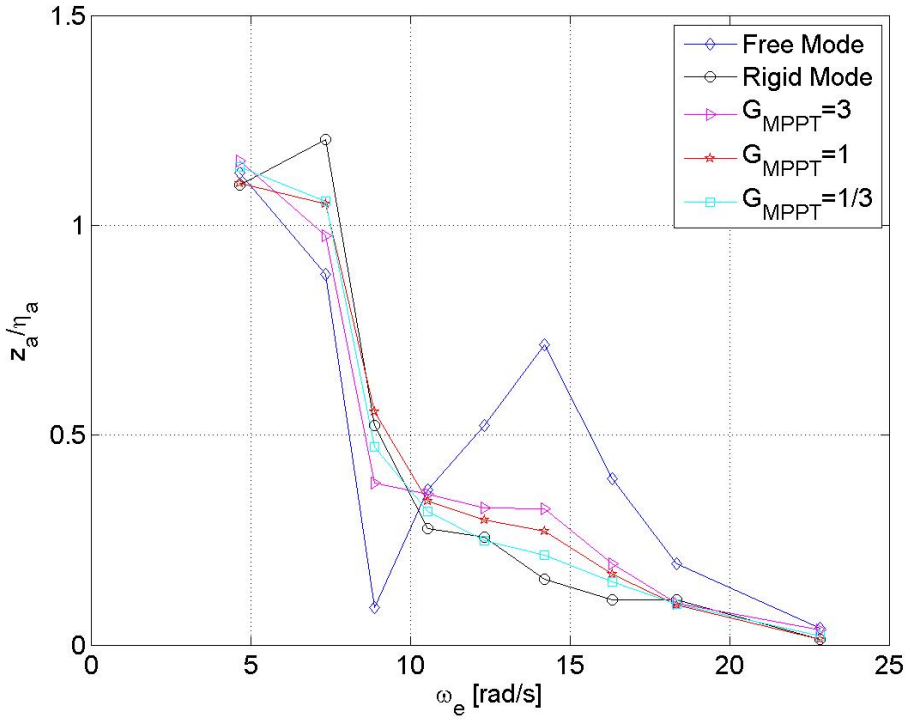

(b) Heave of the hulls

Figure 4.5: Heave of the cabin and the hulls at MPPT mode with forward speed of 1.5 m/s

4.2.4 Heave Response at Integrated Mode

Figure 4.6 showed the heave response of the cabin and the hulls under head wave conditions with forward speed of 1.5 m/s. When adopted a higher I gain as 573, tuning the impact factor of MPPT mode from 1 to 1/3 did not yield obvious effect on the heave of the cabin, however, certain increment of the heave of the hulls was observed below 10 rad/s in Fig.4.6(b). When adopted the MPPT mode with an impact factor of 1, tuning the gain of the I controller from 229 to 573 produced a significant heave reduction of the cabin, especially at the frequency lower than 10 rad/s.

Heave Response at Integrated Mode, $v = 1.5\,\mathrm{m/s}$**,** $\beta = 180°$

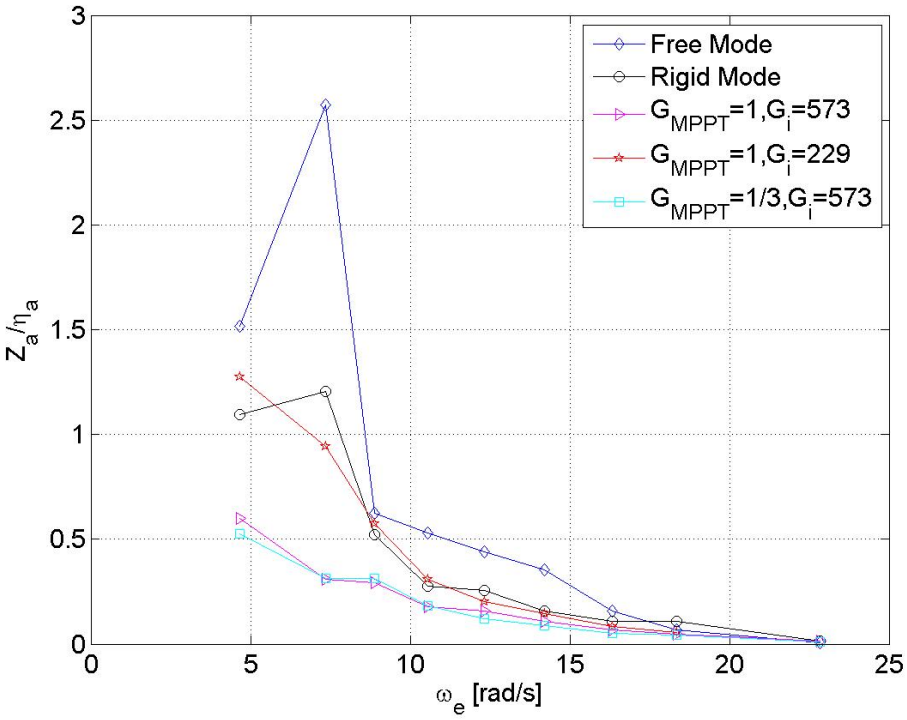

(a) Heave of the cabin

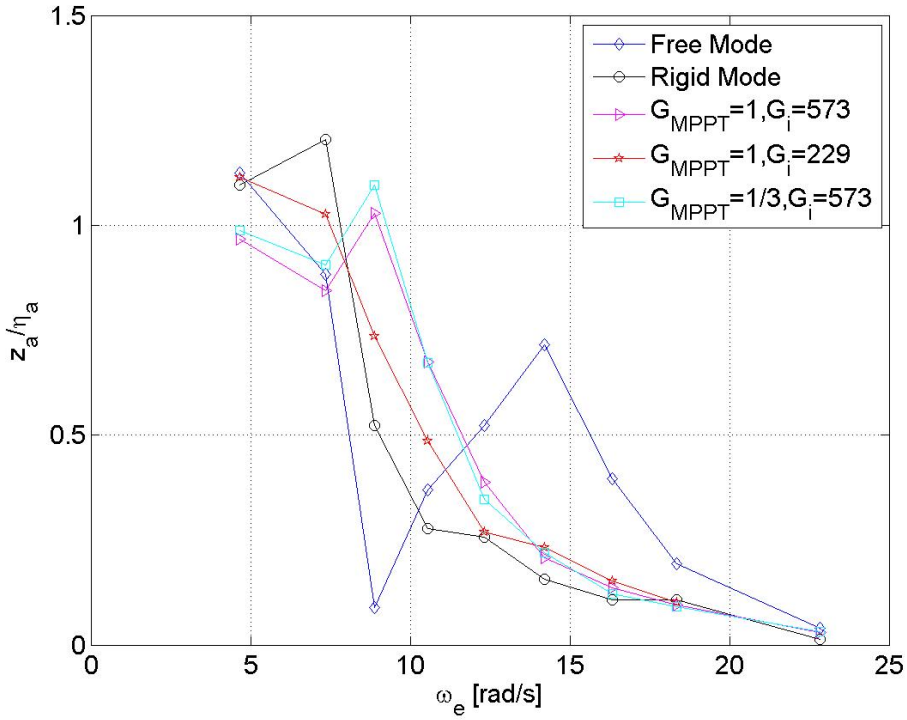

(b) Heave of the hulls

Figure 4.6: Heave of the cabin and the hulls at integrated mode with forward speed of 1.5 m/s

4.2.5 Pitch Response at Skyhook Mode

Figure 4.7 depicted the pitch response of the cabin and the hulls under head wave conditions without forward speed. The blue-diamond line represents the free mode, an obvious resonance of the cabin was observed around 5 rad/s in Fig.4.7(a), while at the rigid mode, which was represented by the black-circle line, such resonance was not obvious. It implied that this resonance was affected by the mass distribution of the cabin and the compression spring constant. It also can be seen that the pitch of the cabin below 5.8 rad/s at the free mode was larger than that at the rigid mode, which was smaller when the encounter frequency was above 5.8 rad/s. Tuning the I gain from 115 to 573 produced a significant pitch reduction of the cabin. The magnitude of which was smaller than that at the rigid mode and the free mode. It implied that the I controller worked effectively in pitch elimination of the cabin. When tuning the I gain, the pitch of the hulls did not vary as much as the cabin did. However, it was seen that at the skyhook mode the pitch of the hulls was larger than that at the free mode, but smaller than that at the rigid mode. It revealed that introducing skyhook control from the free mode reduced the pitch of the cabin but with an expense of increasing that of the hulls. However, if it was introduced from the rigid mode both the pitch of the cabin and the hulls were reduced.

Figure 4.8 showed the pitch response of the cabin and the hulls under head wave conditions with forward speed of 1.5 m/s. Around 5 rad/s, an aggressive pitch motion of the cabin was observed at the free mode, which was smaller at the rigid mode. It was reduced greatly along with an increment of the I gain from 115 to 573. A resonance of the hulls occurred around 7.5 rad/s when the I gain was at 229 and 573 as shown in Fig.4.8(b). At the same frequency, a peak of the cabin with I gain of 573 was also observed. It demonstrated that higher I gain contributed more in the pitch reduction of the cabin but may produce an increment of the pitch of the hulls.

Pitch Response at Skyhook Mode, $v = 0\,\mathrm{m/s}$**,** $\beta = 180°$

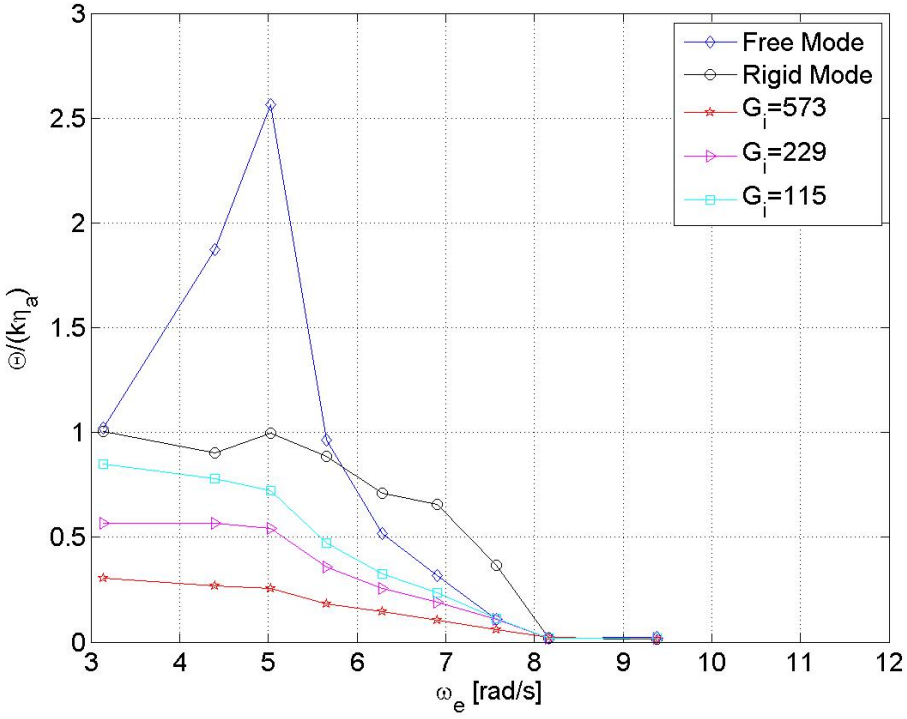

(a) Pitch of the cabin

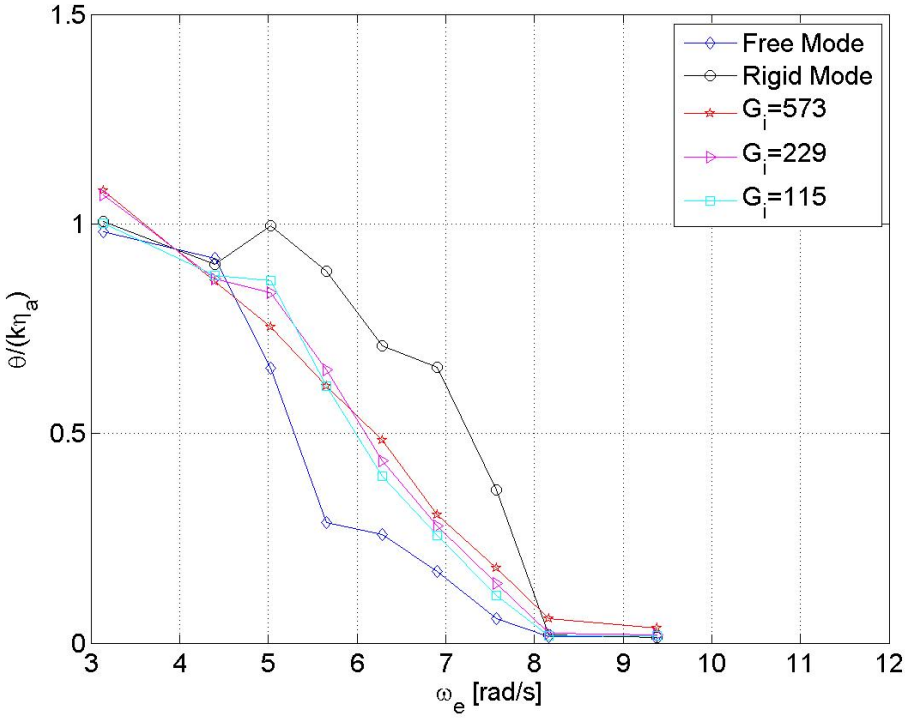

(b) Pitch of the hulls

Figure 4.7: Pitch of the cabin and the hulls at skyhook mode without forward speed

Pitch Response at Skyhook Mode, $v = 1.5\,\mathrm{m/s}$**,** $\beta = 180°$

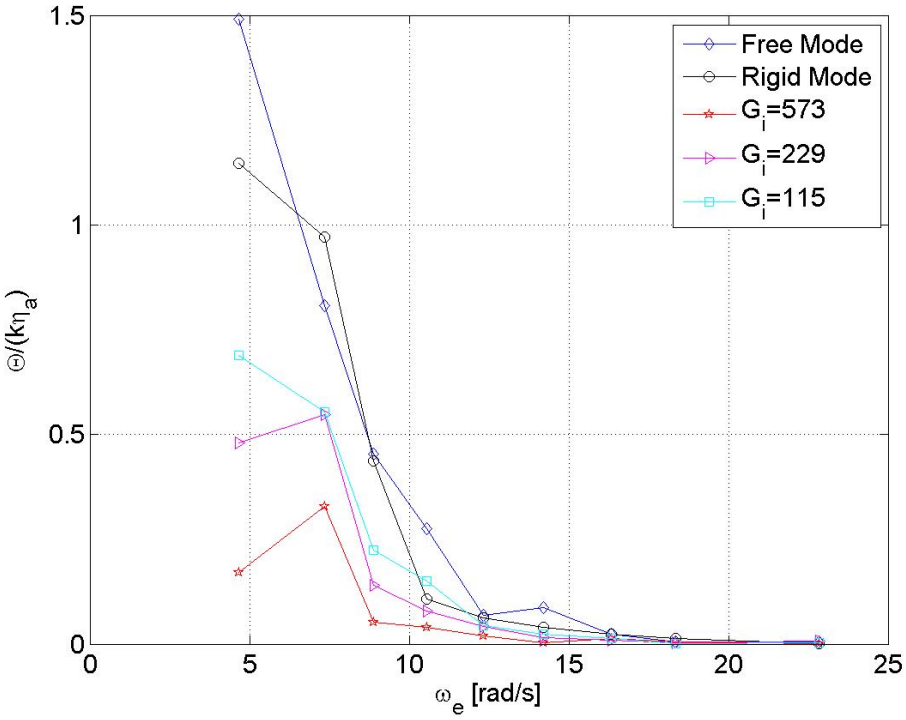

(a) Pitch of the cabin

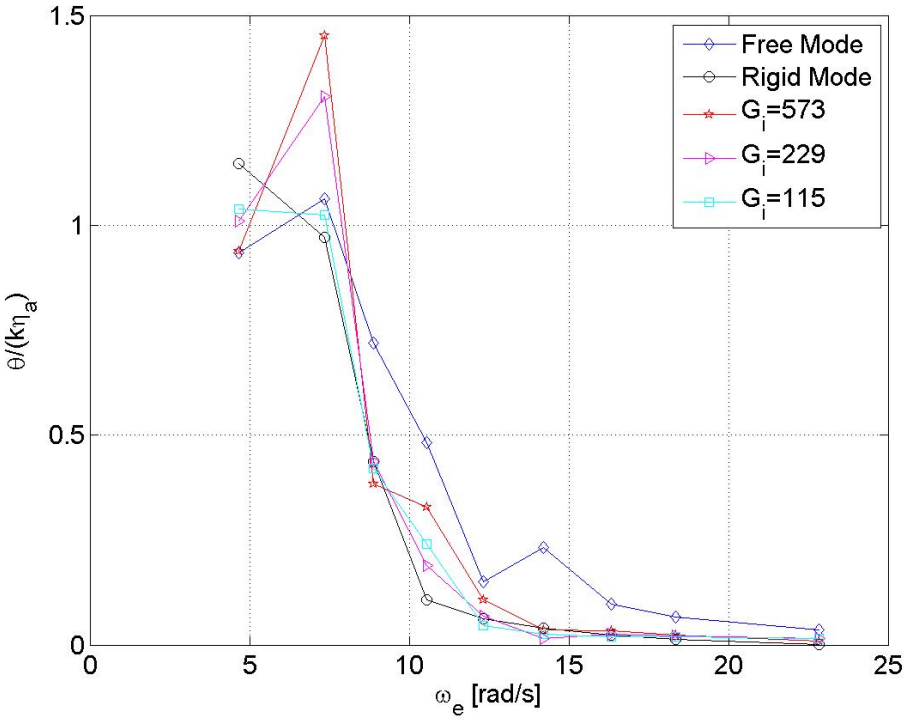

(b) Pitch of the hulls

Figure 4.8: Pitch of the cabin and the hulls at skyhook mode with forward speed of 1.5 m/s

4.2.6 Pitch Response at MPPT Mode

Figure 4.9 depicted the pitch response of the cabin and the hulls under head wave conditions without forward speed. The impact factor of the MPPT mode was tuned to validate the reliability of the maximum power points suggested by the simulation program. It was showed in Fig.4.9(a) that when the frequency was below 5.5 rad/s, the pitch of the cabin was larger than that at the rigid mode but smaller than that at the free mode. When it was above 5.5 rad/s, the pitch of the cabin at MPPT mode turned to be smaller than that at both the rigid mode and the free mode. In Fig.4.9(b), it can be seen that with a larger impact factor the pitch of the hulls was relatively smaller. In most of the frequencies, the pitch of the hulls at MPPT mode was smaller than that at the rigid mode but larger than that at the free mode.

Figure 4.10 depicted the pitch response of the cabin and the hulls under head wave conditions with forward speed of 1.5 m/s. Tuning of the impact factor of the MPPT mode did not show obvious influence on the pitch of the cabin, since they were similar with each other as can be seen in Fig.4.9(a). However, Fig.4.9(b) showed that the pitch of the hulls varied slightly due to the variance of the impact factor. With a higher value of the impact factor, the pitch of the hulls was relatively larger.

Pitch Response at MPPT Mode, $v = 0\,\mathrm{m/s}$**,** $\beta = 180°$

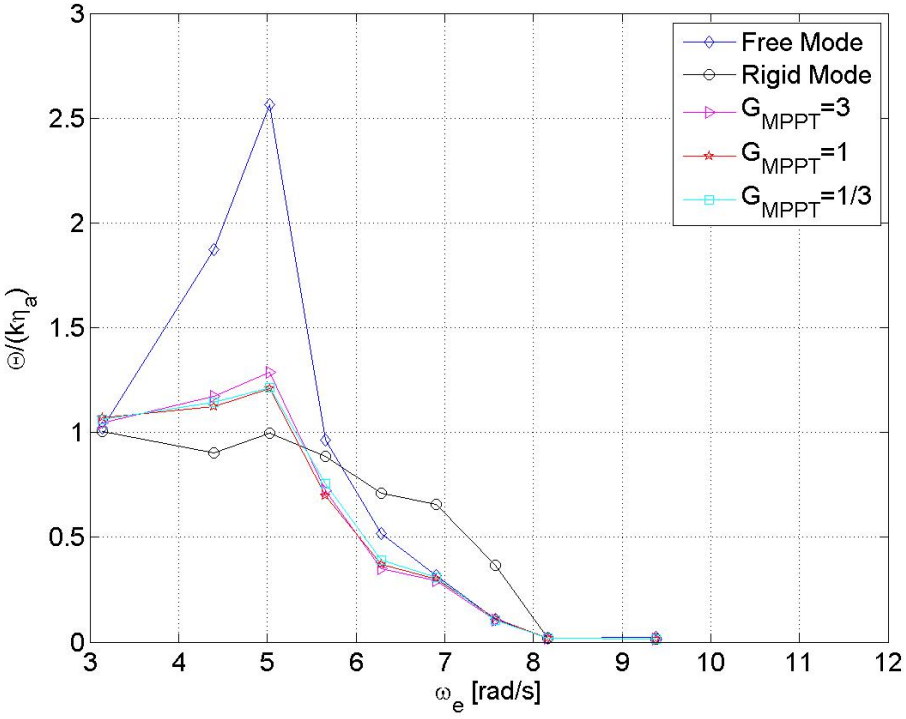

(a) Pitch of the cabin

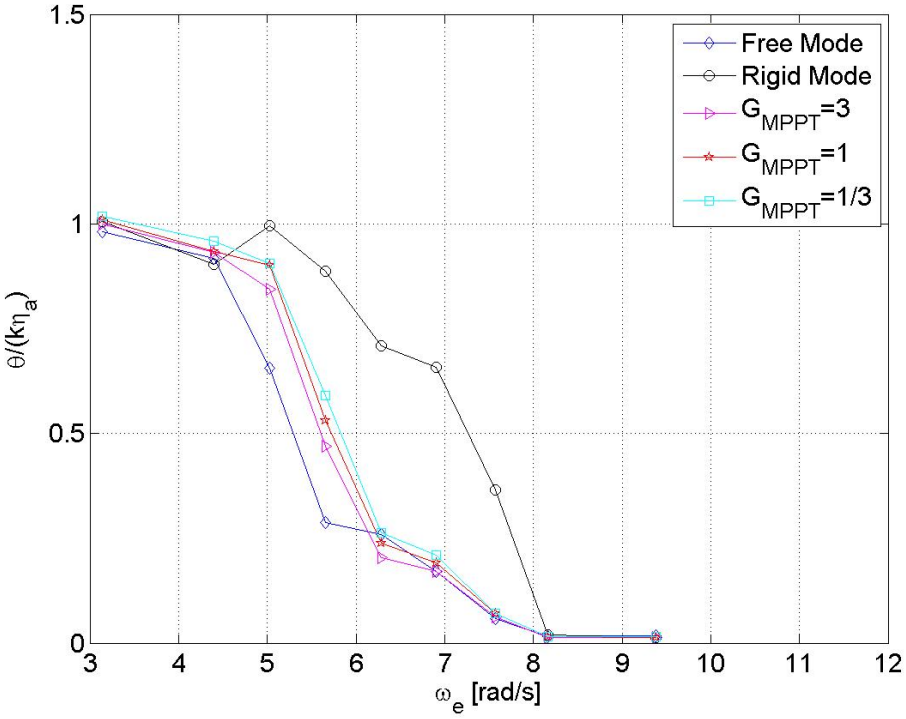

(b) Pitch of the hulls

Figure 4.9: Pitch of the cabin and the hulls at MPPT mode without forward speed

Pitch Response at MPPT Mode, $v = 1.5\,\mathrm{m/s}$**,** $\beta = 180°$

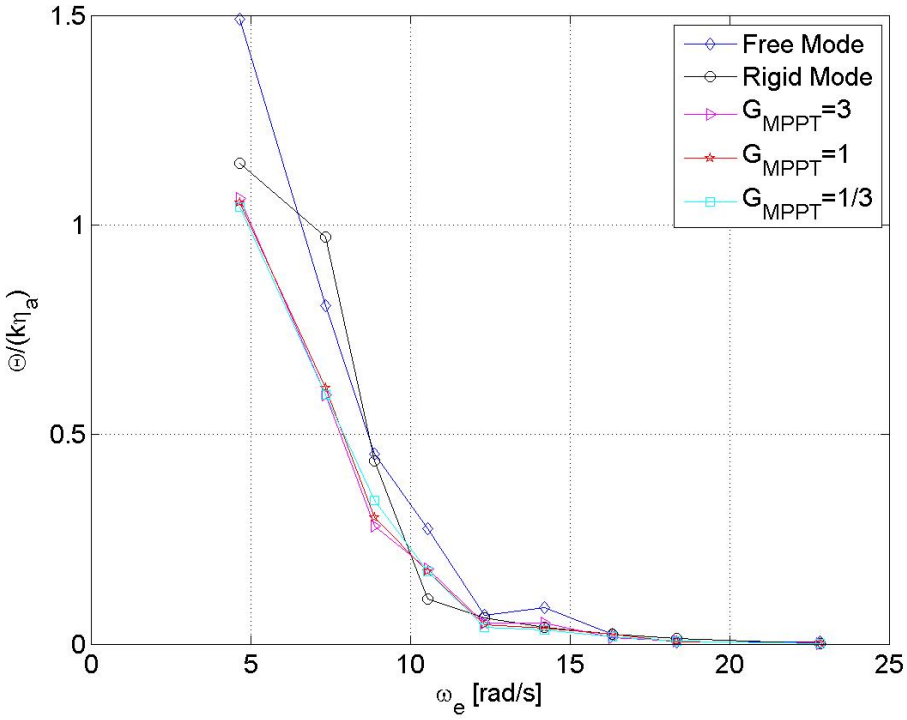

(a) Pitch of the cabin

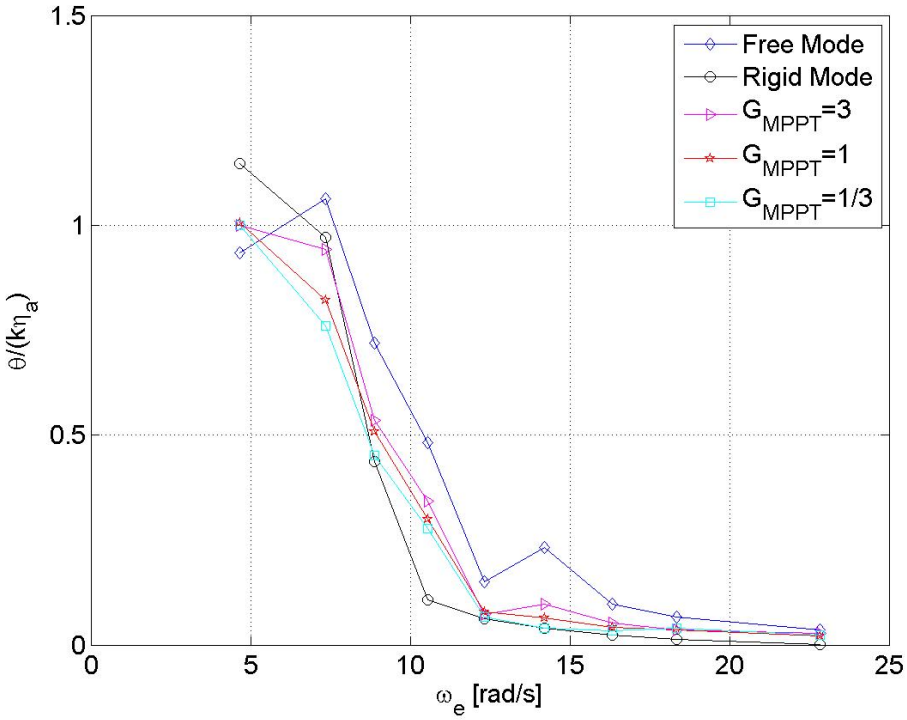

(b) Pitch of the hulls

Figure 4.10: Pitch of the cabin and the hulls at MPPT mode with forward speed of 1.5 m/s

4.2.7 Pitch Response at Integrated Mode

Figure 4.11 depicted the pitch response of the cabin and the hulls under head wave conditions with forward speed of 1.5 m/s. The pitch of the cabin at the integrated mode was reduced significantly if the encounter frequency was below 10 rad/s, especially when it adopted a higher I gain, which can be seen in Fig.4.11(a). It also showed that tuning the impact factor of the MPPT component at an integrated mode did not produce obvious variance of the pitch motion of the cabin after 7.5 rad/s, as well as that of the hulls. In Fig.4.11(b), a resonance of the pitch of the hulls was observed around 7.5 rad/s, which was similar to that shown in Fig.4.8(b). Besides, the heave of the cabin and the hulls at integrated mode with an I gain of 573 was also analogous to that at the skyhook mode if one compares Fig.4.6 to Fig.4.3. It implied that the skyhook controller with an I gain of 573 may be the dominant component in this integrated mode.

Pitch Response at Integrated Mode, $v = 1.5\,\mathrm{m/s}$, $\beta = 180°$

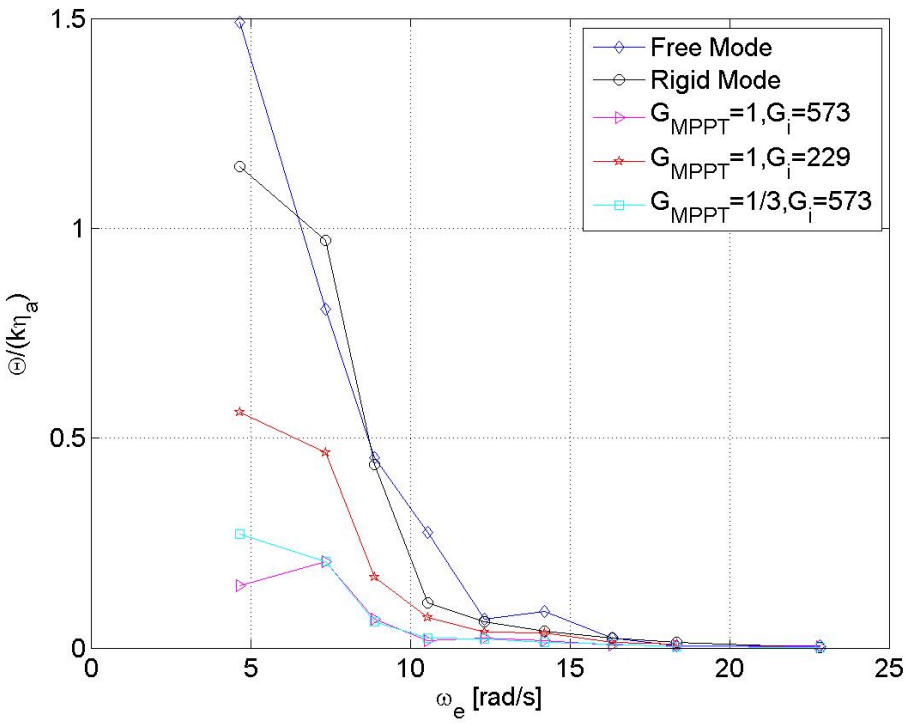

(a) Pitch of the cabin

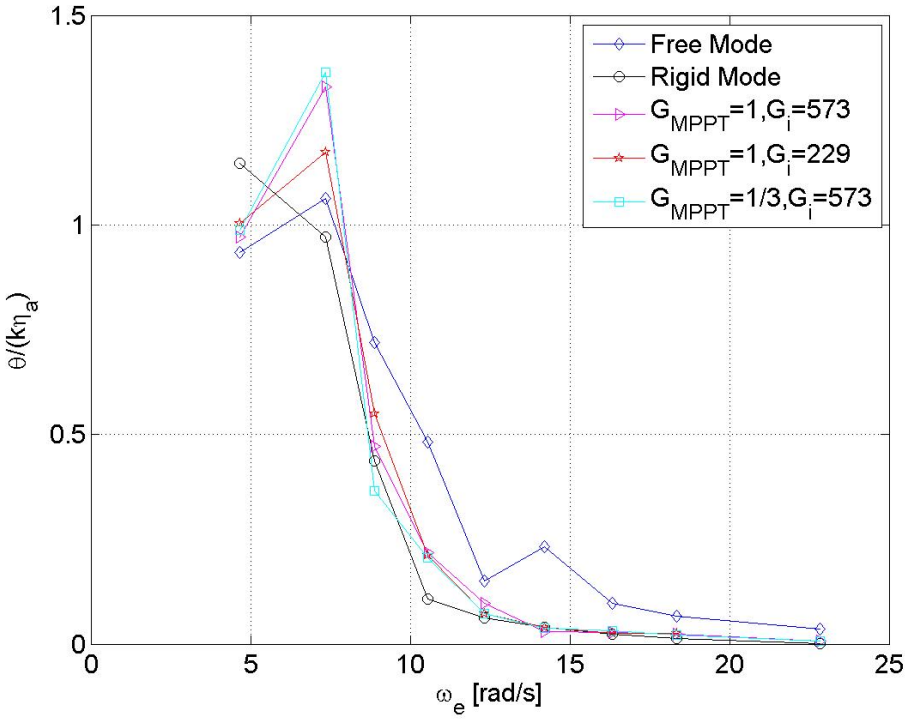

(b) Pitch of the hulls

Figure 4.11: Pitch of the cabin and the hulls at the integrated mode with forward speed of $1.5\,\mathrm{m/s}$

4.2.8 Relative Displacement at Skyhook Mode, MPPT Mode and Integrated Mode

Figure 4.12 depicted a comparison of the relative displacement between the cabin and the hulls at the skyhook mode and the free mode without forward speed. Fig.4.12(a) showed that at the free mode the front two suspension units yielded larger movement than that at the rear when the encounter frequency was below 6.8 rad/s. However, after that the rear two was slightly larger than that at the front. After 8 rad/s the movement died out gradually. Fig.4.12(b) to Fig.4.12(d) demonstrated the results at the skyhook mode with the I gain reducing from 573 to 115. The peak of the relative displacement at those sub-figures was not clearly observed, especially when the I gain was as large as 573. It also told that the small the I gain the little the relative displacement, thus the motion of the cabin and the hull were more alike.

Figure 4.13 depicted a comparison of the relative displacement between the cabin and the hulls at the skyhook mode and the free mode with forward speed of 1.5 m/s. An obvious peak at the front and rear suspension units was observed around 7.5 rad/s at the free mode as shown in Fig.4.13(a). Besides a tough and a peak at the rear suspension units occurred around 11 rad/s and 14 rad/s, respectively, whereas that at the front units was not clearly observed. It suggested that around 11 rad/s the rotation center of the pitch motion was shift backward significantly. Fig.4.13(c) to Fig.4.13(d) showed the results at the skyhook mode with I gain of 573, 229 and 115, respectively. In those sub-figures, a peak of the front suspension units was observed, however, neither peaks nor troughs were identified at the rear suspension units. One may also find that the magnitude of the relative displacement at the front units was smaller when the I gain was smaller, and that at the rear units was more flat comparing to that at the free mode.

Figure 4.14 depicted a comparison of the relative displacement between the cabin and the hulls at the MPPT mode and the free mode without forward speed. Fig.4.14(b) to Fig.4.14(d) showed the results of tuning the impact factor of the MPPT mode from 3 to 1/3. It suggested that the tuning operation modified the relative displacement in a way that with a lower G_{MPPT} the relative displacement was smaller, and the tendency was more flat comparing to the one at the free mode.

Figure 4.15 depicted a comparison of the relative displacement between the cabin and the hulls at the MPPT mode and the free mode with forward speed of 1.5 m/s. The relative displacement at a MPPT mode fluctuated similar to that at the free mode, but with a smaller magnitude. Two peaks and one trough at the rear units, one peak at the front units were observed at the MPPT mode and the free mode around the same frequencies.

Figure 4.16 depicted a comparison of the relative displacement between the cabin and the hulls at the integrated mode and the free mode with forward speed of 1.5 m/s. It was seen that after 5 rad/s the relative displacement of the front units was greatly reduced at the integrated mode comparing to that at the free mode. That of the rear units at the integrated mode was varied at a small gradient along with an increment of the encounter frequency.

Relative Displacement at Skyhook Mode, $v = 0\,\mathrm{m/s}$, $\beta = 180°$

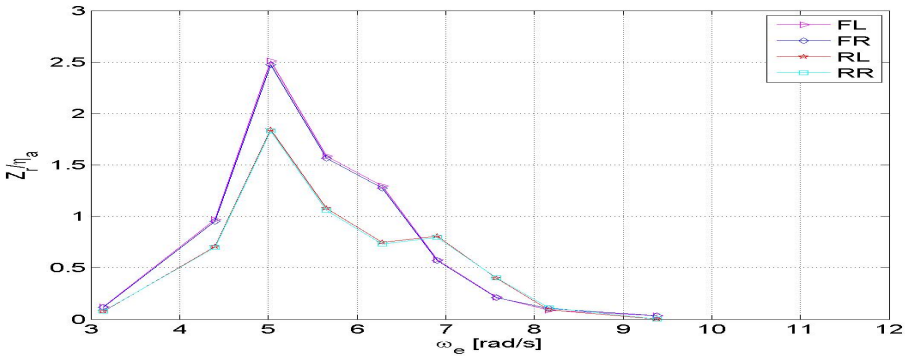

(a) Free Mode

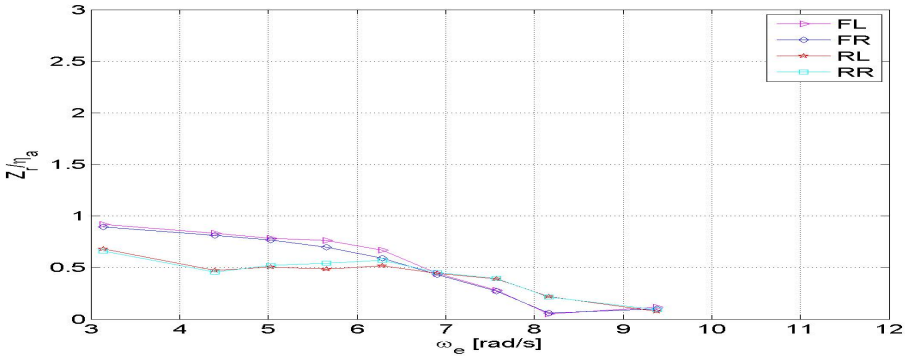

(b) Skyhook Mode with $G_i = 573$

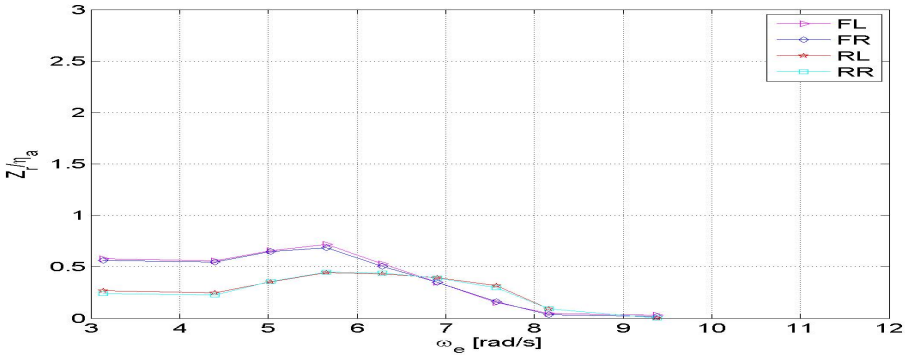

(c) Skyhook Mode with $G_i = 229$

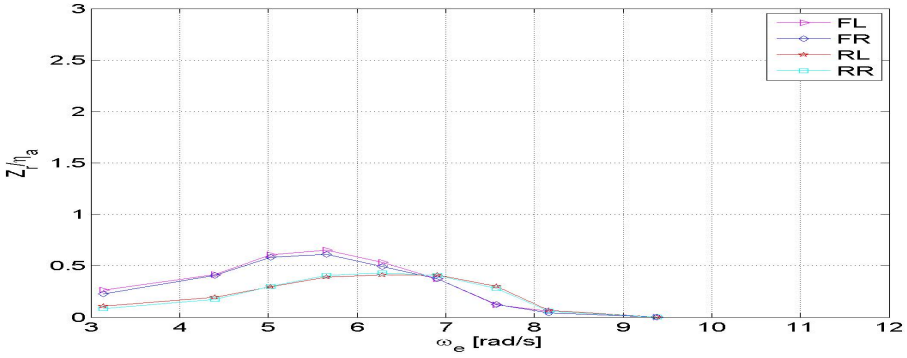

(d) Skyhook Mode with $G_i = 115$

Figure 4.12: Relative displacement at skyhook mode without forward speed

Relative Displacement at Skyhook Mode, $v = 1.5\,\mathrm{m/s}$**,** $\beta = 180°$

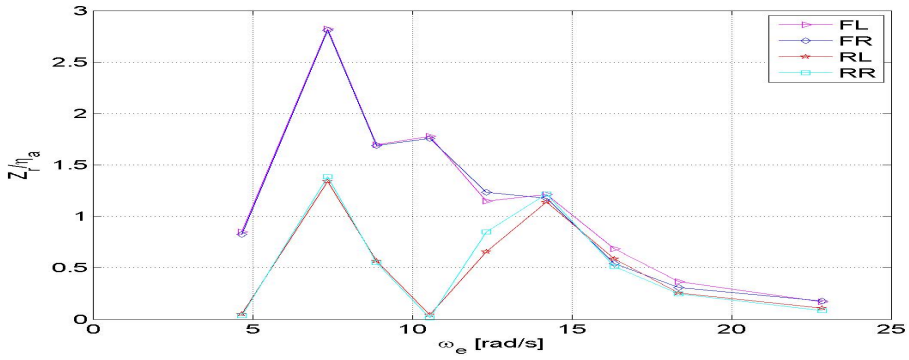

(a) Free Mode

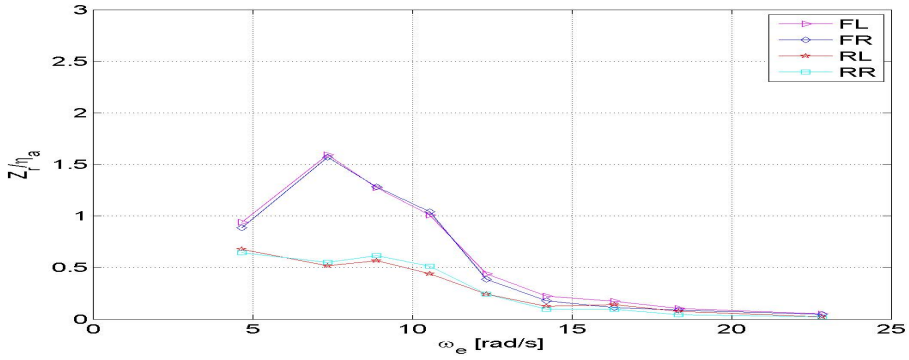

(b) Skyhook Mode with $G_i = 573$

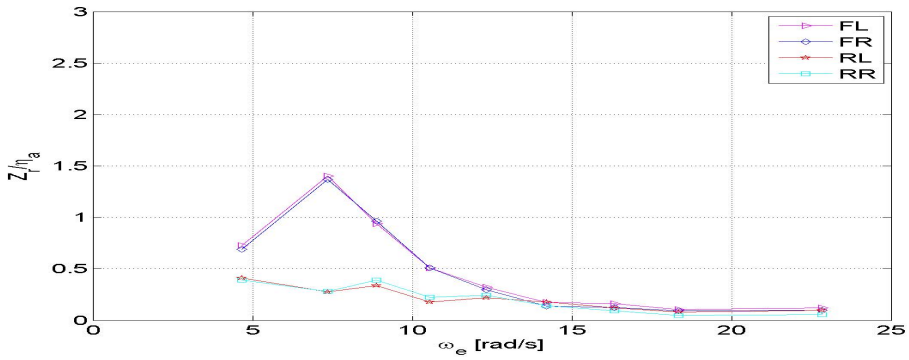

(c) Skyhook Mode with $G_i = 229$

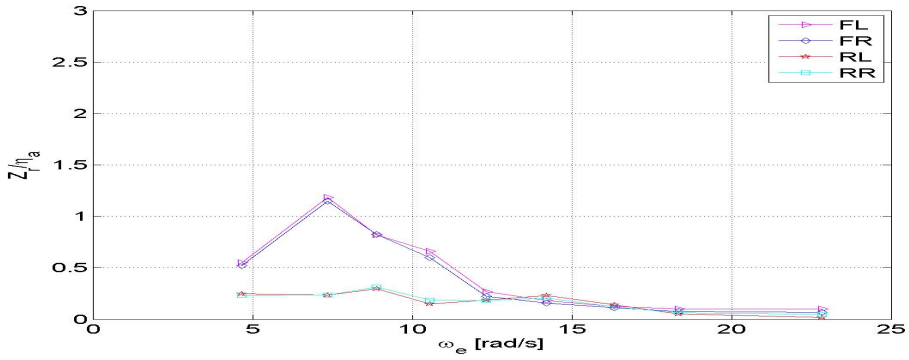

(d) Skyhook Mode with $G_i = 115$

Figure 4.13: Relative displacement at skyhook mode with forward speed of 1.5 m/s

Relative Displacement at MPPT Mode, $v = 0\,\mathrm{m/s}$, $\beta = 180°$

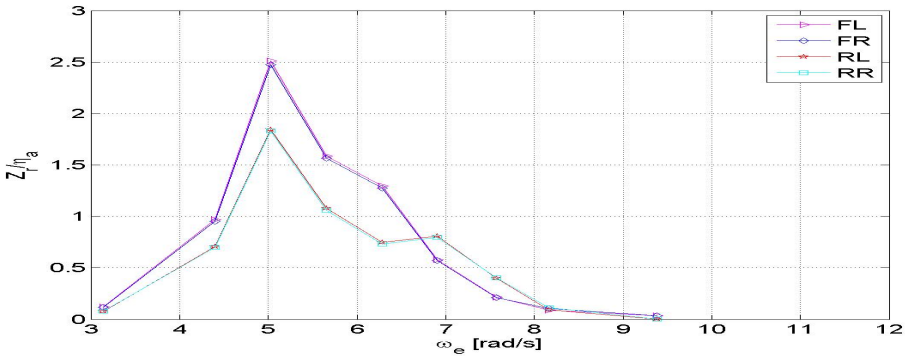

(a) Free mode

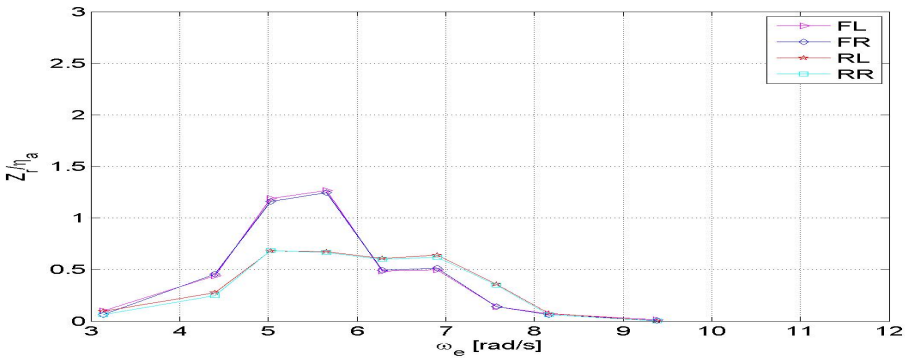

(b) MPPT mode with $G_{MPPT} = 3$

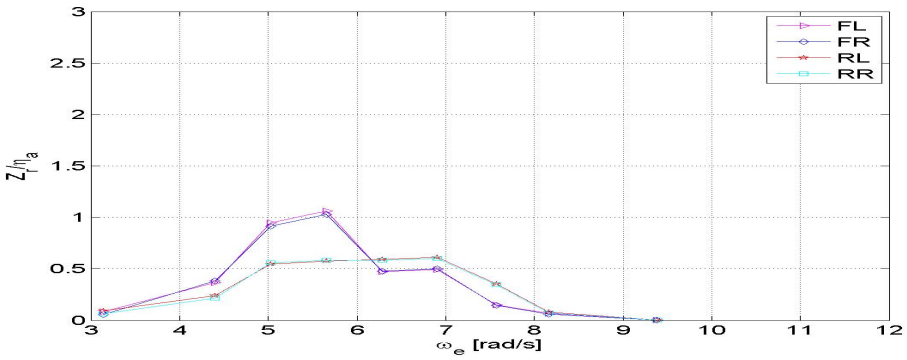

(c) MPPT mode with $G_{MPPT} = 1$

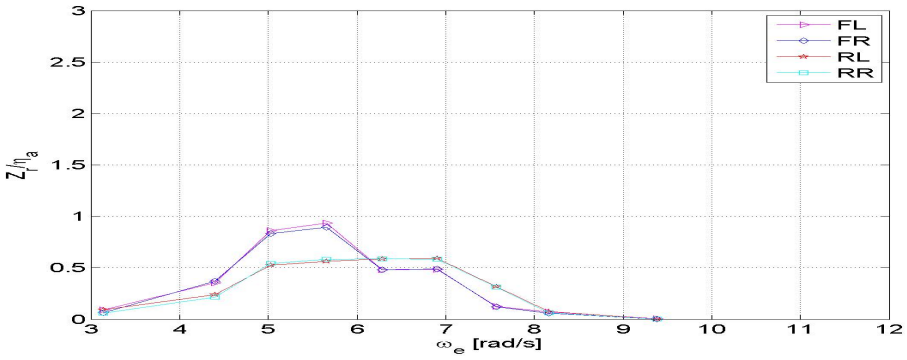

(d) MPPT mode with $G_{MPPT} = 1/3$

Figure 4.14: Relative displacement at MPPT mode without forward speed

Relative Displacement at MPPT Mode, $v = 1.5\,\mathrm{m/s}$**,** $\beta = 180°$

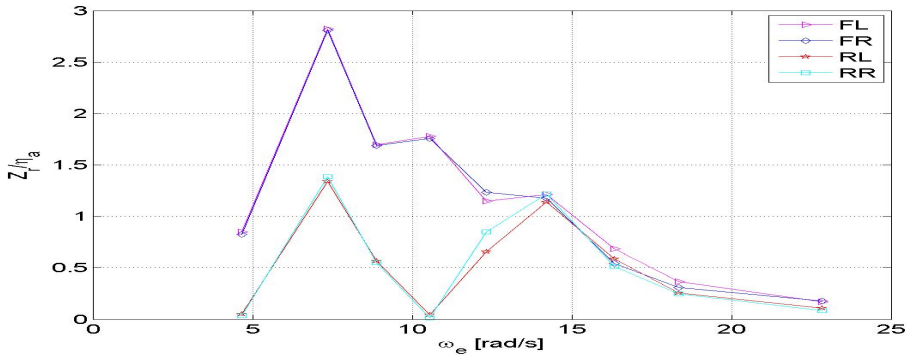

(a) Free mode

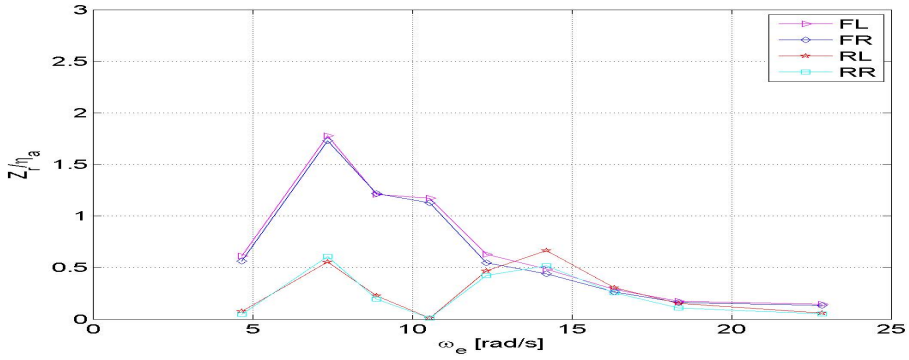

(b) MPPT mode with $G_{MPPT} = 3$

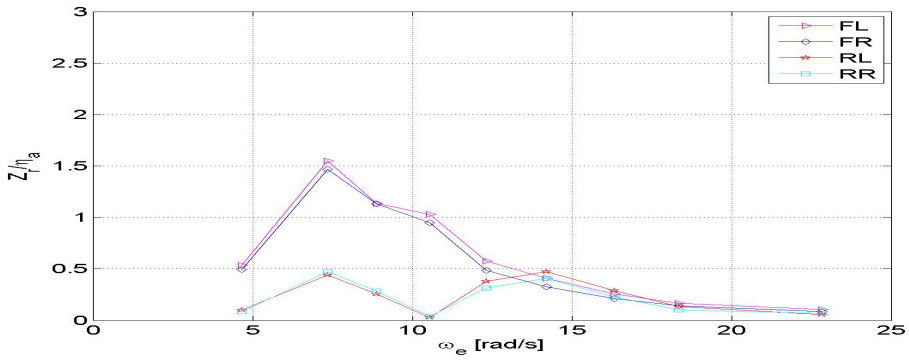

(c) MPPT mode with $G_{MPPT} = 1$

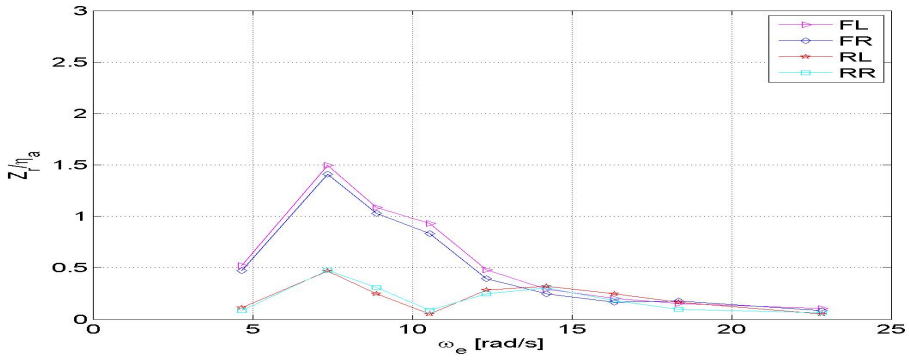

(d) MPPT mode with $G_{MPPT} = 1/3$

Figure 4.15: Relative displacement at MPPT mode with forward speed of 1.5 m/s

Relative Displacement at Integrated Mode, $v = 1.5\,\mathrm{m/s}$**,** $\beta = 180°$

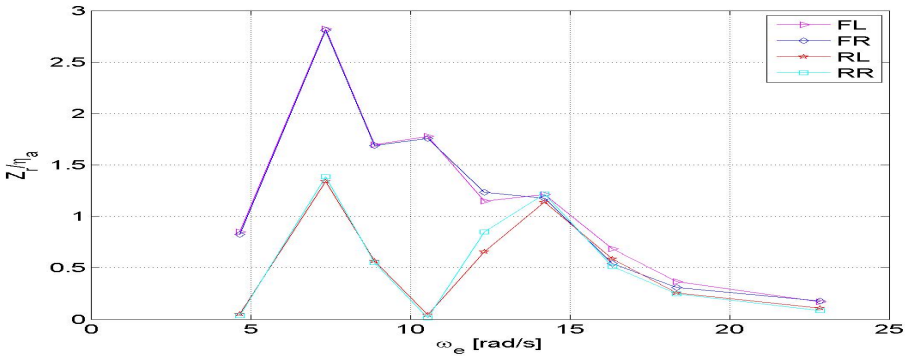

(a) Free mode

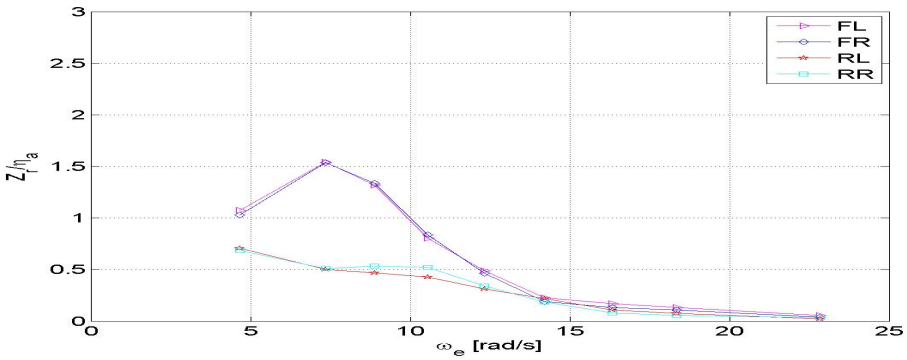

(b) MPPT mode with $G_i = 573$,$G_{MPPT} = 1$

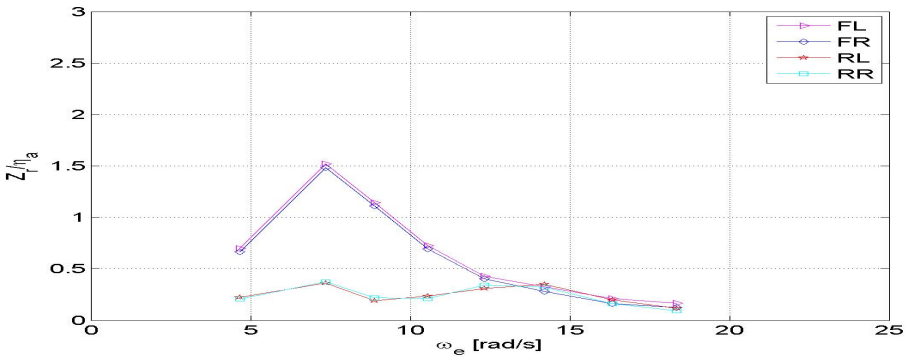

(c) MPPT mode with $G_i = 229$,$G_{MPPT} = 1$

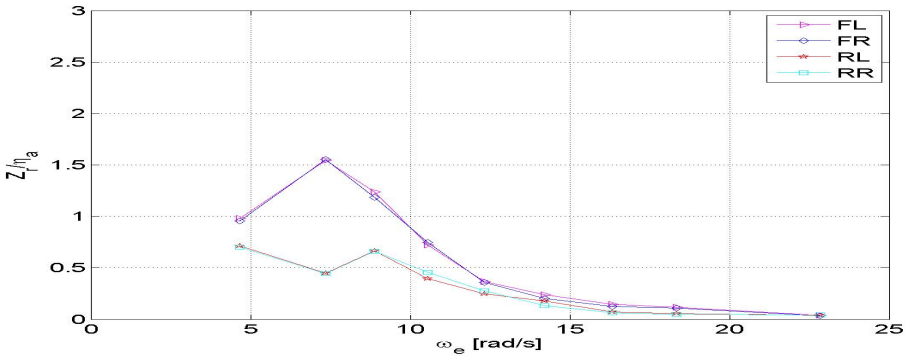

(d) MPPT mode with $G_i = 573$,$G_{MPPT} = 1/3$

Figure 4.16: Relative displacement at integrated mode with forward speed of 1.5 m/s

4.2.9 Power Production at Skyhook Mode, MPPT Mode and Integrated Mode

Figure 4.17 depicted the power production at the skyhook mode and the MPPT mode without forward speed. Recall that a negative value of the power production represents consumption, while that of positive represents harvesting. Fig.4.17(a) showed that large amount of power was consumed at the skyhook mode, which was used to suppress the oscillation of the cabin. It also told that the higher the I gain was, the more the power was consumed. A peak value of which was observed around 5 rad/s. Fig.4.17(b) demonstrated the power captured at the MPPT mode. A peak occurred around 5.8 rad/s, which was about 27%. Departing from the peak, the wave energy capture width ratio decreased sharply. Beyond the band of 4.5 rad/s to 7.5 rad/s, the ratio was reduced below 5%. It also showed that before the peak, MPPT mode with the impact factor of 3 captured the most power, whereas after, that with the impact factor of 1 harvested the most.

Figure 4.18 showed the power production at the skyhook mode, the MPPT mode and the integrated mode with forward speed of 1.5 m/s. Fig.4.18(a) showed that at the skyhook mode, with a higher I gain the power consumption was larger. The largest amount of the power needed was about 7.8 times of the power carried by the wave crest with the same width of the hulls. Fig.4.18(b) showed the power that harvested at the MPPT mode. A peak value of 82% was observed around 9 rad/s with an impact factor of 1. At other frequencies, the MPPT mode with an impact factor of 3 was more effective. Between the encounter frequency of 5.5 rad/s and 13 rad/s the wave energy capture width ratio was above 10%. Fig.4.18(c) showed the power production at the integrated mode. It was seen that the one adopted a stronger I gain of 573 consumed significant amount of power, however, by reducing the I gain to 229, the consumed power was greatly decreased accordingly. When the encounter frequency was about 9 rad/s, the power production approached approximately 0, which means the power production of the control system reached an equilibrium. After that the wave power was started to be captured. It suggested that at an integrated mode tuning the impact factor of the MPPT mode or the I gain of the skyhook mode can modify the power production of the control system effectively.

Power Production, $v = 0\,\mathrm{m/s}$, $\beta = 180°$

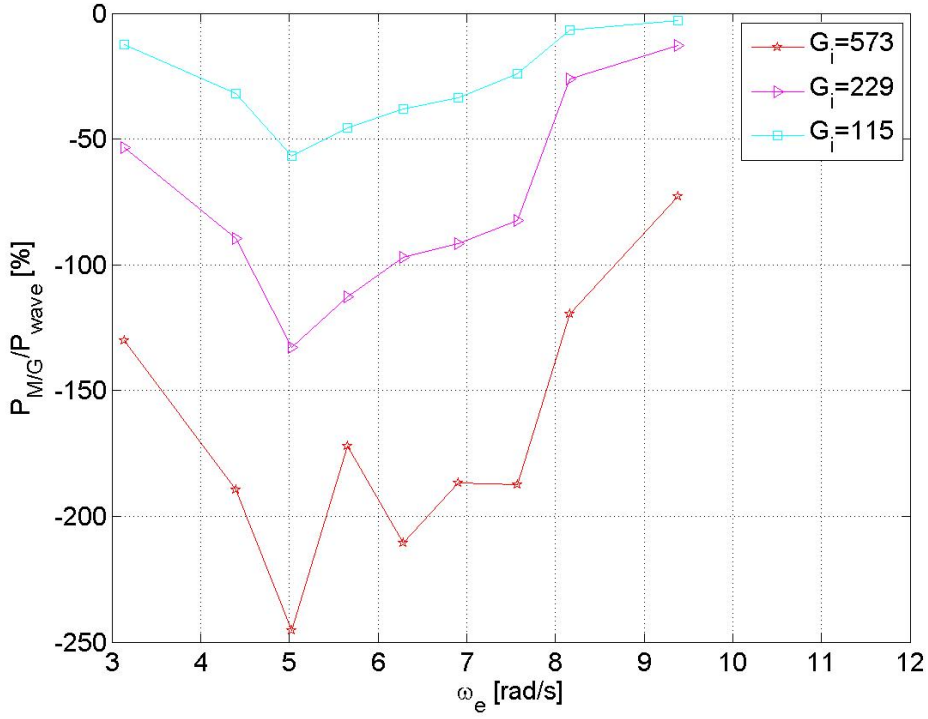

(a) Skyhook mode

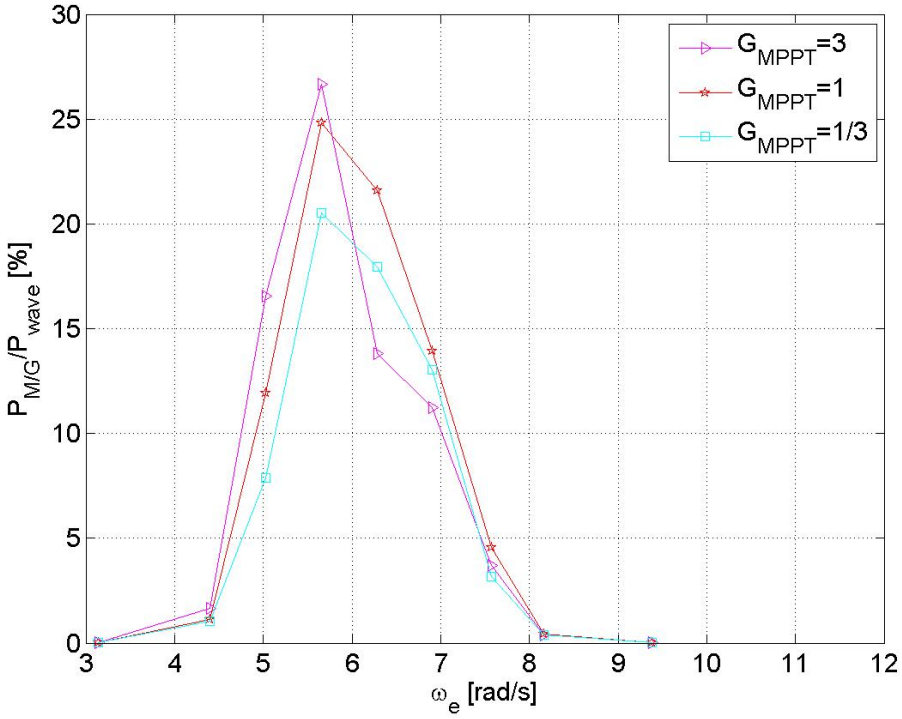

(b) MPPT mode

Figure 4.17: Power production at skyhook mode and MPPT mode without forward speed

Power Production, $v = 1.5\,\mathrm{m/s}$**,** $\beta = 180°$

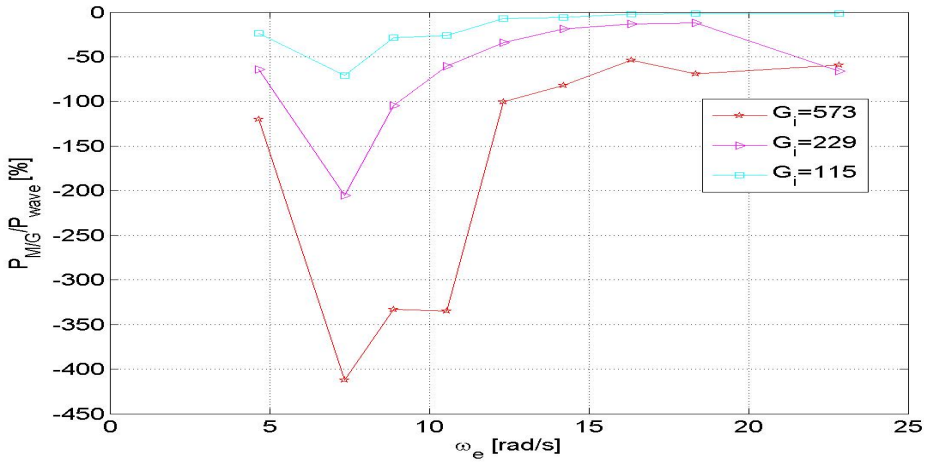

(a) Skyhook mode

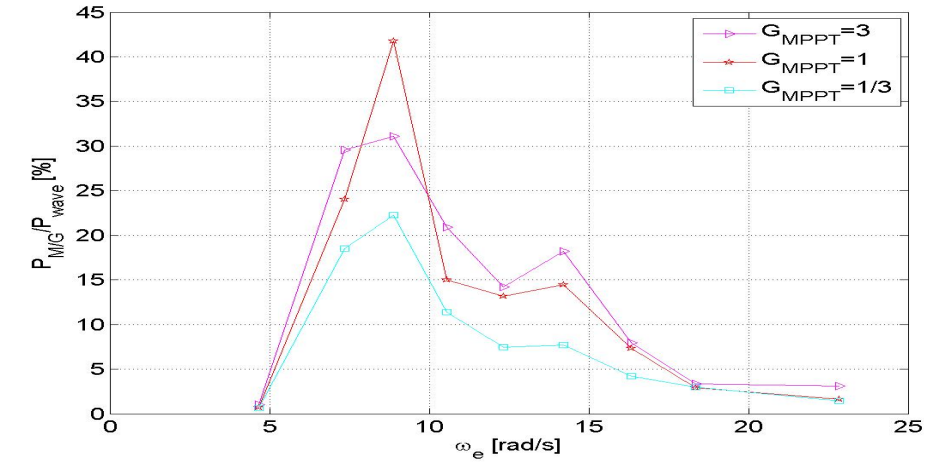

(b) MPPT mode

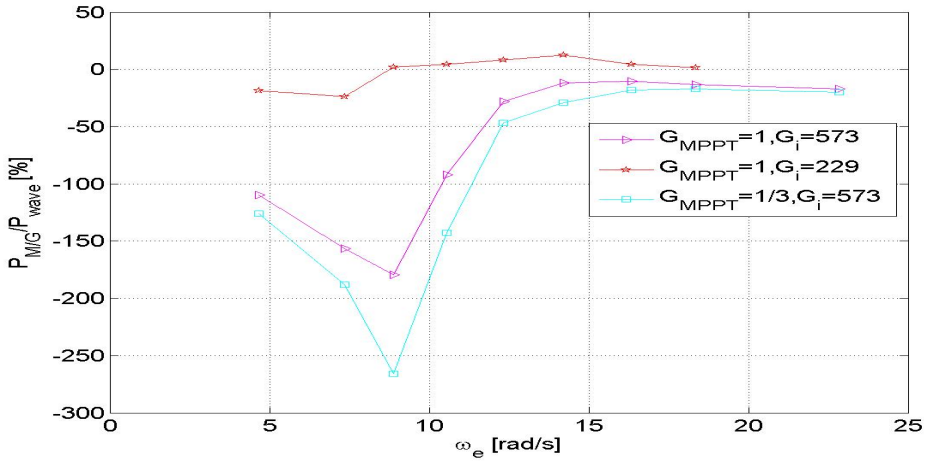

(c) Integrated mode

Figure 4.18: Power production at skyhook mode, MPPT mode and integrated mode with forward speed of 1.5 m/s

4.2.10 Beam Wave Condition

The results at beam wave conditions without forward speed were shown from Fig.4.19 to Fig.4.22. The x axis represents the angular frequency of encounter, while the y axis represents the corresponding dimensionless values.

The heave of the cabin and the hulls were given in Fig.4.19. The dimensionless heave was obtained by calculating the ratio of the magnitude of the heave to that of the incident waves.

The roll of the cabin and the hulls were given in Fig.4.20. The dimensionless roll was obtained by calculating the ratio of the amplitude of the roll to the incident wave slope.

The relative displacement between the cabin and the hulls were given in Fig.4.21. The dimensionless relative displacement was obtained by calculating the ratio of the amplitude of the relative displacement to that of the incident waves.

The power production at the skyhook mode, the MPPT mode and the integrated mode are given in Fig.4.22. The dimensionless power production was obtained by calculating the ratio of the power measured at the terminal of the M/Gs to that carried by the wave crest which has the same width as the hulls. A positive value means the power was captured, that of negative means consumed.

4.2.11 Heave Response, Pitch Response, Relative Displacement and Power Production at Skyhook Mode, MPPT Mode and Integrated Mode

Figure 4.19 showed the heave response of the cabin and the hulls without forward speed. In Fig.4.19(a), the blue-diamond line represents the free mode, a trough and a peak of the cabin were seen around 6 rad/s and 7 rad/s, respectively. That of the hulls were also observed as shown Fig.4.19(b). At the rigid mode, a trough occurred around 6 rad/s, while a peak was seen around 8 rad/s. Fig.4.19(a) also showed that when the encounter frequency was below 7.3 rad/s, the free mode generated larger heave motion of the cabin than that at the rigid mode, whereas it was reversed if the frequency was above that. Fig.4.19(b) told that below 7 rad/s, the heave of the hulls at the rigid mode was similar to that at the free mode, when it was above that the heave at the rigid mode increased significantly. Comparing the heave of the cabin at the integrated mode to that at the skyhook mode and the MPPT mode, it was found that the one at the integrated mode was smaller than that at the MPPT mode but larger than that at the skyhook mode. It implied that the integrated mode modified the heave of the cabin in such a way that it was sustained in between the one at the MPPT mode and the skyhook mode.

Figure 4.20 showed the roll response of the cabin and the hulls without forward speed. An aggressive roll motion of the cabin and the hulls were seen at the free mode when the frequency was below 4 rad/s. A peak was observed around 4.5 rad/s on both the cabin and the hulls at the rigid mode. Around the peak frequency, the skyhook mode and the integrated mode suppressed the roll of the cabin and the hulls greatly, which was below that at the rigid mode. However, at other frequencies the roll at the rigid mode was smaller. At the MPPT mode, the roll of the cabin and the hulls were larger than that at the rigid mode. Comparing to the free mode, it was found that the roll of the cabin was greatly reduced at the skyhook mode and the integrated mode, if the frequency was below 6 rad/s. Such comparisons implied that comparing to the free mode the skyhook mode eliminated the roll significantly, but comparing to the rigid mode, it was effective only around the resonance frequency.

Figure 4.21 showed the relative displacement between the cabin and the hulls without forward speed. Known that the wave propagation angle was 90°, thus the incident waves excited the starboard side of the ship before the port side. So the relative displacement at FR and RR behaved alike, which was the same to that at FL and RL. In Fig.4.19(a), a peak was observed around 7 rad/s at the free mode. From 4.5 rad/s to 6 rad/s and 7 rad/s to 9.5 rad/s, the starboard side had lager relative displacement than that at the port side, while at other frequencies, that at the port side was larger. At the skyhook mode, from 4.5 rad/s to 6.5 rad/s, the relative displacement at the port side was larger, while at other frequencies, the port side and the starboard side were alike. At the MPPT mode, the trend of the relative displacement was similar to that at the free mode, but the amplitude was smaller. While at the integrated mode, the relative displacement was similar to that at the skyhook mode, which implied that the effect of the skyhook mode was stronger than the MPPT mode.

Figure 4.22 showed the power production at beam wave conditions without forward speed. At the MPPT mode, wave power was converted into electricity since the power production was positive, a peak of which was seen around 6.5 rad/s. At the skyhook mode, a small peak of power consumption was observed around 5 rad/s, however after 7.5 rad/s it was increased dramatically. At the integrated mode, the consumed power was smaller than that at the skyhook mode. The lowest power consumption was observed around 6.5 rad/s. It was because at this frequency the MPPT component harvested the most energy which compensated that consumed by the skyhook component.

Heave Response, $v = 0\,\mathrm{m/s}$**,** $\beta = 90°$

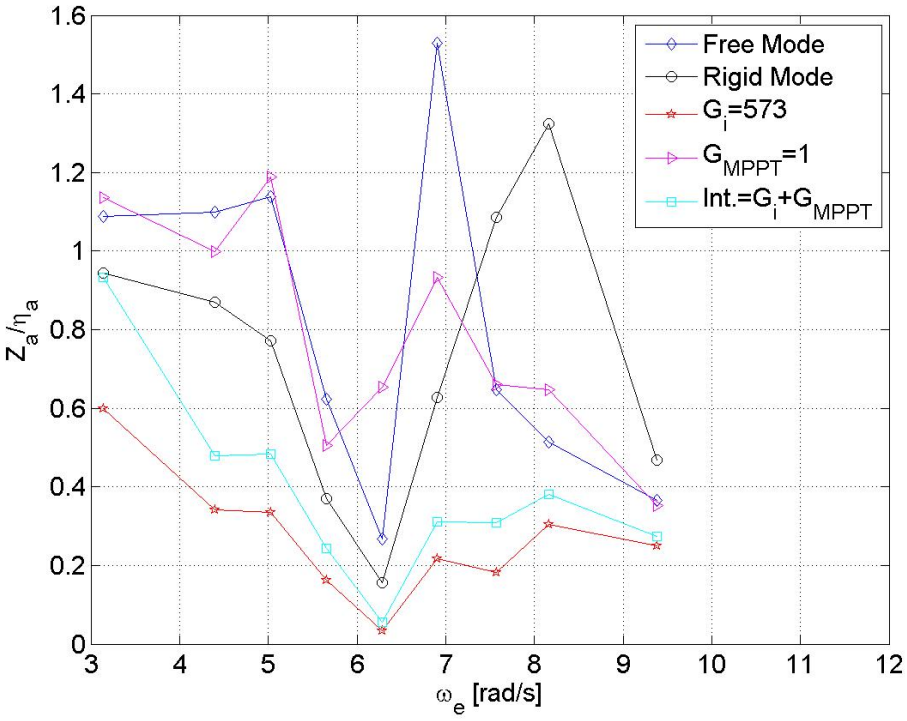

(a) Heave of the cabin

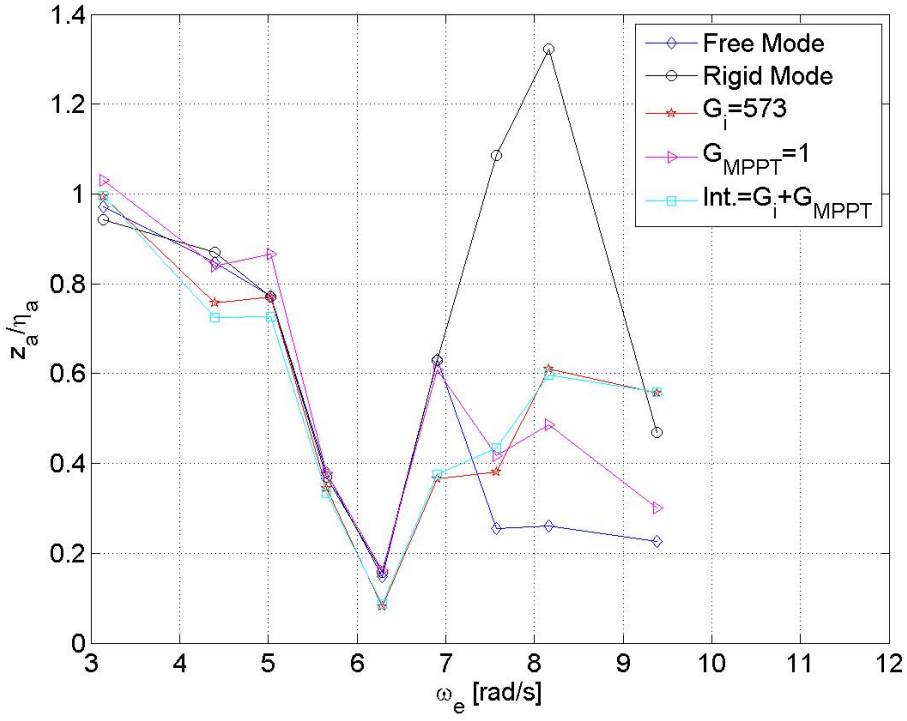

(b) Heave of the hulls

Figure 4.19: Heave response at beam wave condition without forward speed

Roll Response, $v = 0\,\mathrm{m/s}$**,** $\beta = 90°$

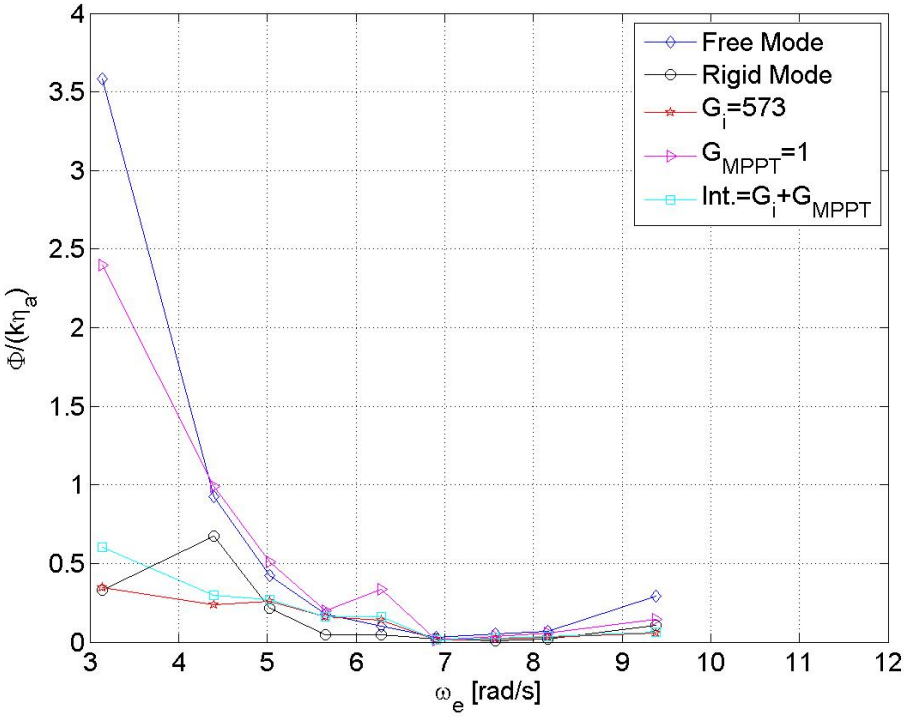

(a) Roll of the cabin

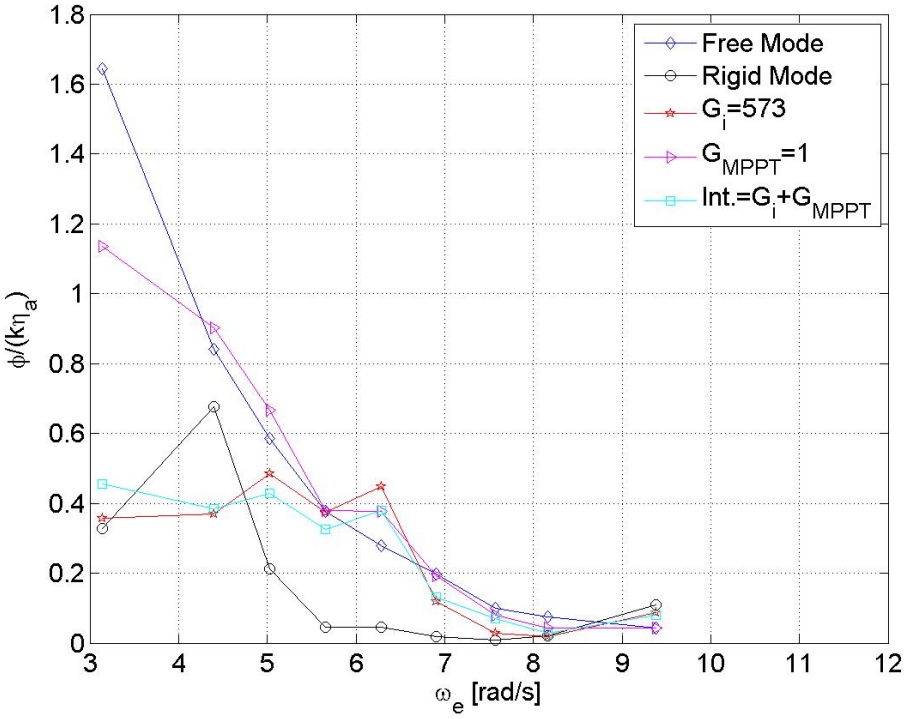

(b) Roll of the hulls

Figure 4.20: Roll response at beam wave condition without forward speed

Relative Displacement, $v = 0\,\mathrm{m/s}$**,** $\beta = 90°$

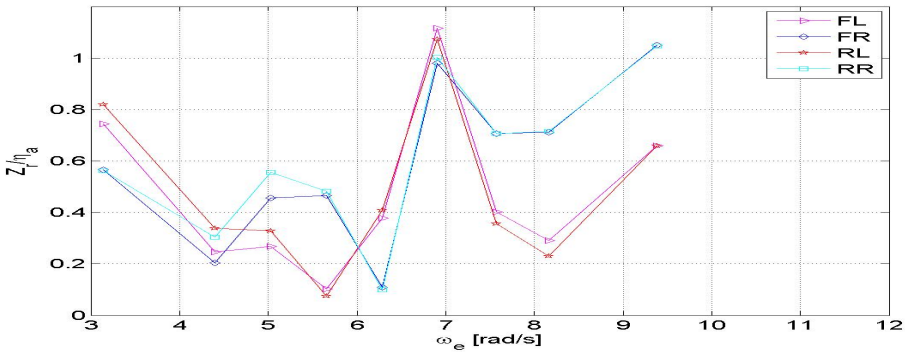

(a) Free mode

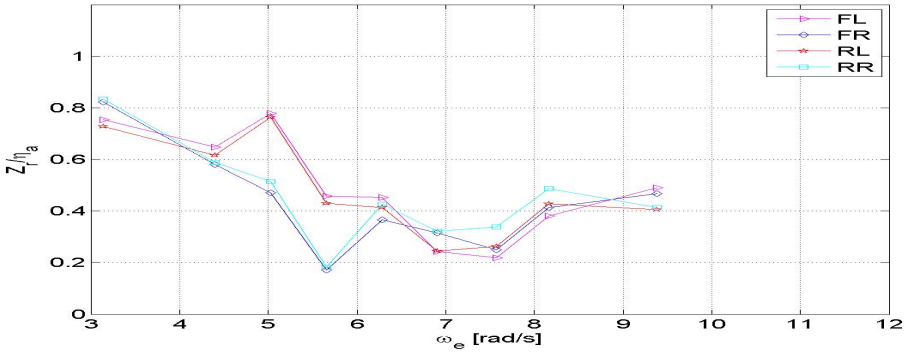

(b) Skyhook mode with $G_i = 1147$

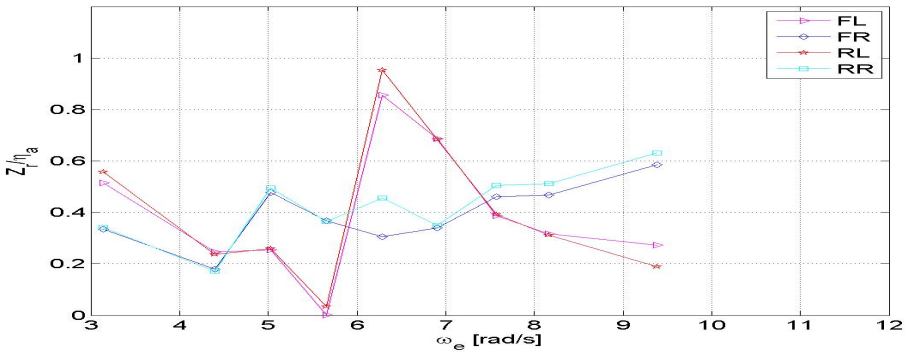

(c) MPPT mode with $G_{MPPT} = 1$

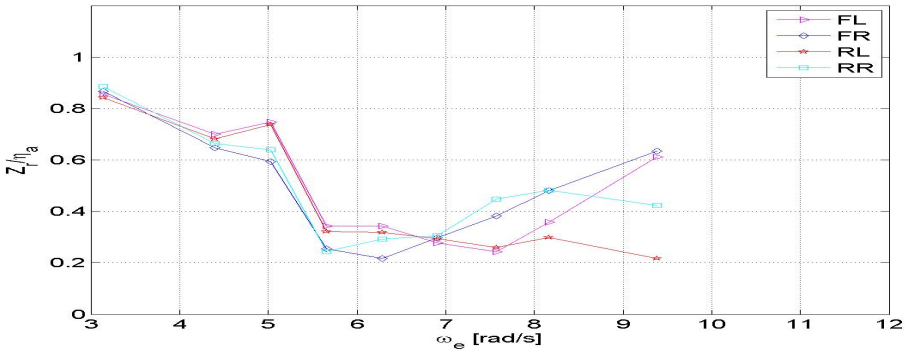

(d) Integrated mode with $G_i = 1147$, $G_{MPPT} = 1$

Figure 4.21: Relative displacement at beam wave condition without forward speed

Power Production, $v = 0\,\mathrm{m/s}$, $\beta = 90°$

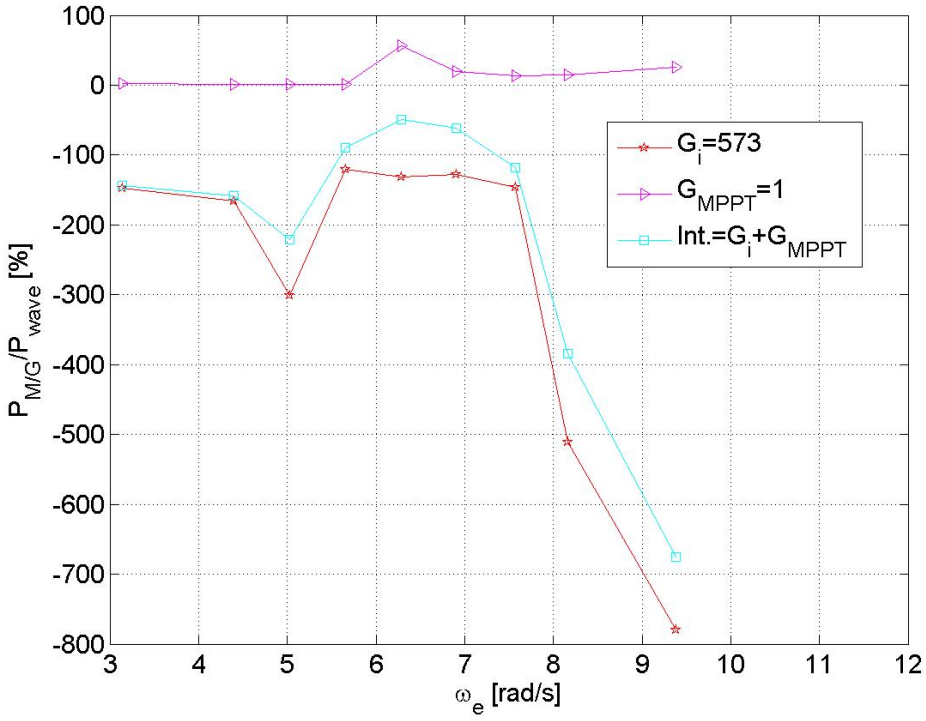

Figure 4.22: Power production at beam wave condition without forward speed

4.3 Discussion

4.3.1 Skyhook Mode

Recall that the objective of the skyhook mode is to reduce the motion of the cabin in terms of heave, pitch and roll. The experiment implemented in the towing tank suggested that with an I gain of 573, those motion of the cabin were significantly eliminated, especially around its resonance frequency, which can be seen in Fig.4.2(a), Fig.4.3(a), Fig.4.7(a), Fig.4.8(a), Fig.4.19(a) and Fig.4.20(a). However, it may be accompanied with an expense of increasing the motion of the hulls at some frequencies, as was shown in Fig.4.3(b), Fig.4.7(b), Fig.4.8(b), Fig.4.19(b) and Fig.4.20(b).

The power needed to achieve a certain level of the motion reduction had a positive relation with the magnitude of I gain. In other words, higher I gain consumed more power while the I controller was in process as can be seen in Fig.4.17(a), Fig.4.18(a) and Fig.4.22. Moreover, it was found that the peak of the relative displacement at the free mode may have a relation with that of the power consumption at the skyhook mode. With forward speed of 0 m/s, the resonance frequency of the relative displacement was observed about 5.0 rad/s in Fig.4.12(a). A peak of the power consumption was also seen around 5.0 rad/s in Fig.4.17(a). With forward speed of 1.5 m/s, a peak of the relative displacement at the free mode was about 7.5 rad/s, which was also the peak frequency of the power consumption at the skyhook mode as shown in Fig.4.18(a). However, such relation was not validated at the beam wave conditions. Fig.4.21(a) showed a peak frequency of the relative displacement around 7 rad/s, nevertheless, a peak of power consumption was observed around 5 rad/s in Fig.4.22.

4.3.2 MPPT Mode

The objective of the MPPT mode is to convert wave energy into electricity as much as possible at a given frequency. It was achieved by tuning the electronic load of the control system to match the impedance of the mechanical system, so as to get the maximum power extraction at a frequency. The impact factor of the MPPs was defined as 1. To make a comparison, two other impact factor 3 and 1/3 were also tested. Fig.4.17(b) and Fig.4.18(b) suggested that the maximum power was achieved either with an impact factor of 1 or that of 3, that with 1/3 gave the lowest power in most of the cases. As aforementioned, the MPPs for the towing tank test were suggested by a one DOF LTspice® program, which were used to give approximate values of the true MPPs for the towing tank test. The experiment results implied that the true MPPs under the towing tank condition might larger than the MPPs chosen in the test.

The heave and pitch response of the cabin at the MPPT mode were in between the free mode and the rigid mode, at some cases it was slightly smaller than that at the rigid mode as shown in Fig.4.4(a), Fig.4.5(a), Fig.4.9(a) and Fig.4.10(a). Moreover, the heave and pitch of the cabin at the MPPT mode with different impact factors behaved similar with each other, however, a significant variance of the harvested power was observed. It told that improving wave energy capture width ratio is achievable by choosing proper electronic loads at a given wave condition.

4.3.3 Integrated Mode

The objective of the integrated mode is to investigate the outcomes of the motion reduction mode combined with the wave energy capture mode, which can provide an insight into further study concerning optimization of the control system, for instance motion equilibrium, energy equilibrium, and win-win strategy of the motion reduction and energy harvesting.

Three types of combination of the skyhook mode and the MPPT mode were tested. The results suggested that when I gain was 573, the dominant component of the integrated mode was the skyhook control, if it was reduced to 229, the MPPT mode turned to be the dominant one. It can be seen from the motion response of the cabin as shown in Fig.4.6(a) and Fig.4.11(a), as well as from the perspective of the power production as shown in Fig.4.18(c). When the skyhook mode was stronger comparing to the MPPT mode, the heave and the pitch were suppressed more and large amount of power was consumed. However, if the impact factor of the MPPT mode was increased, the power consumption was reduced, until the MPPT mode was in the main position, wave power was captured and converted into electricity. It suggested that tuning either the impact factor of the MPPT mode or the I gain of the skyhook mode was an effective approach to balance the motion response of the cabin and the energy production of the control system.

Chapter 5

Energy Conversion Efficiency

5.1 General Description

Primary energy conversion efficiency plays an important role in evaluating the workability of a wave energy converter. Researches have been done to develop an efficiency assessment method [35], or to investigate an improvement approach [36]. In this chapter, the **primary energy conversion efficiency** is defined as the ratio of the input energy to the incident wave energy, while the **secondary energy conversion efficiency** is given by the ratio of the captured energy to the input energy.

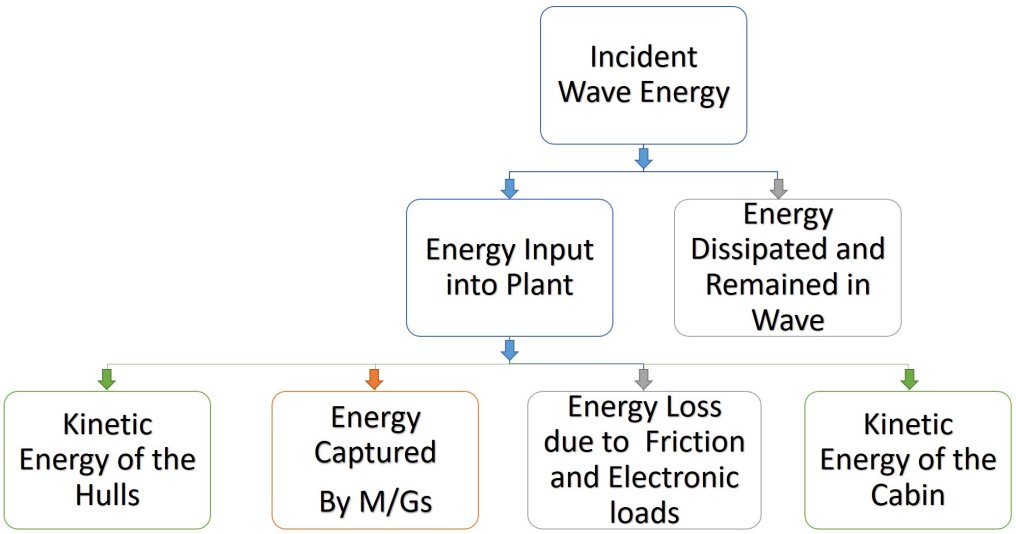

Figure 5.1: Energy flow and distribution

At the MPPT mode, the ship was acting as a wave energy converter. Incident waves excited the hulls, which leaded to a relative displacement between the cabin and the hulls. Such movement drove the M/Gs rotates, hereby converted kinetic energy into electrical energy. The energy flow and distribution was depicted in Fig.5.1. The input energy E_{in} from the incident waves to the ship can be divided into four components: the kinetic energy of the cabin E_{cb} and that of the hulls E_{hl}, the energy captured by the M/Gs E_{MG}, and the energy dissipated by friction and the electronic loads E_{cf}. Hereby, the input energy can be approximately expressed as

$$\boxed{E_{in} = E_{hl} + E_{cb} + E_{MG} + E_{cf}} \tag{5.1}$$

in which, the kinetic energy of the hulls can be represented as the work done by the waves to produce heave and pitch motion of the hulls, which is obtained by

$$E_{hl} = E_z + E_\theta \tag{5.2}$$

$$= \frac{4}{\pi^2}(z_a \cdot e_3 + \theta_a \cdot e_5) \tag{5.3}$$

where, e_3 and e_5 represents the amplitude of the wave exciting force in heave and that of the exciting moment in pitch, receptively. They were obtained by a diffraction test, the dimensionless result and the corresponding phase were given in Fig.5.2 and Fig.5.3, respectively.

The kinetic energy of the cabin was regarded as a sum of a heave components E_Z and a pitch components E_Θ, which was estimated by

$$E_{cb} = E_Z + E_\Theta \tag{5.4}$$

$$= \frac{1}{2}M(\frac{2}{\pi}\omega Z_a)^2 + \frac{1}{2}I(\frac{2}{\pi}\omega\Theta_a)^2 \tag{5.5}$$

$$= \frac{2}{\pi^2} \cdot \omega^2 \cdot (M \cdot Z_a^2 + I \cdot \Theta_a^2) \tag{5.6}$$

The wave energy carried by the crest with a width as same as the hulls can be given as

$$E_w = 2B \cdot \frac{g^2\rho}{32\pi} \cdot H^2 \tag{5.7}$$

Known the fact that the energy dissipated by friction was non-linear and the proposed accuracy of the approach to estimate its magnitude was low beyond the cabin's natural frequency, therefore, it was not taken into account in the following discussion. Hence, the primary and secondary energy conversion efficiency at one period were defined as

$$\eta_1 = \frac{E_{M/G}}{E_{in}} \cdot 100\% = \frac{E_{M/G}}{E_{cb} + E_{hl} + E_{M/G}} \cdot 100\% \tag{5.8}$$

$$\eta_2 = \frac{E_{cb} + E_{hl} + E_{M/G}}{E_w} \cdot 100\% \tag{5.9}$$

It is readily to know that the product of the primary and secondary efficiency gives the wave energy capture width ratio. Note that if the denominator and numerator in the above equations were divided by its corresponding period simultaneously, the conversion efficiency does not change. Therefore, in the following discussion, the time averaged energy was used.

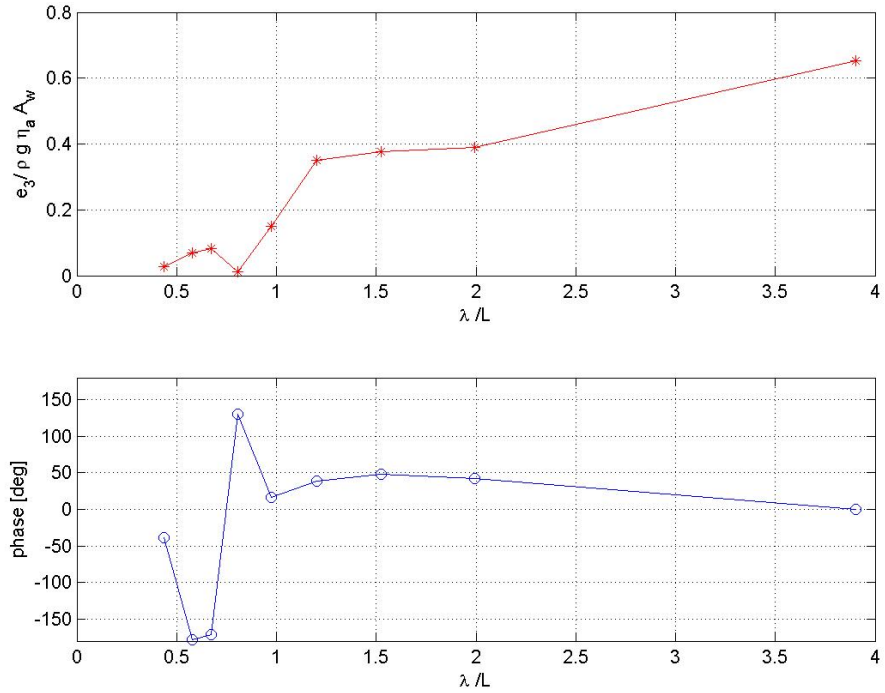

(a) $v = 0\,\mathrm{m/s}$

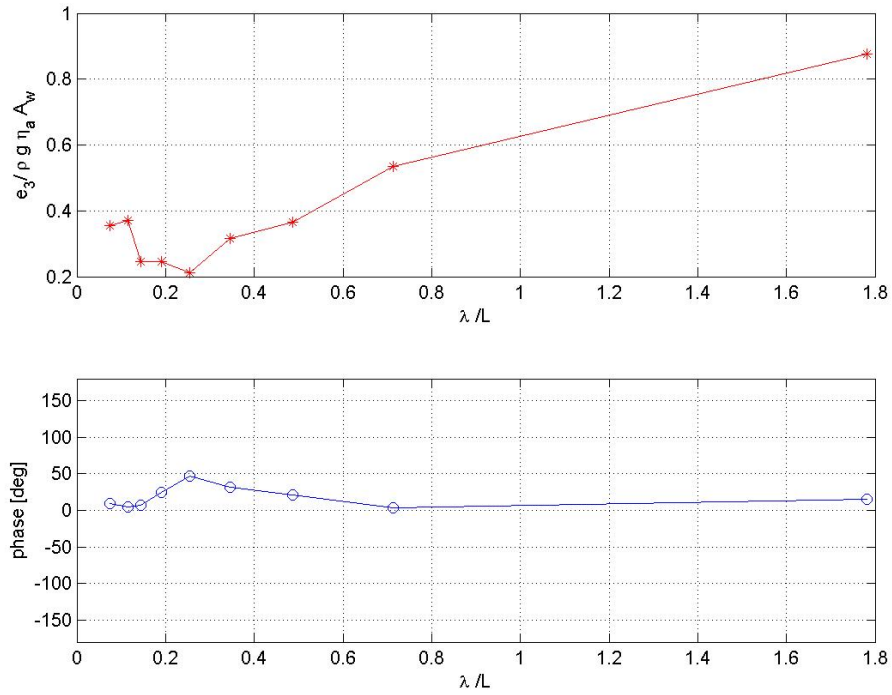

(b) $v = 1.5\,\mathrm{m/s}, Fn = 0.38$

Figure 5.2: Wave exciting force in heave

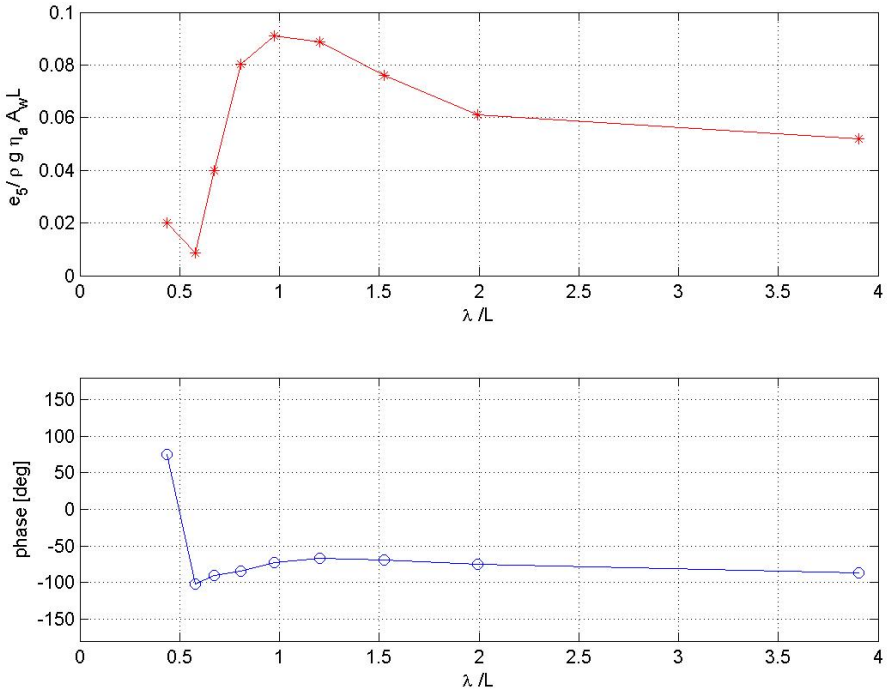

(a) $v = 0\,\mathrm{m/s}$

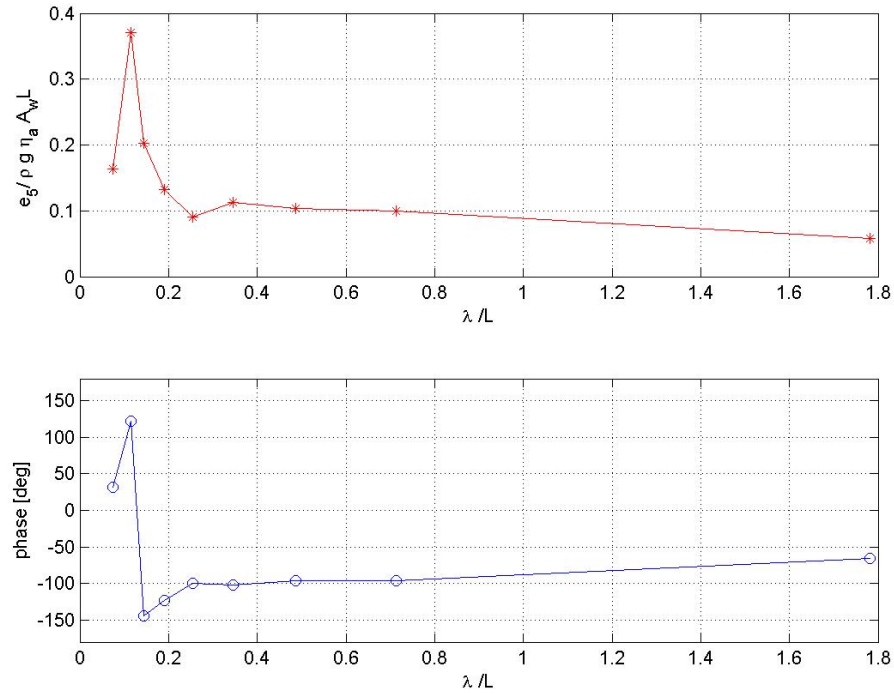

(b) $v = 1.5\,\mathrm{m/s}, Fn = 0.38$

Figure 5.3: Wave exciting moment in pitch

5.2 The Primary and Secondary Energy Conversion Efficiency

The results of the primary and secondary energy conversion efficiency were showed in Fig.5.4 and 5.5.

Figure 5.4(a) depicted the primary energy conversion efficiency with forward speed of 0 m/s. In which, the highest input power was observed at the $G_{MPPT} = 3$ with a peak of 74% around 5.7 rad/s. At the rigid mode, the peaks were seen around 7 rad/s with a highest value of 71%. The efficiency at the free mode was smaller than other modes in most of the frequencies, whose peak was 54% as observed around 5 rad/s.

Figure 5.4(b) depicted the secondary energy conversion efficiency with forward speed of 0 m/s. Peaks of the efficiency were observed around 6.5 rad/s. When the impact factor was 1 the peak reached to 48%, while that of 3 and 1/3 were about 44%. Apart from the peak frequency, the efficiency decayed rapidly. When the encounter frequency was below 5.5 rad/s, $G_{MPPT} = 3$ gave higher efficiency, while above that, it turned to be $G_{MPPT} = 1$. In general, $G_{MPPT} = 1/3$ showed the lowest efficiency among the three cases.

Figure 5.5(a) depicted the primary energy conversion efficiency with forward speed of 1.5 m/s. In contrast with that without forward speed, the rigid mode showed the lowest efficiency. At the MPPT mode, peaks of the efficiency exceeded 100% were observed from 6 rad/s to 10 rad/s, others peaks were seen around 14 rad/s and 18 rad/s.

Figure 5.5(b) depicted the secondary energy conversion efficiency with forward speed of 1.5 m/s. Two significant peaks around 9 rad/s and 12 rad/s were obtained, whose value was about 60%. The tendency at the three cases were alike, although the highest efficiency was observed alternatively between the impact factor of 1 and 3. That of 1/3 showed the lowest.

The product of the primary and secondary energy conversion efficiency gives the final efficiency of the MPPT mode concerning the ability of wave energy capture, which have already been shown in Fig.4.17(b) and Fig.4.18(b), respectively.

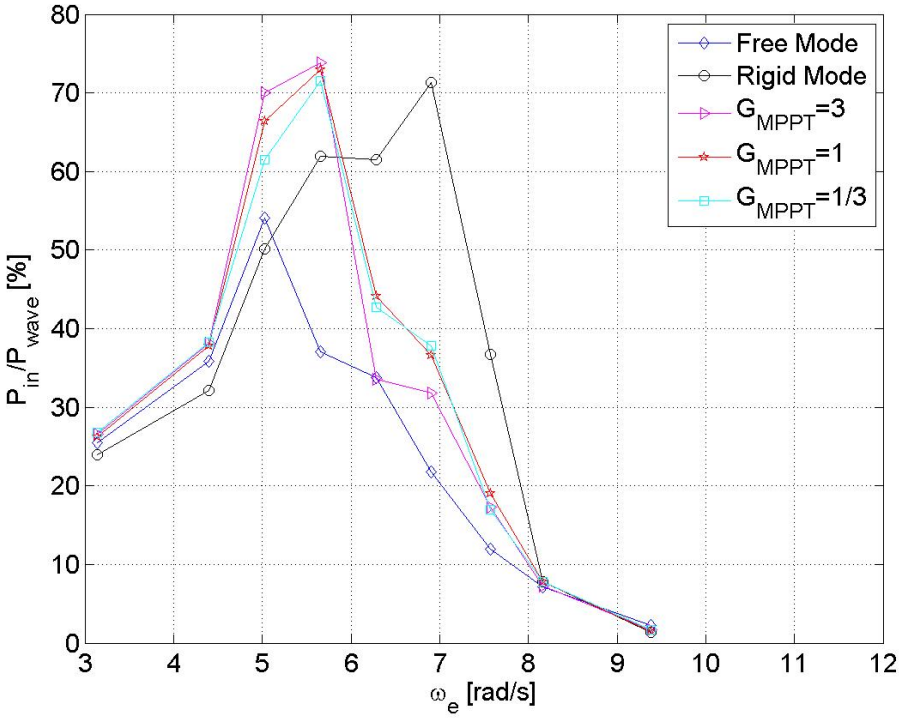

(a) Primary efficiency

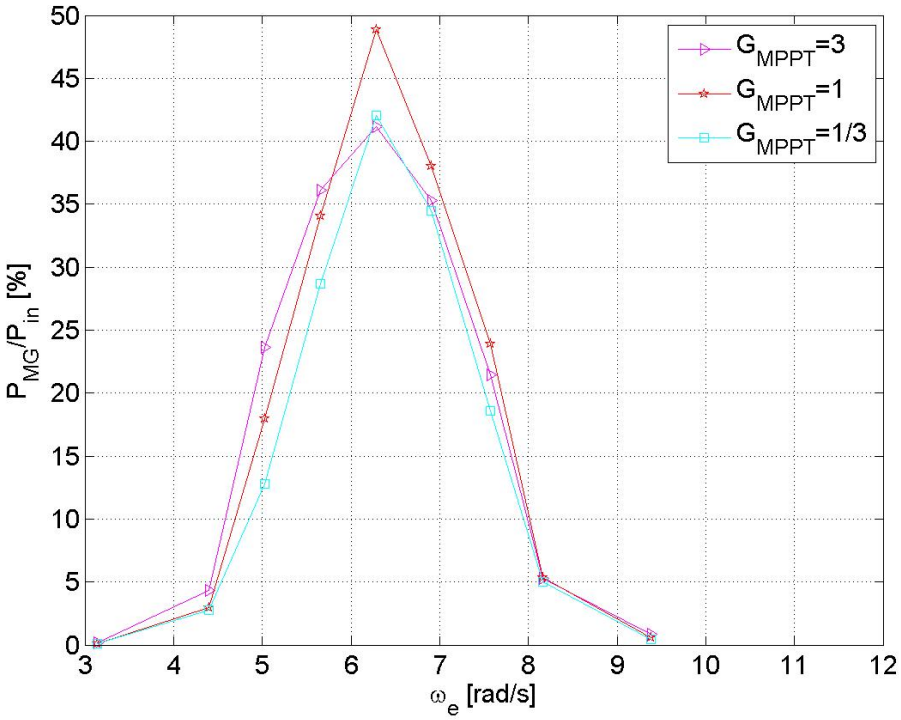

(b) Secondary efficiency

Figure 5.4: Primary and secondary energy conversation efficiency with forward speed of 0 m/s

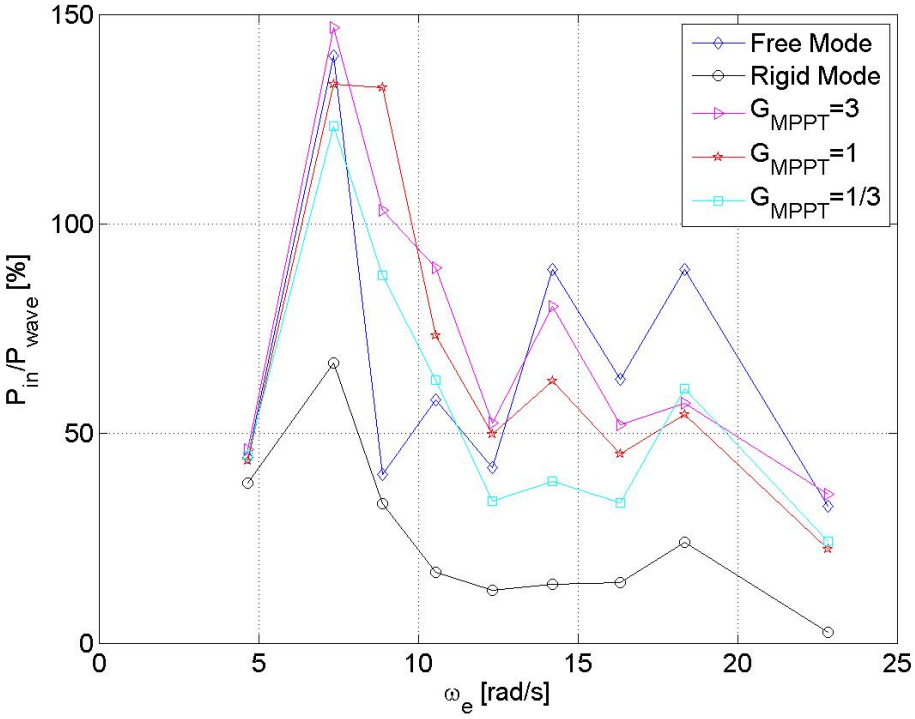

(a) Primary efficiency

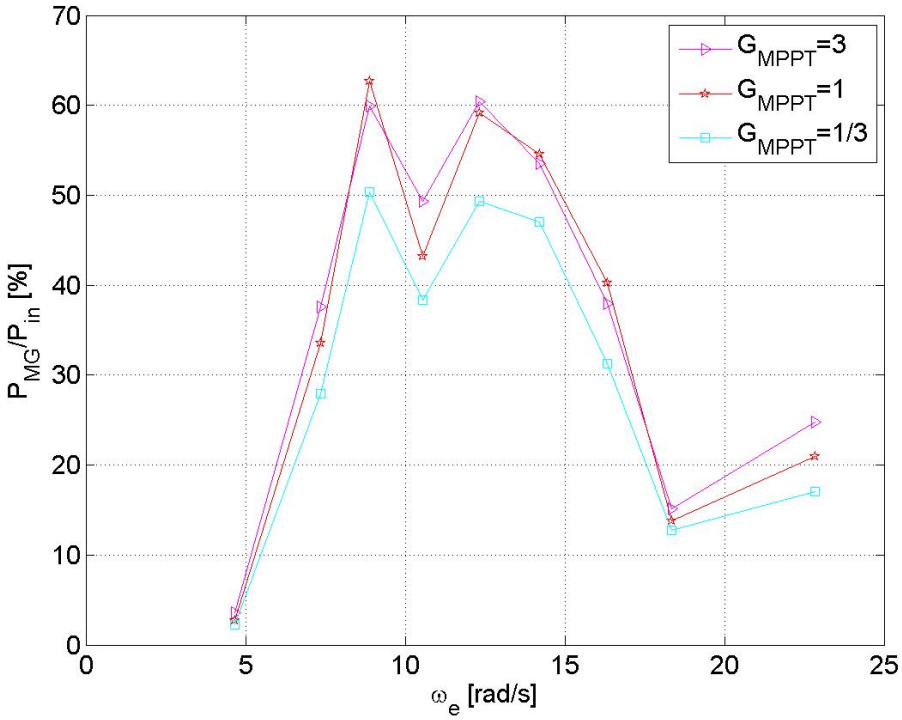

(b) Secondary efficiency

Figure 5.5: Primary and secondary energy conversation efficiency with forward speed of 1.5 m/s

5.3 Encounter Wave Power

When the ship has a non zero forward speed, it was observed that at some frequencies, the primary energy conversion efficiency exceeded 100%. It can be solved by modifying the time averaged energy carried by the water particles. The propagation velocity of the waves is proposed to be replaced by the encounter propagation velocity, which takes into consideration of the velocity of the ship. It can be written as

$$c_e = c - v \cdot cos\beta \tag{5.10}$$

in which, c is the propagation velocity of a surface wave known as $\frac{\omega}{k}$, v is the velocity of the ship, β represents the angle between the velocity of the ship and the propagation velocity of the wave. Known that the time averaged energy transport by the water partials as seen from a fixed reference system, can be written as

$$\overline{P_w} = \frac{1}{4}\rho g \eta_a^2 \left(1 + \frac{2kd}{sinh(2kd)}\right) \cdot c \tag{5.11}$$

in which, ρ is the water density, g is the accelerational gravity, η_a is amplitude of the wave, d is the water depth[37]. Instead the propagation velocity by the encounter propagation velocity, it gives

$$\overline{P_w^*} = \frac{1}{4}\rho g \eta_a^2 \left(1 + \frac{2kd}{sinh(2kd)}\right) \cdot (c - v \cdot cos\beta) \tag{5.12}$$

$$= \overline{P_w} - \frac{1}{4}\rho g \eta_a^2 \left(1 + \frac{2kd}{sinh(2kd)}\right) \cdot v \cdot cos\beta \tag{5.13}$$

In deep water condition, it can be simplified as

$$\boxed{\overline{P_w^*} = \overline{P_w} - \frac{1}{16}\rho g H^2 v \cdot cos\beta} \tag{5.14}$$

It tells that if the wave propagates in the direction of the ship moving, and the velocity of the two are the same, the energy transport of the water particles can be regarded as 0 as seen from the ship. If the direction of the two is in opposite, the energy transport of the water particles seems to be enlarged as seen from the ship, which is due to the increase of the relative velocity between the two. The time averaged energy carried per unit crest of the wave obtain by Eq.(5.14) is called **encounter wave power**.

The modified primary energy conversion efficiency and the corresponding wave energy capture width ratio were shown in Fig.5.6. It was seen that around 7 rad/s the peak primary efficiency was about 100% at the free mode, 80% $\sim$ 90% at the MPPT mode. Fig.5.6(b) showed that about 15% $\sim$ 33% of the modified wave energy can be captured at the MPPT mode while the encounter frequency located between 7 rad/s and 10 rad/s. This ratio was reduced comparing to Fig.4.18(b) was only because the modification enlarged the amount of energy transferred from the incident waves.

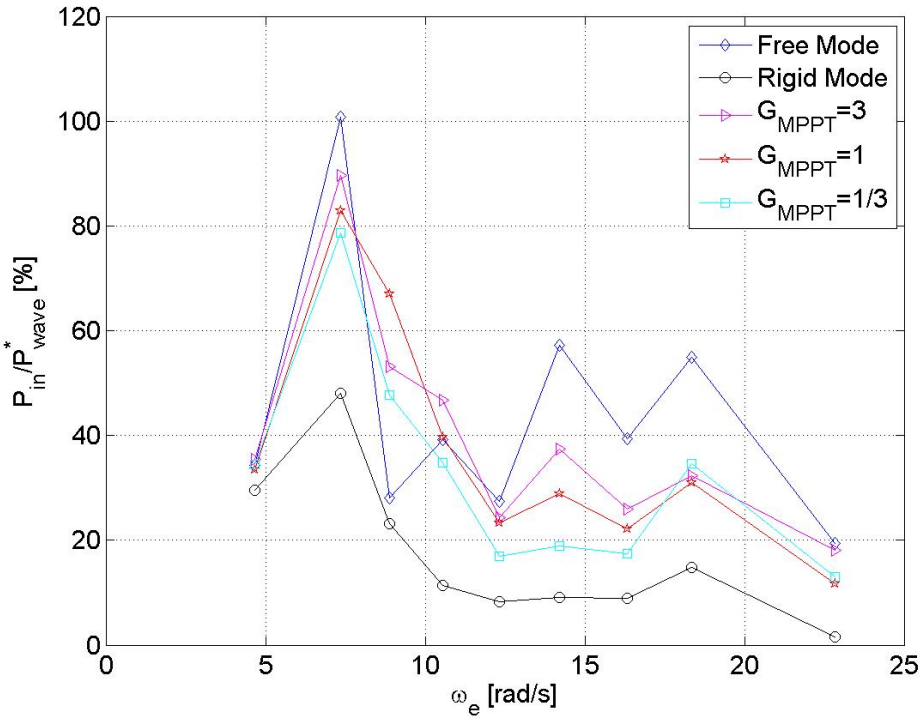

(a) Modified Primary efficiency

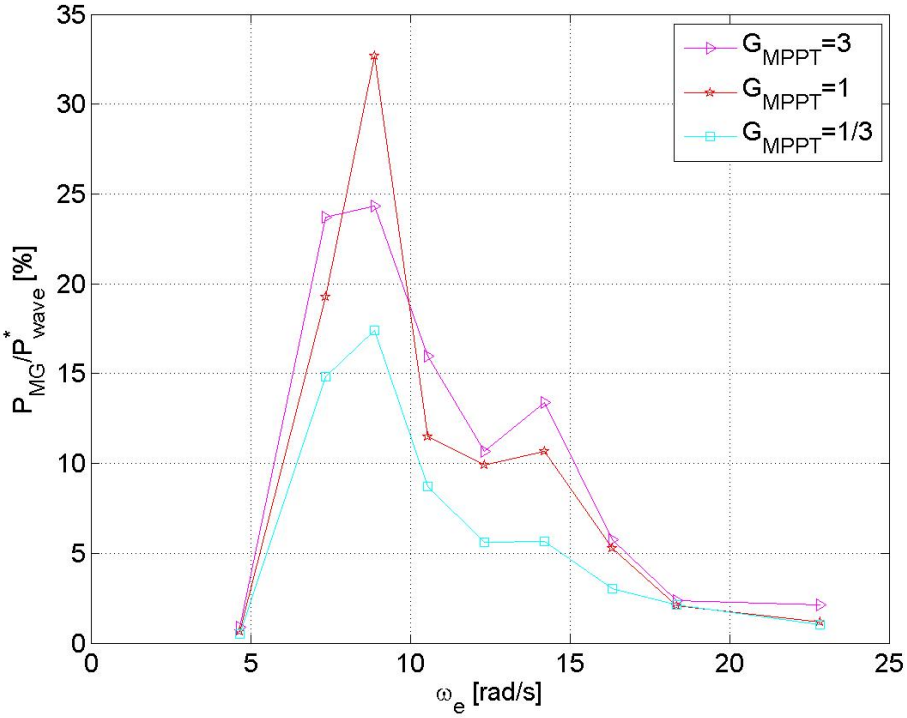

(b) Modified wave energy capture width ratio

Figure 5.6: Modified Primary energy conversation efficiency and wave energy capture width ratio with forward speed of 1.5 m/s

Chapter 6

Conclusions

A novel catamaran was proposed and developed. It equips with a suspended cabin, and has a control system to regulate the motion of the cabin. The control system consists three modes: skyhook mode, MPPT mode and integrated mode. The skyhook mode is aim to reduce the motion of the cabin so as to improve its ride comfort. The MPPT mode is applied to track the maximum power point, thus capture the wave energy as much as possible. The integrated mode is a combination of the skyhook mode and the MPPT mode, by tuning the impact factor of the MPPT mode or the I gain of the skyhook controller, a certain level of the balance the motion reduction of the cabin and the energy harvesting ability can be achieved. It was regarded as a pre-investigation of the optimization of the control system.

A model ship with length of 1.6 m was built and tested. It had four compression springs located at the four corner of the deck, namely as Front-Left, Front-Right, Rear-Left and Rear-Right, respectively. The springs were mounted between the cabin and the hulls in such a way that two sets fit on one hull which located symmetrically from the center of the buoyancy of the ship. Four brushed DC motors were employed and set on the deck above the springs, so that one motor was in charge of one control unit. One shaft of a M/G was connected to a pinion gear whose teeth meshed with that of a rack, which was vertically fixed on a hull. In this way the vertical relative displacement between the cabin and the hulls can be converted into rotational motion of the M/G, and vice versa. Supported by four modified racks, two set of Watt's link and two pantographs, the roll motion of the cabin was attainable.

At the skyhook mode, an I controller was designed to correct the motion of the cabin. The acceleration at each control unit of the cabin was detected by a G-sensor, then sent back to its corresponding I controller. The error between the processing signal and the set point was calculated, then a correcting command voltage was produced by the controller. It was applied to the M/G, accordingly torque was produced and act on the cabin and the hulls. In this way, the motion of the cabin was modified, hereby new acceleration of the cabin was generated. This loop continues until the set point of the controller was reached.

At the MPPT mode, the maximum power point was tracked until the impedance of the source and its load were matched. Electronic load of the MPPT controller were tuned at a given oscillation frequency so as to find the MPPs. The energy harvesting width ratio was investigated at those MPPs.

At the Integrated mode, both the skyhook mode and the MPPT mode were executed. The command signal from the two mode was multiplied by their impact factor, respectively. It was added up to form a new command voltage signal applied to the M/Gs.

A bench test was implemented to validate the concept of the control system. In which, the hulls were vertically oscillated by a powerful machine at a frequency range of 0.8 Hz to 1.4 Hz.

The motion response of the cabin was observed under the skyhook mode and the MPPT mode. The results indicated that the heave motion of the cabin can be obviously reduced at the skyhook mode. With an I gain of 573, more than 50% of the heave was eliminated. It also told that higher I gain contributed more in heave reduction, but consumed large amount of energy. The test at the MPPT mode, implied that the MPPs can be reasonably found by a simulation program. The function of the skyhook mode and the MPPT mode was validated.

A towing tank test was carried out under regular wave conditions, with a towing speed of 0 m/s and 1.5 m/s, respectively. The heave, pitch and roll response of the cabin as well as the hulls, the power production at the M/Gs terminal, the relative displacement between the cabin and the hulls were discussed at every control mode. That at the rigid mode and the free mode were tested so as to provide a reference system for motion reduction evaluation of the skyhook mode.

It was found that at the skyhook mode, the resonance of the cabin was greatly suppressed when the I gain was set as 573. The heave response of the cabin was reduced below 60% comparing to the incident wave amplitude, that of the pitch and the roll were eliminated more than 50% comparing to the incident wave slope. Decreasing the gain of the I controller, the motion elimination of the cabin was reduced accordingly. At head wave condition, when the forward speed was 0 m/s, the heave motion of the cabin was alike to that at the rigid mode if I gain was set as low as 115. It implied that the I controller was too weak to be effective, which can be improved by increasing its gain. At the forward speed of 1.5 m/s, motion reduction of the heave, pitch and roll of the cabin were achieved noticeably. Especially, when the I gain was as high as 573, the heave motion of the cabin was maintained below 60%, while that of the pitch was below 50%. More important, resonance of the cabin was eliminated significantly. The investigation of the motion response of the hulls implied that its motion may be increased at some frequencies, especially when a forward speed was considered. The energy input of the M/Gs suggested that to achieve a higher motion reduction of the cabin, more energy was needed.

At the MPPT mode, it was seen that the highest wave energy capture width ratio at 0 forward speed was about 27% around 5.5 rad/s, while that at 1.5 m/s was about 82% around 9 rad/s. At a given frequency, the maximum power was observed at either the case with the impact factor of 3 or that of 1, while that of 1/3 was generally the lowest. It implied that the 1 DOF simulation program provided a reasonable prediction on the MPPs, although those may not be the true MPPs of the 9 DOF model. The motion response of the cabin and the hulls were increased comparing to the rigid mode at low frequency domain, which implied that the ride comfort was scarified for wave energy harvesting purpose. However, at high frequency domain, the heave and pitch of the cabin was reduced comparing to the rigid mode, meanwhile wave energy was harvested with the CWR of $1\% \sim 5\%$.

At the integrated mode, it was observed that if the skyhook mode was in the dominating position, the motion reduction of the cabin can be achieved at a certain level, which accompanied with large amount of energy consumption. In contrast, when the MPPT mode was in the dominating position, certain amount of wave energy was captured, however, the heave of the cabin was enlarged at some frequencies comparing to that at the rigid mode. It also suggested that the motion response of the cabin and the hulls, the power production of the system were analogous to the dominating mode. It implied that along with the tuning of the impact factor of the MPPT mode and the I gain of the skyhook mode, an equilibrium state of the energy production/consumption and that of the motion reduction/increase could be found, which may further support the development of the optimization of the control system.

The highest primary energy conversion efficiency was above 70% with 0 m/s forward speed,

while that of 1.5 m/s was above 100%. The peak of the secondary energy conversion efficiency was about 48% and 63% with forward speed of 0 m/s and 1.5 m/s, respectively. The reason why the primary efficiency exceeded 100% was regarded as an underestimation of the energy carried by the incident waves. A concept, namely encounter wave power, was proposed to modify the energy carried by the wave crest as seen from the ship. It showed that after a modification, the peak of the first efficiency was about 80% $\sim$ 90%.

The research methods adopted in this study were mainly relay on the experimental investigation. During the tank test, it was found that the cabin may oscillate around a certain trim angle, specifically with the bow down and stern up slightly. It suggested that a horizontal position control of the cabin might be necessary in the future work. Moreover, simulation program with 2 or more degrees of freedom should be developed so as to provide more accurate prediction of the motion response and the power production of the system with respect to various wave conditions and control algorithms. Moreover, fail-safe strategy should be developed so as to prevent or minimize the unsafe consequences of the control system's failure.

A mature type of the Wave Harmonizer can be used in a lot of field. For instance, a high speed rescue boat which could handle large wave conditions and run fast without sacrificing ride comfort; a shuttle passenger ship which could save passenger from sea sick; an investigation boat which could provide a stable work environment for equipment and researchers, moreover, extend work period by solving energy crisis through energy harvesting mode; a maintenance ship for offshore wind farm which could provide a safe and stable connection between the wind turbines and the ship deck for equipment and personnel transportation; the suspended-cabin technique can also be used in building stable offshore platform after some modification.

Bibliography

[1] Adrean Webb, Wataru Fujimoto, Keiji Kiyomatsu, Kazuhiro Matsuda, Yasumasa Miyazawa, Sergey Varlamov, Takuji Waseda, and Jun Yoshikawa. A high-resolution, wave and current resourse assessment of japan: The gis-web-server dataset. In *3rd Asian Wave and Tidal Energy Conference*, Oct 2016.

[2] Giovanna Fargione, Domenico Tringali, and Giacomo Risitano. A fuzzy-genetic control system in the abs for the control of semi-active vehicle suspensions. *Mechatronics*, 39:89–102, 2016.

[3] Haiping Du, Kam Yim Sze, and James Lam. Semi-active control of vehicle suspension with magneto-rheological dampers. *Journal of Sound and Vibration*, 283(3-5):981–996, 2005.

[4] I.V. Ryabov, V.V. Novikov, and A.V Pozdeev. Efficiency of shock absorber in vehicle suspension. *Procedia Engineering*, 150:354–362, 2016.

[5] Xiangdong Xie and Quan Wang. Energy harvesting from a vehicle suspension system. *Energy*, 86:385–392, 2015.

[6] Yuxin Zhang, Xinjie Zhang, Min Zhan, Konghui Guo, Fuquan Zhao, and Zongwei Liu. Study on a novel hydraulic pumping regenerative suspension for vehicles. *Journal of the Franklin Institute*, 352(2):485–499, 2015.

[7] Morteza Moradi and Hamid Malekizade. Robust adaptive first–second-order sliding mode control to stabilize the uncertain fin-roll dynamic. *Ocean Engineering*, 69:18–23, 2013.

[8] Yanhua Liang, Hongzhang Jin, and Lihua Liang. Fuzzy-pid controlled lift feedback fin stabilizer. *Journal of Marine Science and Application*, 7(2):127–134, 2008.

[9] Kula Krzysztof. Cascade control system of fin stabilizers. In *19th International Conference on Method and Models In Automation and RObotics*, 2014.

[10] Reza Moaleji and Alistair R. Greig. On the development of ship anti-roll tanks. *Ocean Engineering*, 34(1):103–121, 2007.

[11] A. Souto Iglesias, L. Pérez Rojas, and R. Zamora Rodríguez. Simulation of anti-roll tanks and sloshing type problems with smoothed particle hydrodynamics. *Ocean Engineering*, 31(8-9):1169–1192, 2004.

[12] Wen-Chuan Tiao. Preliminary assessments of the anti-roll tank as a wave energy converter. *Ships and Offshore Structures*, 8(5):488–496, 2013.

[13] M.T. Sharif, G.N. Roberts, and R. Sutton. Final experimental results of full scale fin/rudder roll stabilisation sea trials. *Control Engineering Practice*, 4(3):377–384, 1996.

[14] J. van Amerongen, P.G.M. van der Klugt, and H.R. van Nauta Lemke. Rudder roll stabilization for ships. *Automatica*, 26(4):679–690, 1990.

[15] Fuat Alarçin and Kayhan Gulez. Rudder roll stabilization for fishing vessel using neural network approach. *Ocean Engineering*, 34(13):1811–1817, 2007.

[16] Velodyne Marine. Martini. `http://www.velodynemarine.com/research.html`.

[17] Nauti Craft. Nauti Craft Play-4 and Play-2. `http://www.nauti-craft.com/`.

[18] ISO2631. *Mechanical vibration and shock -Evaluation of human exposure to whole-body vibration-Part 1 : General requirements*. International Organization for Standardization, 2 edition, 1997.

[19] Anthony Lawther and Michael J. Griffin. Prediction of the incidence of motion sickness from the magnitude, frequency, and duration of vertical oscillation. *Journal of Acoustical Society of America*, 82(3):957–966, Sep 1987.

[20] M. Arima, Y. Tamura, and M. Yoshihira. Evaluation of ride comfort of passenger craft. In *2006 IEEE International Conference on Systems, Man and Cybernetics*, volume 1, pages 802–807, Oct 2006.

[21] S.H. Salter, D.C. Jeffrey, and J.R.M. Taylor. The architecture of nodding duck wave power generators. *The Naval Architect*, pages 21–21, 1976.

[22] Ross Henderson. Design, simulation, and testing of a novel hydraulic power take-off system for the pelamis wave energy converter. *Renewable Energy*, 31(2):271 – 283, 2006. Marine Energy.

[23] EMEC. Pelamis Wave Power. `http://www.emec.org.uk/about-us/wave-clients/pelamis-wave-power/`.

[24] V. Piscopo, G. Benassai, L. Cozzolino, R. Della Morte, and A. Scamardella. A new optimization procedure of heaving point absorber hydrodynamic performances. *Ocean Engineering*, 116:242 – 259, 2016.

[25] Kevin Tarrant and Craig Meskell. Investigation on parametrically excited motions of point absorbers in regular waves. *Ocean Engineering*, 111:67 – 81, 2016.

[26] N.M. Tom, M.J. Lawson, Y.H. Yu, and A.D. Wright. Development of a nearshore oscillating surge wave energy converter with variable geometry. *Renewable Energy*, 96, Part A:410 – 424, 2016.

[27] Yanji Wei, Ashkan Rafiee, Alan Henry, and Frederic Dias. Wave interaction with an oscillating wave surge converter, part i: Viscous effects. *Ocean Engineering*, 104:185 – 203, 2015.

[28] Yanji Wei, Thomas Abadie, Alan Henry, and Frederic Dias. Wave interaction with an oscillating wave surge converter. part ii: Slamming. *Ocean Engineering*, 113:319 – 334, 2016.

[29] Giovanni Malara, Alessandra Romolo, Vincenzo Fiamma, and Felice Arena. On the modelling of water column oscillations in u-owc energy harvesters. *Renewable Energy*, 101:964 – 972, 2017.

[30] Antonino Viviano, Stefania Naty, Enrico Foti, Tom Bruce, William Allsop, and Diego Vicinanza. Large-scale experiments on the behaviour of a generalised oscillating water column under random waves. *Renewable Energy*, 99:875 – 887, 2016.

[31] Chenliang Lu. A comfortable boat with suspensions absorbing wave power. Master's thesis, the University of Tokyo, 2010.

[32] Daisuke Tsukamoto. Basic research on a wave energy absorbing and motion-controlled ship. Master's thesis, the University of Tokyo, 2012.

[33] Jialin Han. Research on a new semi-active motion-controlled ship by harvesting wave energy. Master's thesis, the University of Tokyo, 2013.

[34] J.M.J Journee and W.W.Massie. *Offshore Hydromechanics*. Delft University of Technology, 2001.

[35] Yasutaka Imai, Kazutaka Toyota, Shuichi Nagata, and Mohammad A.H.Mamum. Duct extension effect on the primary conversion of a wave energy converter backward bent duct buoy. *OTEC*, 15:33–36, 2010.

[36] Yang Zhang and Yaobao Yin. Research on the primary energy conversion efficiency of pendulum wave energy converter. In *2015 International Conference on Fluid Power and Mechatronics (FPM)*, pages 633–638, Aug 2015.

[37] Leo H. Holthuijsen. *Waves in Oceanic and Coastal Waters*. Cambridge University Press, 2007.

Appendix A

Development of a Displacement Hull

A.1 Design and Build

Two displacement hulls were designed and built to meet the requirement of the mass increase of WHzer-6. The main material of the hulls is polystyrene foam, which has advantages such as low cost, light and easy to cut. The building procedure of the hulls was shown in Fig.A.1. The form of the hull was cut, modified and polished by hands. Several curve measure plates were made to check the relevancy between the design and the hulls. Finally, a water proof sheet was used to cover the surface of the hulls. The top layer of the hulls is a wooden plate, the purpose of which is to provide a solid connection with other objects fixed on it.

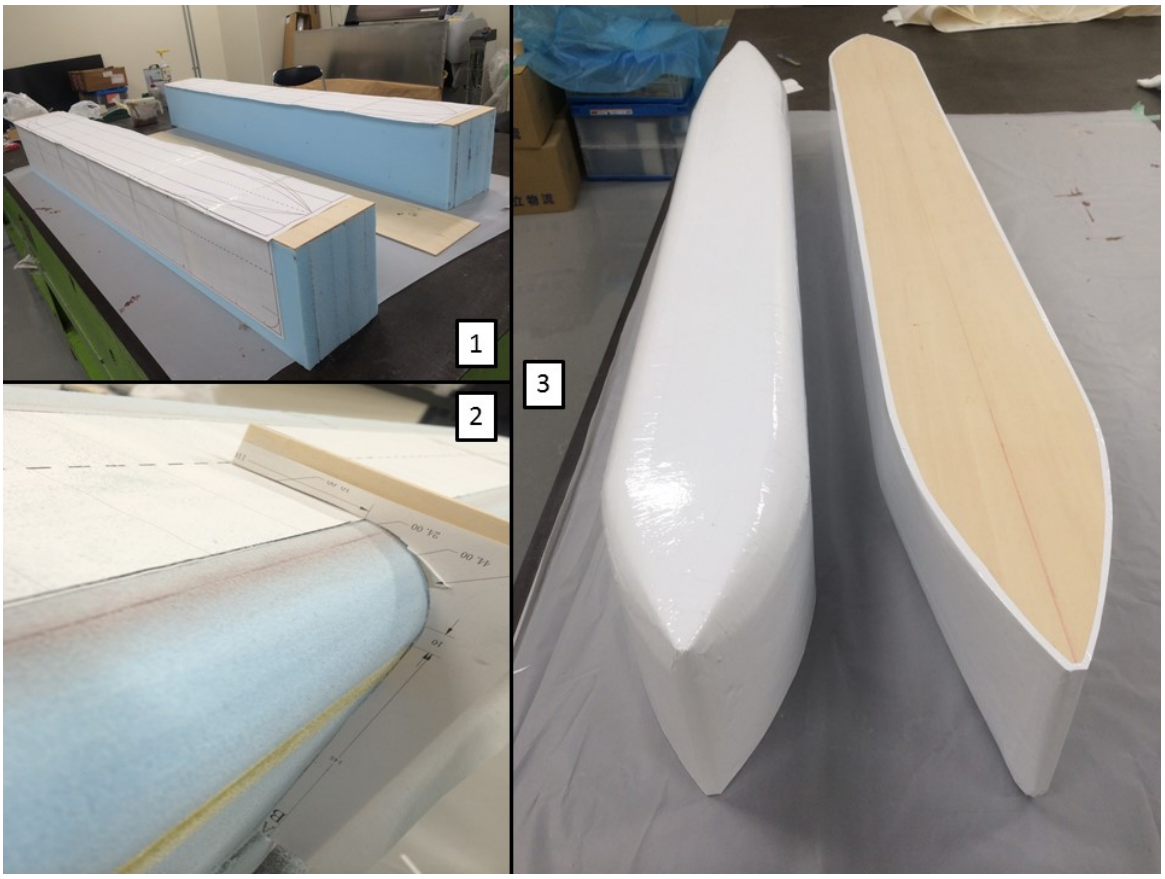

Figure A.1: Building procedure of the displacement hulls

A.2 Calculation of Hydrodynamic Coefficients

The calculation of the hydrodynamic coefficients and the wave exciting force/moment of the hulls used the method introduced by Professor Kashiwagi, namely **New Strip Method**(**NSM**).

A.2.1 General Description

According to NSM the hydrodynamic force acting on a hull, as well as the wave disturbance produced by the existing and/or motion of the hull can be estimated by the velocity potential on the surface of the hull. It can be obtained by solving

$$\frac{1}{2}\varphi_j(P) + \int_{S_H} \varphi_j(Q)\frac{\partial}{\partial n_Q}G(P;Q)ds(Q) = \begin{cases} \int_{S_H} n_j(Q)G(P;Q)ds(Q), & j = 2 \sim 4 \\ \varphi_0(P), & j = D \end{cases} \tag{A.1}$$

in which, $\varphi_j(P)$ and $\varphi_j(Q)$ represent the velocity potential at point P and Q with respect to j mode, respectively; S_H represents the submerged surface of a hull; n_Q represents the nominal vector at point Q that pointing from the hull surface to the fluid; $G(P;Q)$ represents the free-surface green function; $\varphi_0(P)$ represents the velocity potential of incident waves at point P; $j = 2 \sim 4$ represents the mode of sway, heave and roll of the hull, that of D represents diffraction mode; P represents a point in the fluid, while Q is a point on the submerged surface of a hull, however, in this equation, both of the point are on the submerged surface.

The free-surface green function is given by

$$\begin{aligned} G(x,y;\xi,\eta) = {} & \frac{1}{2\pi}log\frac{r}{r_1} - \frac{1}{\pi}\int_0^\infty \frac{kcosk(y+\eta) - Ksink(y+\eta)}{k^2+K^2}e^{-k|x-\xi|}dk \\ & + ie^{-K(y+\eta)-iK|x-\xi|} \end{aligned} \tag{A.2}$$

in which

$$r, r_1 = \sqrt{(x-\xi)^2 + (y \mp \eta)^2} \tag{A.3}$$

while, on a 2D plane, point P is represented by (x, y) and point Q by (ξ, η), K means the wave number which can be obtained from dispersion relation.

The equations are solved with respect to a 2D plane, by calculating the integral of the results along with the longitudinal direction of the hull, the hydrodynamic coefficients and the wave exciting force/moment can be obtained.

In this study, the hull was divided into 40 blocks from the stern to the bow, which consisted of 41 transverse sections. On each section, half of the submerged surface of the hull was divided into 30 segments, which hereby were composed of 31 points. The division of the hull was depicted in Fig.A.2. Typical transverse section at the stern part, middle part and bow part were shown in Fig.A.3. Known that the hull is symmetrical on the starboard side and the port side, the shape input of the hull was only the port side. In this calculation, the interaction between the two hulls was not taken into consideration, therefore, the hydrodynamic coefficients and the wave exciting force/moment was doubled to represent that of the catamaran. The specifications of one hull was given in Table A.1.

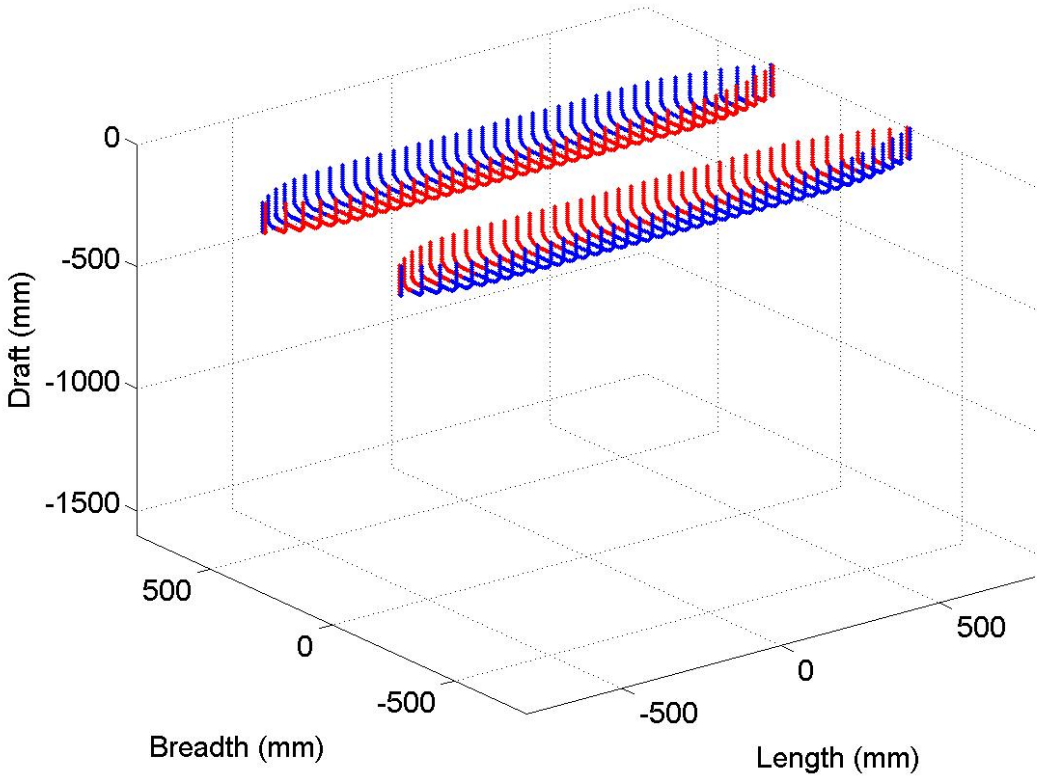

Figure A.2: Division of the hulls with 41 transverse sections

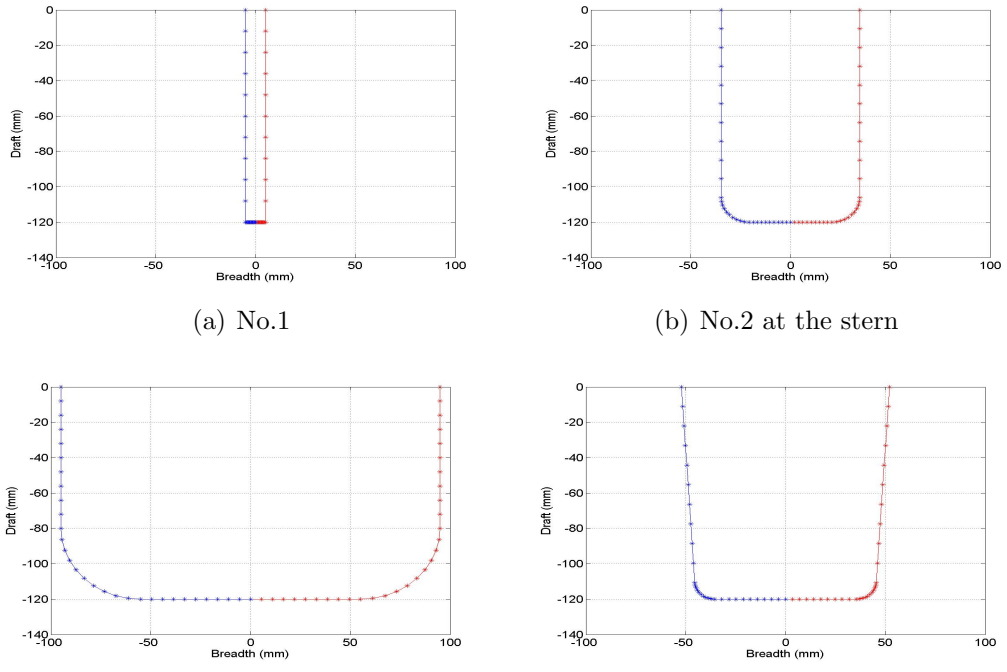

(a) No.1

(b) No.2 at the stern

(c) No.8 to No.33

(d) No.38 at the bow

Figure A.3: Typical transverse segment division with 31 points on half of the segment

Table A.1: Specifications of one hull

Symbol	**Value**	**Unit**	**Description**
L	1.600	m	Length
b	0.190	m	Breath
d	0.120	m	Draft
∇	0.031	m^3	Displacement
A_w	0.267	m^2	Water-plane area
k_{yy}	0.734	m	Gyrational radius
k_{33}	2619.6	N/m	Restoring force constant of heave
k_{53}	-48.76	N	Restoring moment on pitch due to heave at the center of gravity
k_{35}	-48.76	N	Restoring force on heave due to pitch at the center of gravity
k_{55}	447.02	Nm	Restoring moment constant of pitch at the center of gravity

A.2.2 Calculation Results

The hydrodynamic coefficients and forces concern to the heave and pitch motion were calculated, the results were given in from Fig.A.4 to Fig.A.7.

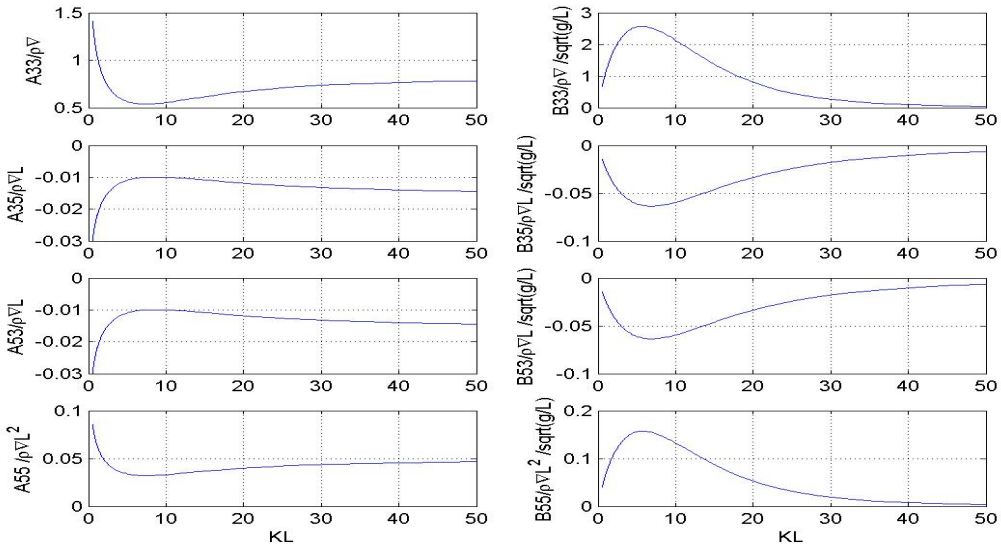

Figure A.4: Hydrodynamic coefficients without forward speed

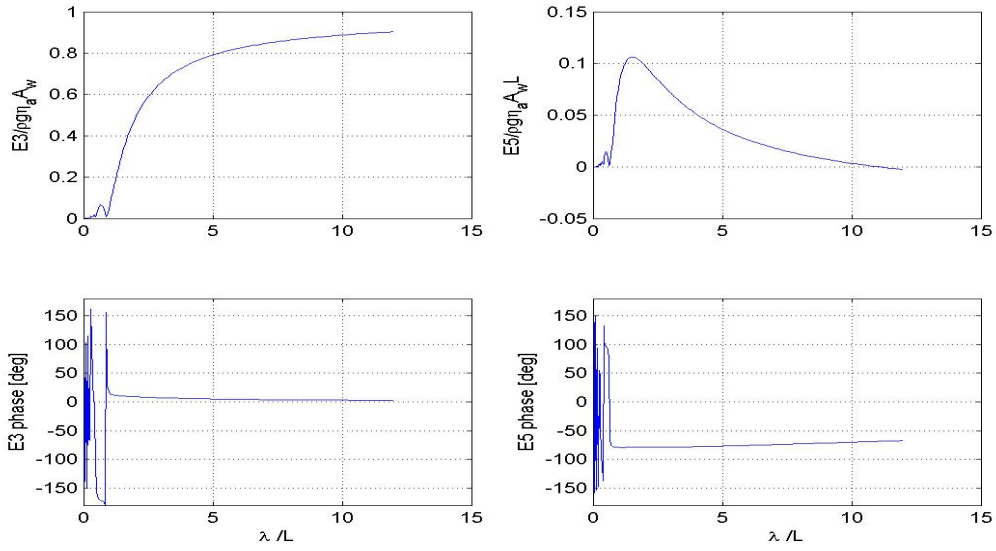

Figure A.5: Wave exciting force/moment without forward speed

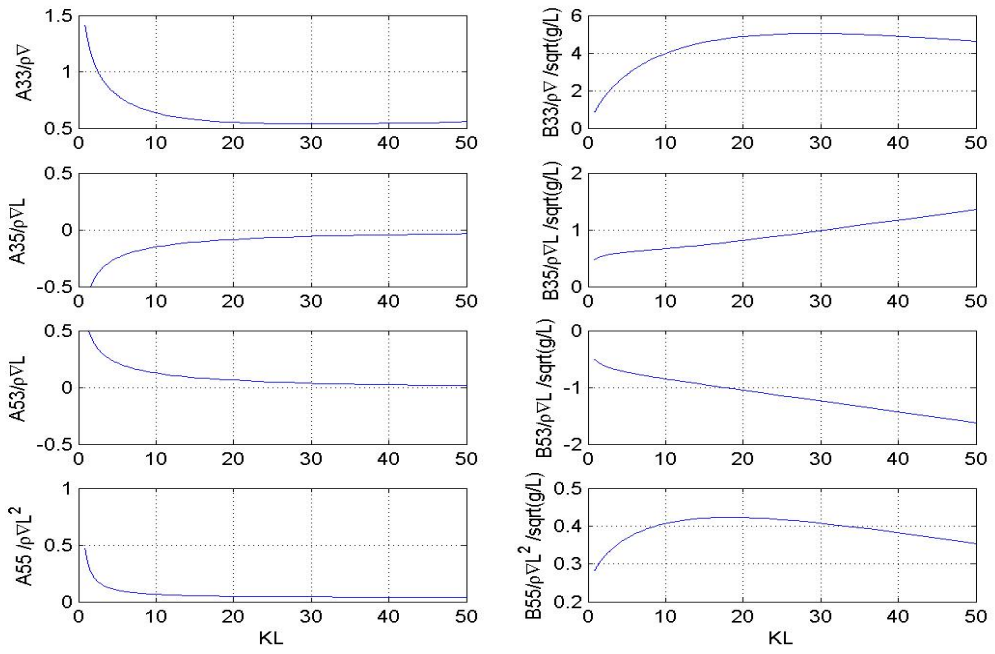

Figure A.6: Hydrodynamic coefficients with forward speed of 1.5 m/s, $Fn = 0.3786$

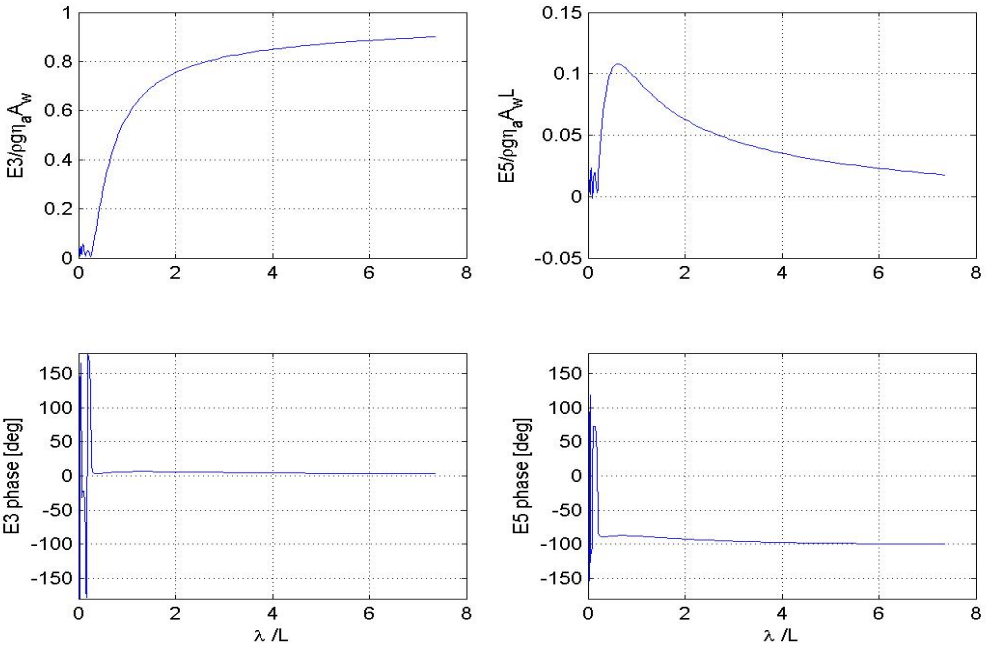

Figure A.7: Wave exciting force/moment with forward speed of 1.5 m/s, $Fn = 0.3786$

A.3 Diffraction Test

A.3.1 General Description

A diffraction test was implemented to identify the characteristics of the wave exciting force and moment with respect to various frequencies. In the test, the four suspension units were disabled, therefore formed a rigid body model. The test was done before the suspensions of WHzer-6 was finished, therefore the structure above the hulls adopted that from WHzer-4. The load cell of an oscillation machine was connected to the cabin at the point which in the vertical line of the center of gravity. The experiment setup was shown in Fig.A.8.

Figure A.8: Experimental setup of the hydrodynamic test in a towing tank

At the initial condition of the test, the ship had a draft of 75 mm in calm water. In the diffraction test, the motion response of the ship was restrained, the force acting on the hulls by the incident waves was measured. The sampling frequency of the data acquirement system was 100 Hz. The forward speed of the model ship was chosen as 0 m/s and 1.5 m/s, whose the Froude Number were 0 and 0.3786, respectively.

A.3.2 Results of the Diffraction Test

Experimental results of the wave exciting force and wave exciting moment were showed from Fig.A.9 to Fig.A.12. The comparisons of which to that of the calculation by NSM were also depicted. Without forward speed, a reasonable agreement on the magnitude as well as the phase between the two was observed. However, when the forward speed was 1.5 m/s, such agreement was only obtained if the ratio of the wave length to the ship length was above 0.5 for the wave exciting force, 0.3 for the wave exciting moment. It was mentioned by Prof.Kashiwagi that NSM may cause large error while the wave length is short. Therefore, it was regarded that the experimental results were more reliable comparing to calculated result while the forward speed was 1.5 m/s.

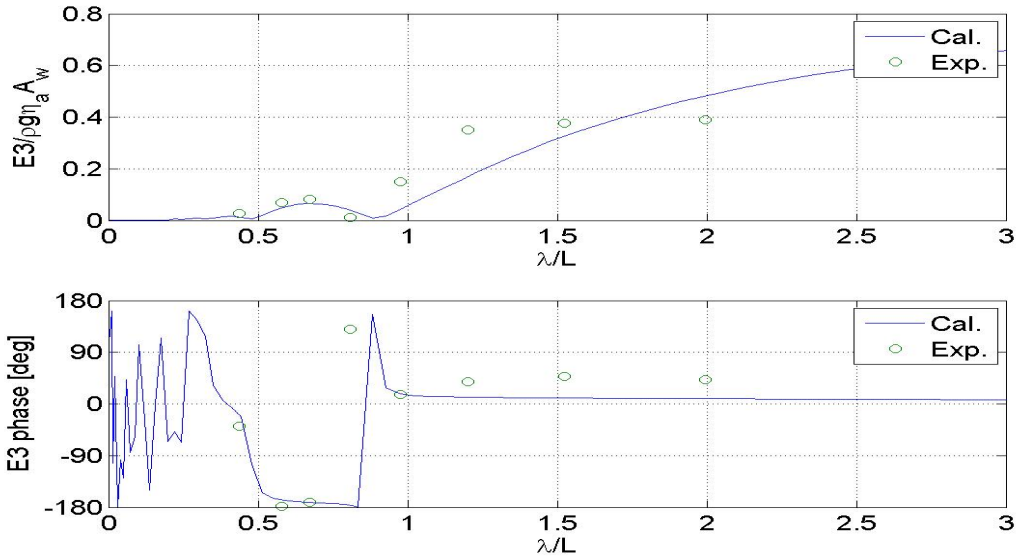

Figure A.9: Comparison of wave exciting force without forward speed

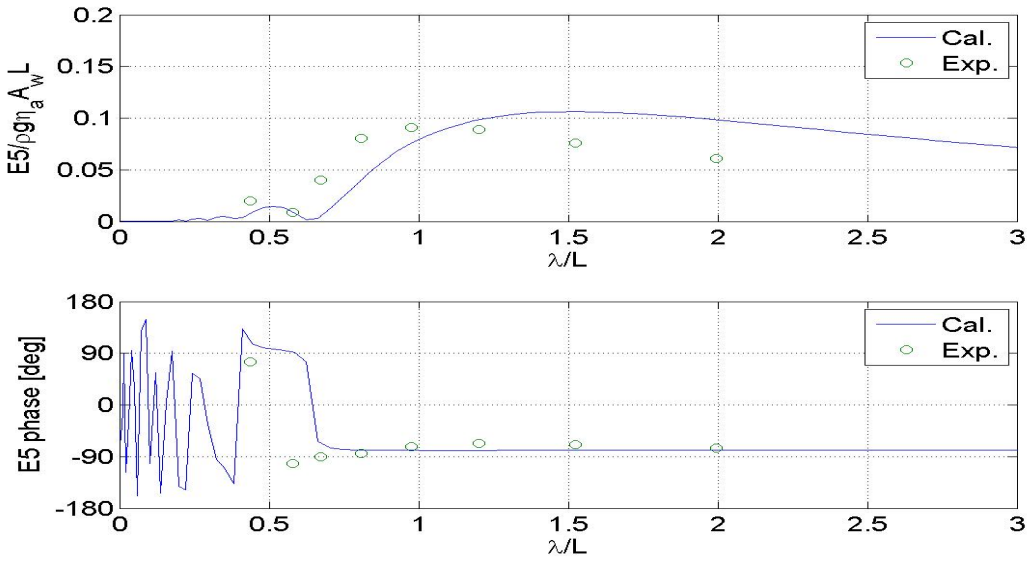

Figure A.10: Comparison of wave exciting moment without forward speed

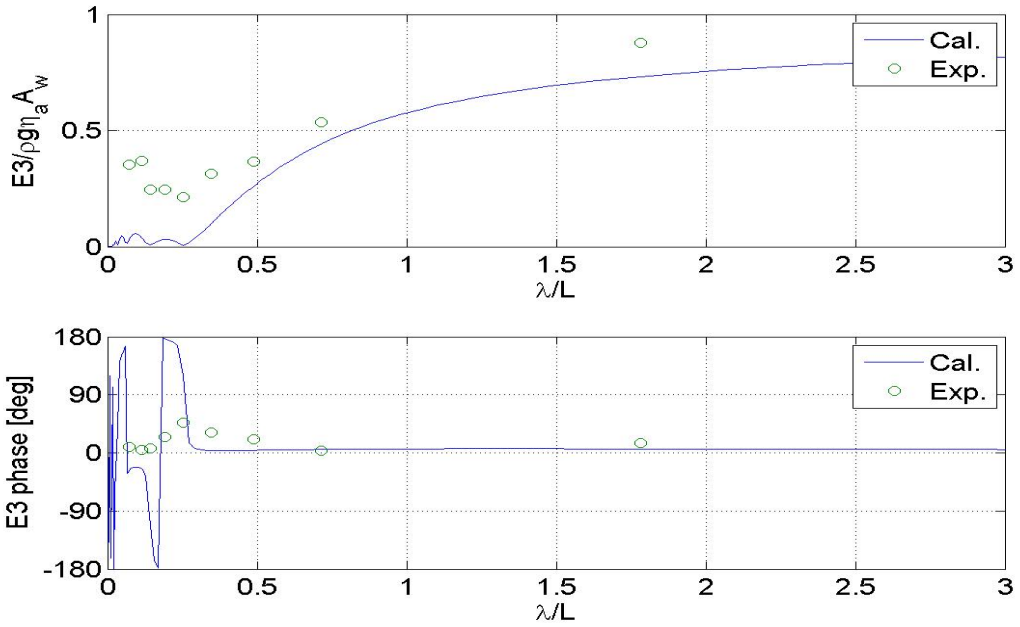

Figure A.11: Comparison of wave exciting force with forward speed of 1.5 m/s, $Fn = 0.3786$

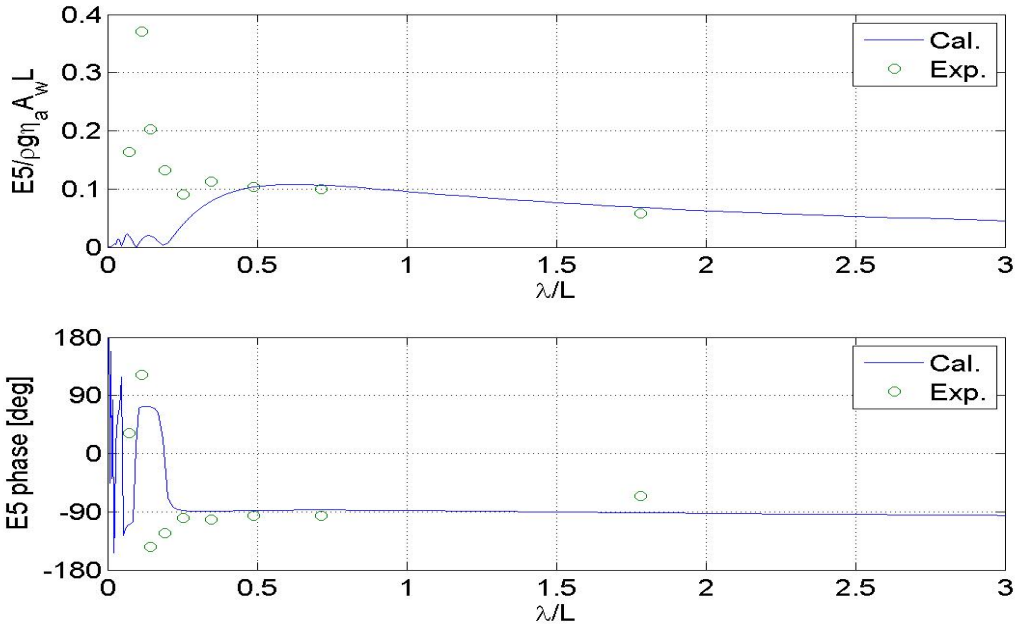

Figure A.12: Comparison of wave exciting moment with forward speed of 1.5 m/s, $Fn = 0.3786$

A.4 Results of Equations of Motion

Figure A.13 showed the heave and pitch response of the cabin and the hulls at the free mode with a forward speed of 0 m/s. The break line represents the calculation results, while the $*$ mark represents the experimental results. It showed that the calculation and the experiment reached a good agreement at the heave motion, however, the pitch motion was not. Especially, pitch resonance of the cabin was not observed in the calculation.

Figure A.14 showed the results at the rigid mode. The spring constant in the equations of motion was set at extremely large so as to form a rigid body. The approach was proven to be effective, since the cabin and the hulls showed the same motion response. Comparing the experiment to the calculation, one may find that the heave motion agreed with each other very well, except that around 8 rad/s. A resonance was seen in the experiment, but it was not observed in the calculation. At low frequency domain, the pitch in the experiment was approaching the wave slope, however, the one obtained in the calculation was smaller than that.

The reasons for the above mentioned deviation can be explained from several aspects. An important one related to the estimation of the moment of inertia. It was done by an experiment, in which the hulls was tested first, and then the parts of the cabin and the suspensions. Known that the mass of the suspensions was assumed to be equally distributed into the cabin section and the hulls section, however, that of the moment of inertia was difficult to do similarly. Another reason may relate to the NSM. In the calculation, the hydrodynamic force and coefficient were doubled so as to apply it on a catamaran. In this way, the interaction of the two hulls was not considered, meanwhile, enlarged the force and coefficient directly may not be an appropriate approximation. Furthermore, in the tank experiment it was seen that at some frequencies the rotational center of the pitch may be shifted toward to the stern, since the relative displacement at the front was larger than that at the rear. Such phenomenon was not realized in the calculation as well. Other reasons may take part of the responsibility as well, for instance, the actual outline of the hand-made hulls may differ from that of the design slightly, the distance of the suspensions to the center of the gravity may not be exactly 0.36 m as the design and so on.

The comparison at a forward speed of 1.5 m/s was not carried out, because at short wave conditions the reliability of the NSM was questionable. Despite deviations at some frequencies between the experiment and the calculation, the motion response of the catamaran can be considered as reasonable. Since the hydrodynamic coefficients and the wave exciting force/moment were not the main focus of this research, the improvement of their estimation was not further discussed in this section.

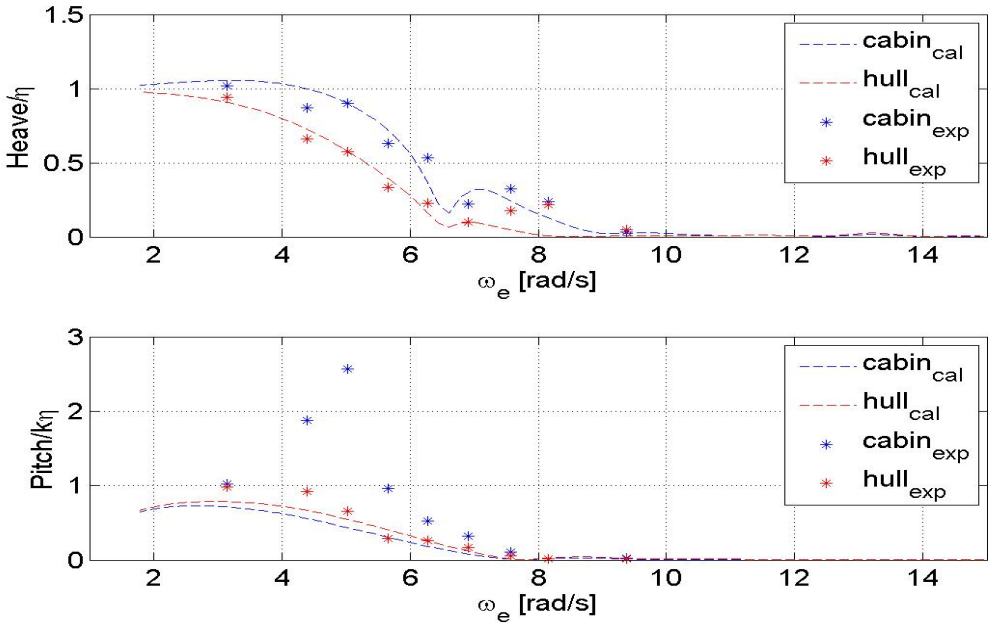

Figure A.13: Comparison of heave and pitch between calculation and experiment at the free mode, with forward speed of 0 m/s, $Fn = 0$

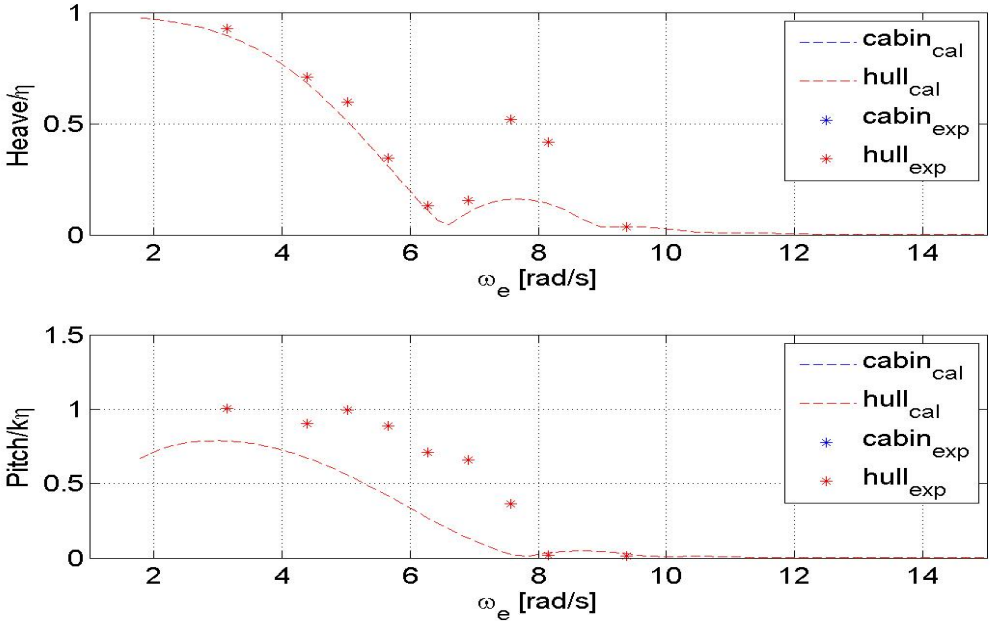

Figure A.14: Comparison of heave and pitch between calculation and experiment at the rigid body mode, with forward speed of 0 m/s, $Fn = 0$